Abstract

Title of Dissertation:	MODULATION OF EARLY OLFACTORY CIRCUITS BY LONG-RANGE GABAERGIC INHIBITION
	Pablo Sebastian Villar Del Rio, Doctor of Philosophy, 2022
Dissertation directed by:	Professor Ricardo C. Araneda, Department of Biology

Sensory perception emerges from the interplay between stimulus-driven feedforward cortical activation and feedback signals that sculpt the activity of early sensory circuits. Odor information is first processed in the olfactory bulb and the activity of its circuits is flexibly shaped by descending signals that arise in several brain regions, including neurons in the basal forebrain (BF). Among these neurons, a group of GABAergic neurons in the BF can modulate odor processing, however, how is this achieved is unknown. Here, we investigate how the activity of long-range GABAergic neurons in the BF modulate the spatiotemporal dynamics of the bulb output neurons. To examine the odor evoked responses of GABAergic neurons, we monitor the activity of their axons in the olfactory bulb of awake mice and characterize their response as a function of odor identity and concentration, using multiphoton calcium imaging. In addition, we

provide anatomical and functional evidence for the existence of a feedback loop that is able to recruit GABAergic neurons in the BF through direct glutamatergic inputs originating in the olfactory cortex. Our work underscores basic principles on how stimulus-driven feedforward information recruits higher-order brain regions to provide descending feedback signals capable of shaping the output of early sensory processing stages.

MODULATION OF EARLY OLFACTORY CIRCUITS BY LONG-RANGE GABAERGIC INHIBITION

by

Pablo Sebastian Villar Del Rio

Dissertation submitted to the Faculty of the Graduate School of the
University of Maryland, College Park, in partial fulfillment
of the requirements for the degree of
Doctor of Philosophy in Biological Sciences
2022

Advisory Committee:

Dr. Ricardo C. Araneda, Chair
Dr. Dinu F. Albeanu
Dr. Elizabeth Quinlan
Dr. Quentin Gaudry
Dr. Anna Xuan Li
Dr. Joshua Singer
Dr. Jens Herberholz, Deans Representative

Preface

All experiments in this dissertation were performed by Pablo S. Villar. Local field potential experiments in Chapter 2, were obtained in collaboration with Dr. Ruilong Hu. *In vivo* imaging experiments presented in Chapter 3 were conducted in the laboratory of Dr. Dinu F. Albeanu in Cold Spring Harbor Laboratory, New York. Whole-brain imaging experiments in Chapter 4 were done in collaboration with Dr. Arun Narasimhan in Cold Spring Harbor Laboratory, New York. Histology experiments in Appendix A and Chapter 4 were done in collaboration with Ms. Batya Teitz and Ms. Meghan Deyesu, respectively. Two articles resulted from this dissertation have already been published and are presented in Chapter 2 and Appendix A, respectively:

Villar PS, Hu R and Araneda RC (2021). Long-Range GABAergic Inhibition Modulates Spatiotemporal Dynamics of the Output Neurons in the Olfactory Bulb. The Journal of Neuroscience. 41(14): 3610–3621.

Villar PS, Hu R, Teitz B and Araneda RC (2021). Cholinergic modulation of distinct inhibitory domains in granule cells of the olfactory bulb. BioRxiv. https://doi.org/10.1101/2021.10.15.464603.

Chapter 3 and Chapter 4 are preliminary drafts of the two respective articles in preparation listed below:

Villar PS, Araneda RC and Albeanu DF. Basal forebrain GABAergic projections to the olfactory bulb are rapidly recruited by odor encounters in a stimulus specific manner (*in preparation*).

Villar PS, Deyesu M, Narasimhan A, Araneda RC. Subpopulations of basal forebrain long-range GABAergic neurons are selectively recruited by fast olfactory-cortical inputs (*in preparation*).

Dedication

To Elisa María and José Manuel.

Acknowledgements

I am grateful to have had the opportunity to work in the laboratory of Dr. Ricardo Araneda. I appreciate Ricardo's dedicated mentoring in all aspects of my academic life, and his effort for ensuring my success in graduate school. Ricardo allowed me the freedom to explore my own scientific interests, while giving me valuable feedback which helped me to stay focused on long-term goals. I am also grateful of the opportunity to have worked with Dr. Dinu F Albeanu. I thank to Florin for his generosity and kindness, and all members of the Albeanu lab for their help and friendship.

I would like to thank numerous talented students and scientists I met during my time in the Araneda lab, especially Ruilong Hu with whom I share the best memories in graduate school. Finally, I would like to thank my family and friends for all their love and emotional support.

Table of Contents

List of Abbreviations

4-AP	4-aminopyridine
ACh	acetylcholine
ACN	anterior cortical nucleus
ACSF	artificial cerebrospinal fluid
AL	antennal lobe
AOB	accessory olfactory bulb
AON	anterior olfactory nucleus
BF	basal forebrain
BNST	bed nucleus of stria terminalis
BRS	bouton response spectrum
CB	calbindin
ChAT	choline acetyl transferase
ChR2	channelrhodopsin-2
Cr	calretinin
CTB	subunit B of cholera toxin
DAR	dopaminergic receptor
DDI	dendrodendritic inhibition
DDS	dendrodendritic synapse
dSAC	deep short-axon cell
EC	entorhinal cortex
eIPSC	evoked inhibitory postsynaptic current
EPL	external plexiform layer
EPL-I	external plexiform layer interneuron
EPSC	excitatory postsynaptic current
FOV	field of view
FS	fast spiking
GABA	ɣ-aminobutyric acid
Gad2	glutamate decarboxylase type 2
GC	granule cell
GCL	granule cell layer
GL	glomerular layer
HDB	horizontal limb of the diagonal band of Broca
IACUC	Institutional Animal Care and Use Committee
LFP	local field potential
LOT	lateral olfactory tract

LRGN	long-range GABAergic neuron
LS	lifetime sparseness
M/TC	mitral/tufted cells
mAChR	muscarinic acetylcholine receptor
MC	mitral cell
MCPO	magnocellular preoptic area
MeA	medial amygdaloid nucleus
MEC	medial entorhinal cortex
min-eIPSC	minimally evoked inhibitory postsynaptic current
MOB	main olfactory bulb
MOE	main olfactory epithelium
MPOA	medial preoptic area
MS	medial septum
MS/DBB	medial septum/diagonal band of Broca
nAChR	nicotinic acetylcholine receptor
nLOT	nucleus of the lateral olfactory tract
OB	olfactory bulb
ON	olfactory nerve
OR	olfactory receptor
ORS	odor response spectrum
OSN	olfactory sensory neuron
PBS	phosphate buffer saline
PBS-T	PBS + Triton X-100
PC	piriform cortex
PGC	periglomerular cell
PID	photoionization device
PLCN	posterolateral cortical amygdaloid nucleus
PMCN	posteromedial amygdaloid cortical nucleus
PN	projection neuron
PV	parvalbumin
SAC	short axon cell
SI	substantia innominata
sim-EPSP	simulated excitatory postsynaptic potential
Sst	somatostatin
STPT	serial two-photon tomography
TC	tufted cell
TT	tenia tecta

Tu	olfactory tubercle
uIPSC	photo-evoked inhibitory postsynaptic current
VHM	ventromedial hypothalamus
VNO	vomeronasal organ

Chapter 1

Introduction

The mammalian olfactory system

Mammals rely on olfaction to fulfill essential needs such as feeding and mating, as well as avoiding predators and harmful substances. Olfaction is among the oldest sensory systems and its signal transduction involves the largest family of receptor proteins in the mammalian genome (Hildebrand and Shepherd, 1997). The large set of olfactory receptors (OR) genes (~1,000 in rodents) (Buck and Axel, 1991), is thought to provide animals with an enormous discriminatory power (Eisenberg and Kleiman, 1972). Airborne molecules gain access to a neuroepithelium lining the back of the nasal cavity, where olfactory sensory neurons (OSN) transform chemical cues into electrical impulses. Generally, each OSN expresses a single or few types of ORs (Mombaerts, 2004), which confers a particular odor receptive field to each OSN. The tuning of OSNs for odor molecules ranges from narrow to broad (Araneda et al., 2000, 2004), thus odor activation of neurons in the olfactory epithelium results in the recruitment of a unique combination of OSNs, which is enhanced in complexity by odor antagonism and potentiation at the receptor level (Oka et al., 2004; Inagaki et al., 2020; Pfister et al., 2020; Xu et al., 2020; Zak et al., 2020).

Olfactory stimuli can be broadly divided into two main groups based on the type of information they convey: common odors and pheromones. Accordingly, the mammalian olfactory system processes odor stimuli through two separate sensory organs: the main

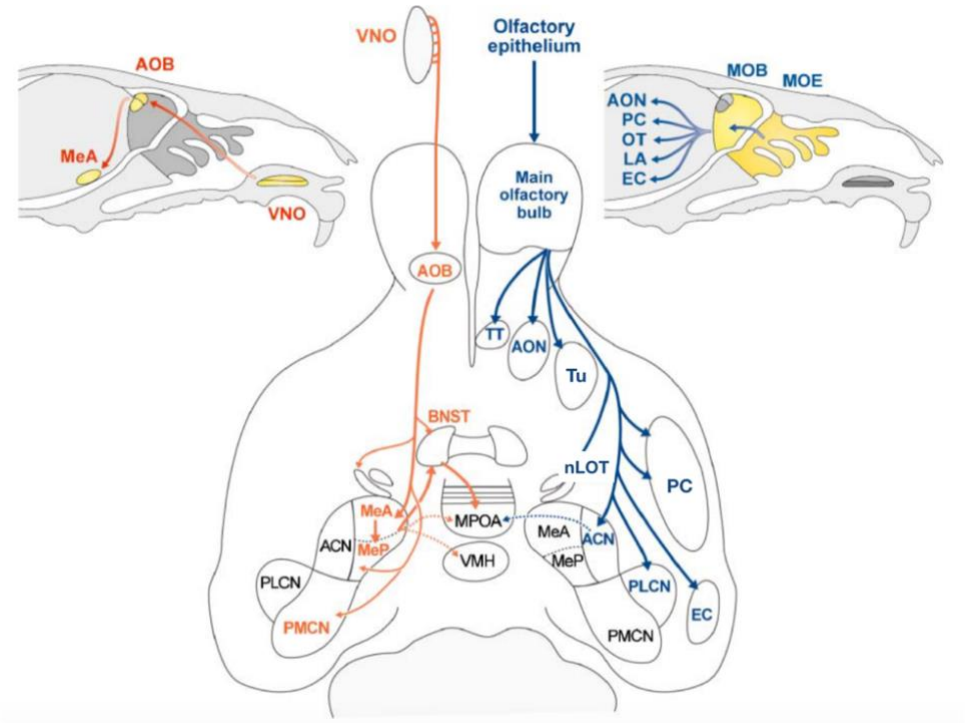

Fig. 1: *The olfactory system in rodents*

Right, volatile odor molecules activate olfactory sensory neurons of the main olfactory epithelium (MOE). These sensory neurons project to the main olfactory bulb (MOB) where the olfactory information is first processed. MOB output neurons project to multiple cortical areas including the tenia tecta (TT), anterior olfactory nucleus (AON), olfactory tubercle (Tu), piriform cortex (PC), nucleus of the lateral olfactory tract (nLOT), anterior cortical and posterolateral cortical amygdaloid nuclei (ACN and PLCN, respectively), and entorhinal cortex (EC). Left, non-volatile molecules activate sensory neurons of the vomeronasal organ (VNO), which in turn project to the accessory olfactory bulb (AOB). The AOB output neurons project to multiple targets in the limbic system including the posterior bed nucleus of the stria terminalis (BNSTp), medial (MeA/MeP) and posteromedial cortical amygdaloid nucleus (PMCN), anterior cortical nucleus (ACN) and posterolateral cortical amygdaloid nucleus (PLCN). Neuronal projections from both olfactory pathways converge into hypothalamic nuclei, including the medial preoptic area (MPOA) and the ventromedial hypothalamus (VMH). Modified from C. Dulac & S. Wagner, 2006.

olfactory epithelium (MOE), which mainly detects common odorants, and the vomeronasal organ (VNO) which is most sensitive to pheromones. In the VNO, pheromones activate a class of receptors unrelated to the receptors expressed in the MOE, the V1R and V2Rs (Dulac and Axel, 1995; Liman, 1996; Herrada and Dulac, 1997). V1R expressing neurons lie in the apical layer of the VNO, while V2R expressing neurons preferentially reside in its basal layer suggesting these two receptor classes convey distinct pheromonal information (Jia and Halpern, 1996; Rodriguez et al., 1999). Despite this anatomical separation, simultaneous activation of MOE and VNO appears to be essential for normal pheromone-mediated behaviors (Dulac and Torello, 2003; Dulac and Wagner, 2006). OSNs in the MOE project a single axon to the surface of the main olfactory bulb (MOB) where they synapse onto apical dendrites of the MOB output neurons, the mitral (MC) and tufted cells (TC), in a neuropile structure termed glomerulus (Shepherd, 2004). OSNs expressing the same OR type bundle within the olfactory nerve (ON) to exclusively innervate two glomeruli in the mouse MOB (Shibuya and Shibuya, 1963; Mombaerts et al., 1996). This arrangement suggests that at least at the glomerular level, odor signals are organized in a labeled line fashion, where a given glomerulus exhibits the same odor tuning as the OSNs that innervate it. Odor signals conveyed by activation of OSNs are integrated in the glomeruli by MCs and TCs, which in turn broadcast these signals to multiple brain areas (**Figure 1**). MC and TC axons bundle in the lateral olfactory tract (LOT), which primarily targets the piriform cortex (PC) and the anterior olfactory nucleus (AON), as well as the olfactory tubercle (Tu), nucleus of the lateral olfactory tract (nLOT), entorhinal cortex (EC) and tenia tecta (TT) (**Figure 1**, blue arrows) (Shepherd, 2004; Dulac and Wagner, 2006). The output neurons of the OB also innervate regions of the limbic system

including the posterolateral cortical amygdaloid nucleus (PLCN) and the anterior cortical nucleus (ACN), which in turn provide inputs to hypothalamic areas such as the medial preoptic area (MPOA).

In contrast, VNO sensory neurons project to the accessory olfactory bulb (AOB), where they convey pheromonal information to the output neurons of the AOB, which are less well defined than in the MOB and termed M/TCs (Brennan, 2001). Unlike in the MOB, axons from AOB MCs avoid cortical areas and instead project to nuclei of the limbic system; among them the posteromedial amygdaloid cortical nucleus (PMCN), medial amygdaloid nucleus (MeA), bed nucleus of stria terminalis (BNST) and nucleus of the accessory olfactory tract (**Figure 1**, orange arrows) (Dulac and Wagner, 2006). In turn, these AOB target regions convey pheromonal information to hypothalamic nuclei associated to social behaviors such as the ventromedial hypothalamus (VHM) and MPOA (Petrovich et al., 2001).

Synaptic organization of the olfactory bulb

Early stages of odor processing in the OB are characterized by prominent local inhibitory circuits that shape the activity of MCs and TCs (Shepherd, 2004; Nagayama et al., 2014). Glomeruli are surrounded by local GABAergic neurons collectively called juxtaglomerular cells, and among them, the most abundant are the periglomerular cells (PGC) (**Figure 2**). These axonless neurons are primarily GABAergic and target the apical dendrites of MCs and TCs as well as the axon of OSNs, thereby modulating the incoming odor signals (Shipley and Ennis, 1996). Presynaptic inhibition of OSN axons by PGCs is

thought to function as a sensory gain mechanism (Wachowiak and Cohen, 1999; Aroniadou-Anderjaska et al., 2000; Ennis et al., 2001; Wachowiak et al., 2005; Shao et al., 2012). The activity of PGCs is driven by glutamate release from the dendritic tuft of MCs and TCs, and direct inputs from sensory afferents (Shepherd, 2004). In addition, a subtype of juxtaglomerular neurons termed short axon cells (SACs), allow long-range interactions between multiple glomeruli (Aungst et al., 2003; Kiyokage et al., 2010). These interneurons have been proposed to implement normalization of the OB output signal and decorrelation of odor representations (Zhu et al., 2013a; Banerjee et al., 2015).

MCs and TCs extend long lateral dendrites into the external plexiform layer (EPL) of the bulb where they form ubiquitous dendrodendritic synapses (DDS) with another type of inhibitory neuron, the granule cells (GC) (**Figure 2A**). Functionally, GCs regulate MCs and TCs activity through two types of inhibitory mechanisms: dendrodendritic inhibition (DDI) and lateral inhibition. DDI results from recurrent local release of ɣ-aminobutyric acid (GABA) from the dendritic spines of GCs, activated by the glutamate release from a connected MC's lateral dendrite (Yokoi et al., 1995; Isaacson and Strowbridge, 1998; Christie et al., 2001; Schoppa and Urban, 2003; Shepherd, 2004). Lateral inhibition involves a global GC depolarization and dendritic Ca^{2+} increase, leading to a broader release of GABA. GCs make DDS with several MCs (and TCs); thus an active MC can inhibit surrounding MCs. This latter mechanism is proposed to generate contrast enhancement and center-surround inhibition in analogy with retinal visual processing (Isaacson and Strowbridge, 1998; Mori et al., 1999; Egger et al., 2003; Shepherd, 2004; Arevian et al., 2008). DDI and lateral inhibition are thought to shape the output signal of MCs both in the temporal and spatial domains (Yokoi et al., 1995; Isaacson and

Strowbridge, 1998; Schoppa, 1998; Mori et al., 1999; Egger et al., 2003; Lagier et al., 2007; Arnson and Strowbridge, 2017). Unlike in other sensory modalities, the axons of MCs and TCs directly reach the cortex, bypassing the thalamus (**Figure 1**); therefore, several models propose that important aspects of olfactory coding occur in the OB, including those that contribute to odor discrimination and concentration invariance of odor perception (Storace and Cohen, 2017; Wilson et al., 2017).

Less is known about the processing of pheromonal signals by the AOB. The synaptic arrangement of the AOB differs from the MOB in that AOB MCs extend apical dendrites to multiple glomeruli (**Figure 2B**). Studies have shown that a significant fraction of AOB MCs receive inputs from glomeruli associated to different sensory neurons, but expressing closely related vomeronasal receptors (Wagner et al., 2006), which contrasts the labeled line connectivity of the MOB, suggesting early integration of sensory inputs from the VNO (Keverne, 1999; Wagner et al., 2006). Nevertheless, like in the MOB, the most abundant neuronal type in the AOB are local inhibitory neurons that serve a similar inhibitory role, and are therefore proposed to have a similar role in pheromonal coding (Jia et al., 1999; Mohrhardt et al., 2018).

Olfactory processing

Odors with different molecular structure activate loosely clustered arrays of glomeruli in the bulb (Rubin and Katz, 1999; Johnson and Leon, 2000; Uchida et al., 2000; Wilson and Mainen, 2006). For instance, aldehydes tend to activate glomeruli in the anterior portion of the bulb surface, while alcohols activate disproportionally more

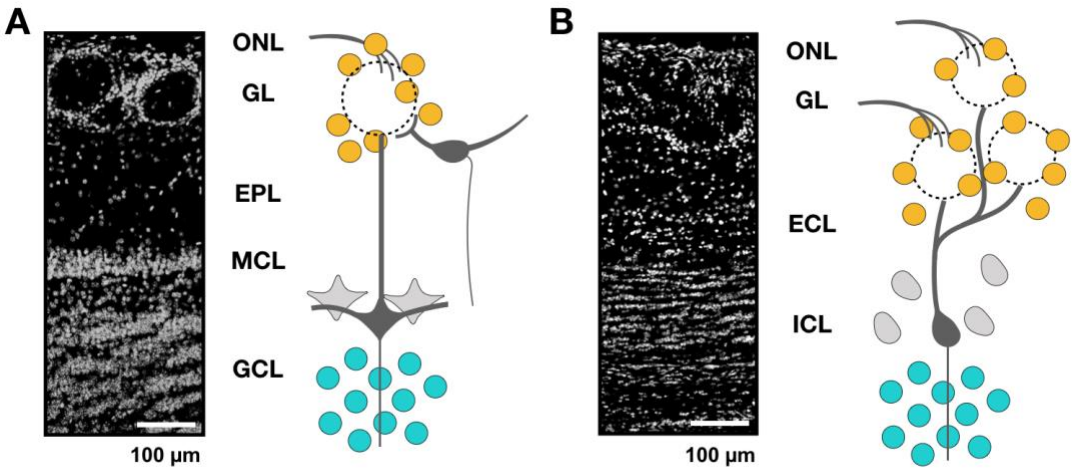

Fig. 2: *Morphological differences between the main and accessory olfactory bulb*

(A) Left, nuclear staining (dapi) of a horizontal slice of the MOB reveals the different cellular layers of the MOB, shown as a scheme on the right. Signals from sensory neurons in the nose innervate the surface of the OB forming the olfactory nerve layer (ONL). The OB output neurons mitral and tufted cells (gray) convey the sensory stimuli and in turn activate local GABAergic neurons in the glomerular layer (GL, yellow) and granule cell layer (GCL, cyan), which shape MC and TC activity. **(B)** Left, nuclear staining of a sagittal slice of the AOB. Right, peripheral inputs from the VNO innervate the glomerular layer of the AOB. The AOB output neurons MCs locate in the external cellular layer (ECL) and project to multiple glomeruli. The AOB internal cellular layer (ICL) contains the inhibitory GCs.

glomeruli in the medial part. These observations lead to propose that inputs to the bulb are organized in a chemotopic map. However, when glomerular responses to a large set of odors are explored on a finer scale, neighboring glomeruli show considerably different responses to structurally similar odors (Bozza et al., 2004; Soucy et al., 2009; Ma et al., 2012). These findings argue against the existence of chemotopic representations in the MOB and the possible role of lateral inhibition as a mechanism for contrasts enhancement of odor signals as originally postulated (Yokoi et al., 1995).

As respiration is inherently related to the access of odor molecules to the nose, the activity of the OB output neurons often correlates with the respiration rhythm (Macrides

and Chorover, 1972; Onoda and Mori, 1980). The firing of MCs and TCs precisely locks to particular times of the sniff cycle (Cury and Uchida, 2010; Shusterman et al., 2011; Smear et al., 2011; Wachowiak, 2011). Individual OB output neurons show odor specific temporal patterns with a trial-to-trial timing precision on the order of 10 ms in awake mice, yet these patterns are highly diverse across populations of neurons (Shusterman et al., 2011). Importantly, in experiments where the olfactory input was optogenetically controlled by expressing channelrhodopsin-2 (ChR2) in the OSNs, mice were able to discriminate between brief light stimulations across different sniff phase points shifted by as little as 10 ms (Smear et al., 2011). This evidence suggests that the olfactory system of rodents can encode fast temporal patterns in an exquisitely precise manner, with a temporal precision comparable to that reported in the auditory and visual systems (Wehr and Zador, 2003; Butts et al., 2007).

Network oscillations are a prominent feature of the OB (Adrian, 1942), and have been proposed to provide a substrate for the encoding of information by MCs and TCs (Kay et al., 2009; Fukunaga et al., 2014). Oscillations in the recorded local field potential (LFP) can be observed across a wide spectrum of frequencies, ranging from 4 to 100 Hz (Kay, 2015). Different frequency bands of the LFP are thought to arise as a consequence of the interaction between output neurons and local GABAergic circuits (Fukunaga et al., 2014; Kay, 2014). For instance, oscillations in the θ frequency band (~4 to 12 Hz), entrained by the respiratory cycle, are partly orchestrated by PGCs (Lagier et al., 2004; Fukunaga et al., 2014), while ɣ oscillations (~40 to 80 Hz) arise from the recruitment of GC inhibition (Rall and Shepherd, 1968; Kay, 2014). In addition, β-range oscillations (~20 Hz) are present in both the OB and PC and are associated with odor learning (Martin et al.,

2007; Kay et al., 2009). Some of the fast electrical oscillations and rhythmic patterns are present across olfactory areas *ex vivo*, suggesting that this activity likely originates from intrinsic circuit properties (Balu et al., 2004; Hayar, 2004; Schoppa, 2006; Pandipati et al., 2010; Pandipati and Schoppa, 2012; Villar et al., 2021a).

Despite the undisputed existence of network oscillatory activity across olfactory areas, their relevance for olfactory processing remains highly debated, mainly because ablating oscillations typically requires interrupting basic neural circuit function (Kay et al., 2009). The strongest argument for the role of odor-evoked neural synchronization in odor perception and the involvement of inhibitory neurons in this process has come from studies in the antennal lobe (AL) of insects, an analogue structure to the mammalian OB. Projection neurons (PN) in the AL, which are analogous to MCs and TCs, respond with an odor-specific synchronized firing pattern (Laurent et al., 1996). This synchronized firing is sculpted by the interaction of PNs with local inhibitory neurons (Laurent and Davidowitz, 1994). Thus, when fast inhibitory transmission is pharmacologically inhibited in the AL, the oscillatory synchronization of PNs is abolished and the discrimination of molecularly similar odors is impaired, however, the response profile and odor-specificity of the PNs remain unaltered (MacLeod and Laurent, 1996; Stopfer et al., 1997). Thus, local GABAergic inhibition in early olfactory areas of insects appears to participate in neuronal synchronization but not in odor response tuning. Furthermore, in mice the intensity of ɣ oscillations in the OB correlates positively with the excitability of the local GABAergic network and olfactory discriminatory power (Nusser et al., 2001).

Neuromodulatory regulation of olfactory circuits

Odor processing in the bulb is profoundly influenced by behavioral states through top-down innervation from several neuromodulatory systems. Among these, the noradrenergic, cholinergic and GABAergic afferences represent the main sources of neuromodulation of the OB (Shipley et al., 1985; Zaborszky et al., 1986, 2012; McLean et al., 1989; Voytko et al., 1994; Voytko, 1996). Noradrenergic projections originate in the locus coeruleus and its activity strongly correlates with wakefulness, alertness and arousal (Foote et al., 1980; Florin-Lechner et al., 1996; Aston-Jones and Cohen, 2005). Adrenergic modulation of the OB circuit have been implicated in important olfactory processes, including odor learning (Sullivan et al., 1989; Doucette et al., 2007), network oscillatory dynamics (Manella et al., 2017; Ramirez-Gordillo et al., 2018) and promoting adult neurogenesis of the inhibitory neurons of the OB (Moreno et al., 2012). Throughout the brain, noradrenaline acts through three classes of adrenergic receptors: α_1, α_2 and β, all of which are expressed in the OB (Pieribone et al., 1994; Woo and Leon, 1995; Day et al., 1997; Small et al., 2003; Hein, 2006). Activation of the different types of adrenergic receptors gives rise to diverse cellular responses due to coupling to different intracellular transduction pathways. In the OB, adrenergic activation modulates DDI by directly acting on α_1 and β receptors in GCs (McLean et al., 1989; Araneda and Firestein, 2006; Smith et al., 2009; Nai et al., 2010; Pandipati et al., 2010; Pandipati and Schoppa, 2012; Zimnik et al., 2013), producing a long-lasting increase in GABAergic inhibitory inputs onto MCs. At the circuit level, the actions of noradrenaline are complex due to the diversity of receptor types expressed in the different cell types, yet overall adrenergic activation excites MCs in

the MOB due to a direct excitatory action on α_1 receptors (Hayar et al., 2001), while inhibits MCs of the AOB by acting on the inhibitory GCs (Araneda and Firestein, 2006; Doyle and Meeks, 2017).

Context-dependent neuromodulation of the OB also originates in the basal forebrain (BF) (Voytko et al., 1994; Voytko, 1996). The BF broadly integrates cortical and subcortical information, which can be relayed to the bulb through extensive cholinergic innervation of all bulb layers (Zaborszky et al., 1986, 2012). OB projecting cholinergic neurons reside in the nucleus of the horizontal limb of the diagonal band of Broca (HDB). In addition to the bulb, HDB cholinergic neurons send projections throughout the cortical mantle, including the olfactory cortex. The release of acetylcholine by these neurons is highly influenced by the behavioral state, and has profound impacts on a diverse array of cognitive processes ranging from arousal, attention, learning and cognitive performance (Hasselmo and Sarter, 2011; Lee and Dan, 2012; Ballinger et al., 2016; Jiang et al., 2016). In the bulb, acetylcholine acts predominantly through the activation of muscarinic acetylcholine receptors (mAChRs) (Castillo et al., 1999; Ghatpande et al., 2006; Pressler et al., 2007a; Smith et al., 2015), and nicotinic receptors (nAChRs) (Castillo et al., 1999; Araneda and Smith, 2010; D'Souza et al., 2013). Muscarinic receptors are divided into five subclasses: M1, M3 and M5, which couple to phospholipase C having an overall excitatory effect, and M2 and M4, which inhibit adenyl cyclase leading to an overall inhibitory effect (Thiele, 2013). The distribution of mAChRs in the OB shows complex patterns across layers and the functional role for such diversity remains unknown. Optogenetic activation of cholinergic afferents *in vivo* reduces the spontaneous firing of MCs and TCs and sharpens their olfactory responses, while it broadens odor responses in GABAergic

interneurons (Ma and Luo, 2012; Rothermel et al., 2014). At the cellular level, cholinergic activation drives opposite effects in the output neurons of the MOB and AOB. Muscarinic activation drives a strong depolarization of AOB MCs mediated by the activation of M1-mAChRs (Araneda and Smith, 2010), while MOB MC are inhibited by M2-mAChRs activation (Smith et al., 2015). Similar opposing effects are observed in the regulation of GCs. Activation of M1-mAChRs increases the excitability of AOB GCs, while M2-mAChRs activation hyperpolarizes MOB GCs, together with inducing a slow afterdepolarization (Pressler et al., 2007a; Araneda and Smith, 2010; Smith et al., 2015). These differences in the modulatory action of acetylcholine across the similar circuits of the MOB and AOB could be related to the processing of distinct sensory signals, which are relevant in different behavioral contexts.

Descending cortical inputs to early olfactory processing areas

Early olfactory processing in the OB is also regulated by extensive top-down projections from olfactory-cortical regions. Glutamatergic projections from the PC, AON and EC innervate the local inhibitory neurons in the granule cell layer (GCL) and glomerular layer (GL) (Shipley and Adamek, 1984; Boyd et al., 2012; Markopoulos et al., 2012; Rothermel and Wachowiak, 2014). Fast excitation of GCs and PGCs by these glutamatergic signals produces a strong disynaptic inhibition in the output neurons (Boyd et al., 2012; Markopoulos et al., 2012). The excitatory feedback from the PC targets exclusively local GABAergic cells, including the deep-short axon cells (dSACs), which represent a local source of inhibition to GCs (Boyd et al., 2012). Functional studies have

shown that the odor-driven recruitment of the PC glutamatergic feedback to the OB is sparse and specific to the odor identity, likely reflecting a sparse odor coding in the PC (Poo and Isaacson, 2009). Pharmacological inactivation of the PC increases responsiveness and correlation of bulb output neurons. These findings propose that the PC corticobulbar feedback allows for decorrelation of MCs, thus enabling odor discrimination (Otazu et al., 2015). Furthermore, studies *in vivo* have shown that glutamatergic feedback projections from the AON, another cortical area targeted by the MCs and TCs, contribute to the generation of precisely timed spikes in MCs and control of basal firing, suggesting that the AON can modulate ongoing odor representations in the OB output neurons (Markopoulos et al., 2012).

Top-down GABAergic innervation of the olfactory bulb

Unlike numerous sources of fast glutamatergic feedback, only few areas have been reported to provide GABAergic innervation to the OB. The BF is a main source of long-range projecting GABAergic cells which broadly innervates cortical and subcortical structures (Zaborszky et al., 1986; Gritti et al., 1997, 2003). BF GABAergic innervation to the OB originates in a nucleus called the magnocellular preoptic area (MCPO) (Gracia-Llanes et al., 2010; Nunez-Parra et al., 2013), in which GABAergic and cholinergic cells intermingle (Zaborszky et al., 1986). Although traditionally BF GABAergic neurons have been studied in the context of cortical arousal and sleep (Yang et al., 2014a, 2017; Brown and McKenna, 2015; Kim et al., 2015a; Lin et al., 2015; Xu et al., 2015; Zant et al., 2016; McKenna et al., 2021), recent evidence suggest that these neurons have also a role in

sensory processing (Melzer et al., 2012; Gonzalez-Sulser et al., 2014; Kim et al., 2015a). Particularly, chemogenetic silencing of the MCPO GABAergic neurons greatly impairs fine odor discrimination in mice (Nunez-Parra et al., 2013). Furthermore, a recent study showed the existence of a smaller population of OB-projecting GABAergic neurons in the AON, which can inhibit spontaneous and odor evoked activity of MCs and TCs *in vivo*. Chemogenetic silencing of these projections, as with the MCPO, also impairs odor discrimination (Mazo et al., 2020).

While recent studies have shed new light on the mechanisms of action of top-down GABAergic regulation of the OB (Sanz Diez et al., 2019; Böhm et al., 2020; Hanson et al., 2020; Villar et al., 2021a), the activation dynamics of OB-projecting MCPO GABAergic neurons and their functional role in modulating odor representations in olfactory circuits remain unknown and are the main focus of this dissertation.

Specific aims

The OB receives rich excitatory and inhibitory descending projections from cortical and subcortical areas, which fine tune local neurons and ultimately modulate the circuit outputs (De Olmos et al., 1978; Luskin and Price, 1983; Shipley and Adamek, 1984; Matsutani and Yamamoto, 2008). Over the last decade, several studies revealed the features of the cortical excitatory glutamatergic feedback in the OB and their role in olfactory processing. In contrast, little is known on the activation of descending inhibitory GABAergic projections from the BF, and their functional role in controlling olfactory representations. *A central hypothesis of this dissertation is that MCPO GABAergic neurons*

are recruited by a direct input from the piriform cortex, which serves to produce a fast top-down influence to local processing in the OB (**Figure 3**). I tested this hypothesis in three independent aims, in which we *(1)* identified the postsynaptic targets of MCPO GABAergic neurons in the OB and determined their impact on circuit function, *(2)* examined the connectivity of the piriform cortex with MCPO GABAergic neurons and studied the activity dynamics of MCPO GABAergic projections in the OB in response to odors in awake mice, and *(3)* characterized the cell type diversity among OB projecting MCPO GABAergic neurons.

Specific aim 1

Identify postsynaptic targets of BF GABAergic neurons within the OB and define the impact of this inhibitory input on the activity of the bulb output neurons. Previous neuroanatomical studies have suggested targets of MCPO GABAergic inputs onto the OB (Gracia-Llanes et al., 2010) and showed functional connections with GCs (Nunez-Parra et al., 2013), however, it remains unknown the full extent of axonal targeting of MCPO GABAergic neurons in the OB, their synaptic properties and how they impact the OB output neurons. As a step towards understanding these questions, we conducted targeted electrophysiological recordings across different neuronal types in OB slices, while optogenetically stimulating MCPO GABAergic axons to characterize postsynaptic inhibitory responses and to evaluate the circuit effects of this inhibition on the activity of MCs.

Specific aim 2

Examine the connectivity of piriform cortex excitatory neurons with MCPO GABAergic neurons and investigate the activity dynamics of MCPO GABAergic projections in the OB, in responses to odors in behaving mice. To date, the function of fast inhibitory inputs from MCPO GABAergic neurons in controlling olfactory representations remains unknown. A main question is whether the activity of these neurons is directly modulated by inputs from the piriform cortex during odor-driven behaviors. In the second aim of this dissertation, I used whole-cell electrophysiology and optogenetics to examine direct inputs from the PC onto OB projecting MCPO GABAergic cells and multiphoton calcium imaging in awake mice to investigate how the activity of MCPO GABAergic projections to the OB is modulated by odor stimuli and characterized their activity dynamics as a function of odor identity and concentration.

Specific aim 3

Determine the diversity of OB-projecting MCPO GABAergic neurons, their projections to the OB and their activation by piriform cortex excitatory inputs. The BF represents a heterogeneous collection of neurons with poorly defined connectivity. In the third aim of this dissertation, I examined the inhibitory inputs to the OB using whole-brain imaging and immunohistochemistry to characterize the subpopulation diversity of GABAergic neurons in the MCPO and their projections to the OB. In addition, using whole-cell electrophysiology and optogenetics I evaluated the targets of these projections

in the OB and the existence of specific inputs from PC to different MCPO populations of neurons.

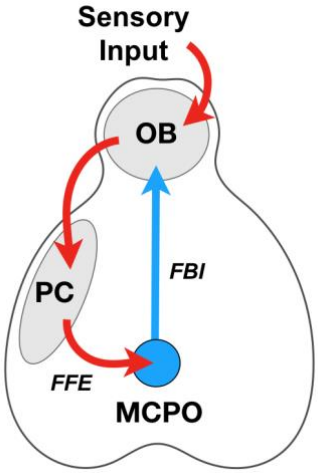

Fig. 3: *Schematic representation of the main hypothesis*

Stimulus-driven feedforward excitation in the olfactory bulb (OB) drives activation of the piriform cortex (PC), which in turn sends feedforward excitation (*FFE*) to the magnocellular preoptic area (MCPO) to recruit the activity of long-range GABAergic cells. In response to the stimulus-driven excitation (red arrows), MCPO GABAergic cells send feedback inhibition (*FBI*) to the OB to regulate ongoing early sensory processing (blue arrow).

Chapter 2

Long-range GABAergic inhibition modulates spatiotemporal dynamics of the output neurons in the olfactory bulb

Citation

Villar PS, Hu R and Araneda RC (2021). Long-Range GABAergic Inhibition Modulates Spatiotemporal Dynamics of the Output Neurons in the Olfactory Bulb. The Journal of Neuroscience. 41(14): 3610–3621.

Author contributions

P.S.V. and R.C.A. designed research; P.S.V. and R.H. performed research; P.S.V. and R.H. analyzed data; PV and R.C.A. wrote the paper.

Acknowledgments

We thank Drs. Rodrigo Andrade, Lucas Pozzo-Miller, Larissa Erben and Dinu F. Albeanu for their helpful comments, and former members of the Araneda laboratory for their technical assistance. This research was supported by the National Institute on Deafness and Other Communication Disorders, grant DCR01-DC-009817 and National Institute on Aging, grant AG-049937A of the National Institute of Health to Dr. Ricardo C. Araneda and National Science Foundation-Graduate Research Fellowships Program/Division of Graduate Education, grant 1322106 to Dr. Ruilong Hu.

Summary

Local interneurons of the olfactory bulb (OB) are densely innervated by long-range GABAergic neurons from the basal forebrain (BF), suggesting that this top-down inhibition regulates early processing in the olfactory system. However, how GABAergic inputs modulate the OB output neurons, the mitral/tufted cells, is unknown. Here, in male and female mice acute brain slices, we show that optogenetic activation of BF GABAergic inputs produced distinct local circuit effects that can influence the activity of mitral/tufted cells in the spatiotemporal domains. Activation of the GABAergic axons produced a fast disinhibition of mitral/tufted cells consistent with a rapid and synchronous release of GABA onto local interneurons in the glomerular and inframitral circuits of the OB, which also reduced the spike precision of mitral/tufted cells in response to simulated stimuli. In addition, BF GABAergic inhibition modulated local oscillations in a layer-specific manner. The intensity of locally evoked θ oscillations was decreased upon activation of top-down inhibition in the glomerular circuit, while evoked γ oscillations were reduced by inhibition of granule cells. Furthermore, BF GABAergic input reduced dendrodendritic inhibition in mitral/tufted cells. Together, these results suggest that long-range GABAergic neurons from the BF are well suited to influence temporal and spatial aspects of processing by OB circuits.

Introduction

The basal forebrain (BF), a brain region that supports wakefulness, attention and cognition (Anaclet et al., 2015; Xu et al., 2015; Ballinger et al., 2016), has an important role in the state-dependent regulation of sensory circuits (Yang et al., 2014b; Hangya et al., 2015; Zant et al., 2016). Among the diverse group of BF neurons, the largest population corresponds to GABAergic projection neurons (Sarter and Bruno, 2002). Yet, unlike the extensive insight on the function of the neighboring BF cholinergic neurons in sensory processing (Hasselmo, 1995; Linster and Cleland, 2002; Wilson et al., 2004; Parikh and Sarter, 2008; Hellier et al., 2012; Zaborszky et al., 2012; Chapuis and Wilson, 2013; Rothermel et al., 2014), the function of BF GABAergic projections in modulating sensory circuits is not understood. Recent evidence suggests GABAergic neurons provide an important parallel neuromodulatory output from the BF (Gritti et al., 2003; Henny and Jones, 2008; McKenna et al., 2013; Kim et al., 2015a; Yang et al., 2017). BF long-range GABAergic neurons (BF-LRGNs) influence the hippocampus and cortex by acting on local inhibitory circuits and modulating the generation of neuronal oscillations, which support essential aspects of the timing of neural activation in these structures (Freund and Antal, 1988; Freund and Meskenaite, 1992; Hangya et al., 2009; Melzer et al., 2012; Gonzalez-Sulser et al., 2014; Kim et al., 2015a). Network oscillations are prominent in the OB, the initial site for odor processing, and they are thought to provide a temporal structure for the encoding of odor information (Adrian, 1942; Macrides and Chorover, 1972; Beshel et al., 2007; Schaefer and Margrie, 2007; Junek et al., 2010). The role of local GABAergic neurons in the generation of network rhythms during odor discrimination tasks is well-

established (Stopfer et al., 1997; Fukunaga et al., 2014; Osinski and Kay, 2016). In addition, the OB local GABAergic circuits have been involved in decorrelation of principal neurons allowing for discrimination of similar odor (Abraham et al., 2010; Gschwend et al., 2015; Li et al., 2018). Thus, we hypothesize that by modulating local inhibitory circuits BF-LRGNs could influence odor processing in the OB. In agreement with this possibility, chemogenetic silencing of LRGNs of the magnocellular preoptic nucleus (MCPO), a main source of BF GABAergic inhibition to the OB (Gracia-Llanes et al., 2010), produces a notable reduction in the discrimination of similar odors (Nunez-Parra et al., 2013); however, how this BF inhibition influences neuronal circuits in the OB remains unclear.

Here, we used a combination of conditional genetics, immunohistochemistry, and electrophysiology in acute brain slices to define the physiological framework by which the BF GABAergic projections modulate, at the circuit level, the spatiotemporal dynamics of the output neurons in the OB. We first established that MCPO Gad2 neurons, which comprise the main inhibitory projections to the OB, appear phenotypically homogeneous, using GABA as the main transmitter, unlike other GABAergic neurons in the BF (Saunders et al., 2015; Case et al., 2017). In agreement with previous work (Gracia-Llanes et al., 2010), immunohistochemical analysis revealed that BF-LRGNs extensively innervate the granule cell layer (GCL) and to a lesser extent the glomerular layer. Consistent with this anatomical distribution, phasic activation of BF GABAergic axons, elicited fast inhibitory responses in local inhibitory neurons, including the granule cells (GCs) and periglomerular cells (PGCs); however, inhibitory responses were absent in the output neurons, the mitral and tufted cells (MC and TCs, respectively). Functionally, the selective activation of the GABAergic axons in the OB results in a disinhibitory effect of the output neurons;

activation of BF inhibition increased the firing rate of active MCs. We show that this increase in firing rate can result from a reduction in the inhibition by glomerular inhibitory neurons and by a reduction in dendrodendritic inhibition at GC-MC synapses. In addition, top-down inhibition decreased the spike precision of MCs in response to simulated sensory stimuli. Importantly, activation of BF GABAergic inputs produced a significant reduction in the power of local θ and γ oscillations, thus desynchronizing the rhythmic activity in the OB. Together, these results indicate that fast BF GABAergic inhibition is well suited to modulate early stages of odor processing by regulating spatiotemporal dynamics of MCs.

Methods

Animals. All experiments were conducted following the US National Institute of Health guidelines and approved by the Institutional Animal Care and Use Committee of the University of Maryland, College Park. For our experiments we used wild type C57BL/6 (JAX, stock #664) and *Gad2-IRES-Cre* mice (JAX, stock #010802) of both sexes, ranging in age from one to four months, from breeding pairs housed in our animal facility.

Stereotaxic injections. Deep anesthesia of *Gad2-Cre* mice was induced with 2% isoflurane at a rate of 1 L/min and adjusted (1-1.5%) over the course of the surgery. Body temperature was maintained using a heating pad. An intraperitoneal injection of carprofen (5 mg/Kg) was used as analgesic and a solution of povidone-iodine (Betadine) as antiseptic. During the surgery, eyes were lubricated using a petrolatum ophthalmic ointment (Paralube). GABAergic projection neurons in the basal forebrain were retrogradely labeled

using a unilateral injection of AAVrg-hSyn-DIO-eGFP in the OB (50 nL, Catalog #50457-AAVrg, Addgene), guided with a stereotaxic apparatus (Kopf, Catalog #940), and using the following stereotaxic coordinates (mm): −D/V 0.4, ±M/L 0.8, A/P +6. This retrograde injection in the OB sparsely labeled neurons in the anterior olfactory nucleus, as recently shown (Hanson et al., 2020). To express channelrhodopsin-2 (ChR2) in LRGNs, *Gad2-Cre* mice were bilaterally injected with AAV5-CAG-Flex-ChR2-tdTomato (200 nL, Catalog #18917, Addgene) in the MCPO region of the BF using the following stereotaxic coordinates (mm): D/V −5.4, M/L ±1.63, A/P +0.14. For histology experiments, the control virus AAV5-CAG-Flex-tdTomato (200 nL, Addgene) was used to anterogradely label MCPO GABAergic axons. For both retrograde and anterograde labelling of LRGNs, electrophysiological or histological experiments were conducted 3 weeks, or later, post-surgery.

Confocal imaging and immunofluorescence. To directly visualize the expression of the reporter gene (tdTomato or eGFP), mice were transcardially perfused with cold 4% PFA diluted in 0.1 M PBS, pH 7.4. Brains were then harvested and post fixed overnight at 4°C in the same fixative. Brain tissue was sliced in sections of 50 μm on a vibratome, the nuclei stained with DAPI (1:1500, Catalog #D1306, Invitrogen) and mounted in a solution of Mowiol-DABCO. Mowiol mounting media was made in batches of 25 mL containing 9.6% w/v mowiol (Catalog #475904, Millipore), glycerol 24% w/v, 0.2 M Tris (pH 6.8), 2.5% w/v DABCO (antifade reagent, Catalog #D2522, Sigma) and Milli-Q water. For immunofluorescence experiments, free floating brain sections (50 μm) were first blocked with donkey serum (10%, Catalog #S30-M, Millipore) in PBS supplemented with Triton

X-100 (0.1% v/v, Catalog #T8787, Millipore, PBS-T) for 1 h at room temperature to block unspecific biding sites. Samples were then incubated overnight at 4°C with a goat primary antibody anti-ChAT (1:500, Catalog #AB144, Millipore) and 2.5% donkey serum in PBS-T with gentle rocking. The primary antibody was then washed with PBS-T for at least 30 min before incubation with a donkey anti-goat antibody coupled to Alexa-647 (1:750, Catalog #A-21447, Invitrogen). Finally, slices were stained with DAPI, dried and mounted using Mowiol-DABCO. Control sections not exposed to the primary antibody were devoid of immunostaining and were used to set background values on the microscope. Images were acquired using a Leica SP5X confocal microscope, with appropriate brightness and contrast adjustments, and immunostained cells counted blindly using ImageJ (NIH).

Whole cell recordings. Patch clamp recordings in brain slices were conducted as previously described (Nunez-Parra et al., 2013) using a dual EPC10 amplifier (HEKA). Briefly, we used a vibratome (VT1000S, Leica) to obtain horizontal 250 μm slices. Sectioning was done using a cold low Ca^{2+} (0.5 mM) and high Mg^{2+} (3 mM) artificial cerebrospinal fluid solution (ACSF). Slices were then placed in normal Ca^{2+} and Mg^{2+} ACSF and left to recover for 30-45 min at 37°C. The normal ACSF had the following composition (in mM): 125 NaCl, 25 $NaHCO_3$, 1.25 NaH_2PO_4, 3 KCl, 2 $CaCl_2$, 1 $MgCl_2$, 3 myo-inositol, 0.3 ascorbic acid, 2 Na-pyruvate and 15 glucose, and it was continuously oxygenated with 95% O_2 and 5% CO_2. After recovery, slices were transferred to a recording chamber on an Olympus BX51W1 DIC microscope. Neurons were visualized using a 40x objective (LUMPlanFI/IR, Olympus). The evoked inhibitory postsynaptic currents (eIPSCs) were recorded at a holding potential of 0 mV using an internal solution

with the following composition (in mM): 125 Cs-gluconate, 4 NaCl, 10 Na-phosphocreatine, 10 HEPES-K, 2 Na-ATP, 4 Mg-ATP and 0.3 GTP. Alternatively, the eIPSCs were recorded at −70 mV using an internal solution of the following composition (in mM): 150 CsCl, 4.6 $MgCl_2$, 0.1 $CaCl_2$, 10 HEPES, 0.2 EGTA, 4 Na-ATP and 0.4 Na-GTP. The pH of internal solutions was adjusted to pH 7.3 with CsOH. Current clamp experiments were performed using pipettes filled with an internal solution of the following composition (in mM): 120 K-gluconate, 10 Na-gluconate, 4 NaCl, 10 HEPES-K, 10 Na-phosphocreatine, 2 Na-ATP, 4 Mg-ATP and 0.3 GTP, adjusted to pH 7.3 with KOH. In some experiments, $CaCl_2$ was replaced by equimolar amounts of $SrCl_2$ in the ACSF. No Ca^{2+} chelators were added to this solution. To confirm the identity of the recorded neurons, and morphological reconstruction, the fluorophore Alexa-594 (20 µM, Invitrogen) was included in the internal solution in a subset of experiments. Post-recording filled neurons were fixed overnight at 4°C in PFA 4% and mounted with Mowiol-DABCO. Neurons were imaged under a confocal microscope and reconstructed using Neurolucida (MBF Bioscience) or neuTube (Feng et al., 2015). Recordings were performed at room temperature (21°C). Patch pipettes were pulled using a horizontal puller (P-97, Sutter Instrument) from thick wall borosilicate glass capillaries (Sutter Instrument), having a resistance of ~3-6 MΩ. All chemicals were obtained from Sigma Aldrich. Drugs were prepared from stocks stored at −20°C and diluted into ACSF; gabazine (Catalog #1262, Tocris), mecamylamine hydrochloride (Catalog #2843/10, Tocris), atropine (Catalog #A0132, Millipore-Sigma), kynurenic acid sodium salt (Catalog #3694, Tocris).

LFP recordings and optogenetic stimulation. Local field potentials in the OB were recorded in 250 μm brain slices using 200-300 KΩ glass electrodes filled with ACSF. To induce oscillations in the OB, a brief stimulation (100 μA, 100 Hz during 50 ms) was delivered to the ON using a stimulus isolation unit (ISO-Flex, A.M.P.I) controlled by the amplifier. Olfactory sensory neuron (OSN) axon bundles were readily seen under DIC optic. For optogenetic stimulation of the GL or GCL a collimated LED (473 nm, Thor Labs) was used to deliver brief light pulses through a 40x objective focused on either layer (which were at least ~400 μm apart), controlled by a TTL pulse triggered by amplifier. The intensity of the light beam was adjusted depending on the level of ChR2 expression from 1-3 mW mm^{-2}, measured after the objective. Trials were alternated between control and optogenetic stimulation conditions.

Data analysis. Electrophysiology data was analyzed using the IgorPro (WaveMetrics) and MATLAB (MathWorks) software. Only events with fast current kinetics were included in the analyses (rise time <4 ms and decay time <100 ms). For the quantification of the currents elicited by light stimulation, we calculated the transferred charge by integrating the current within a 300 ms window following the end of the light pulse and subtracting the baseline charge before the light pulse. The decay time was measured by fitting a double exponential decay function to the current relaxation and computing the weighted time constant (τ_w) as $\tau_w = (a_1\tau_1 + a_2\tau_2)/ (a_1 + a_2)$, where a and τ are the amplitude and time constant of the first (1) and second (2) exponentials, respectively. The rise time was estimated by measuring the time elapsed from 10 to 90% of the current peak amplitude. The onset time was measured by fitting a sigmoid function from stimulus

onset to the response peak and then computing the maximum curvature point by solving the 4th derivative of the fitted curve set equal to zero (Fedchyshyn and Wang, 2007). Spike jitter was measured as total standard deviation of the timing of the action potential peaks (Mainen and Sejnowski, 1995; Gutkin et al., 2003). Spike-triggered averages were calculated using an average of the current stimuli corresponding to the 100 ms prior to each action potential. For LFP analysis, stimulus artifacts were digitally removed, and traces were filtered with a 2nd order 300 Hz Butterworth low-pass filter. Spectral analysis was then conducted using the Chronux toolbox (http://www.chronux.org) using a multitaper spectral estimation (Bokil et al., 2010), using a 250 ms moving window (shifted in 10 ms increments) and seven tapers (K= 7), permitting a time-bandwidth product of 2 (TW= 2). The LFP power was normalized with respect to the pre stimulation period (Winkowski et al., 2013; James et al., 2019). Normalized power spectra were averaged over a window of 1 s and over experiments for all conditions. γ power was averaged between 30 to 80 Hz, while θ power between 4 to 12 Hz. For the histograms of axonal density, the cellular layers of different field of views were aligned horizontally using the nuclear staining as a reference. Mean pixel intensity values were computed across the horizontal axis and normalized to the overall maximal intensity value. Data is shown as the mean ± S.E.M, unless otherwise specified. Statistical analysis was done using a two-tailed t-test and significance was set at $p<0.05$ (*= $p<0.05$, **= $p<0.01$). Statistical power was evaluated using G*Power (Faul et al., 2009).

Results

GABAergic neurons in the MCPO innervate inhibitory circuits of the OB

Previous studies have shown that OB projecting LRGNs are clustered in a lateral region of the BF, the MCPO (Gracia-Llanes et al., 2010). To broadly label these projections neurons we used *Gad2-Cre* mice, as the GABAergic marker Gad2 is abundantly expressed in the MCPO (Nunez-Parra et al., 2013). *Gad2-Cre* mice were injected with the anterograde virus AAV5-Flex-tdTomato in the MCPO (**Figure 1A**, diagram). In agreement with previous work (Gracia-Llanes et al., 2010; Nunez-Parra et al., 2013), this anterograde injection resulted in extensive labelling of fibers in the OB, with a distinct pattern of labelling across its cellular layers. Fluorescently labeled axons of LRGNs exhibited a non-uniform distribution pattern throughout all the layers of the OB, with dense labelling in the GCL and to a lower extent in the external plexiform layer (EPL) (**Figure 1A**). Similarly, there was significant innervation around juxtaglomerular neurons in the glomerular layer (GL) (mean normalized pixel intensity GL, 0.35 ± 0.07; EPL, 0.15 ± 0.02; GCL, 0.7 ± 0.09; n= 6 slices, 3 mice). At a cellular level, the GABAergic axons were characterized by thick and smooth processes running along the distinct cellular layers, with profuse ramifications and axonal boutons (**Figure 1B**, arrow heads).

To specifically access the population of OB-projecting GABAergic neurons in the MCPO we used an AAV variant that produces efficient retrograde labeling, the rAAV2-retro virus (Tervo et al., 2016; in 't Zandt et al., 2019). This virus was injected unilaterally into the OB of *Gad2-Cre* mice (**Figure 1C**, diagram). Approximately three weeks after

injection, transduced GABAergic neurons were abundant in the ipsilateral hemisphere and confined to the MCPO (**Figure 1C**). Recent work has shown that in the medial septum/diagonal band of Broca axis (MS/DBB), a subregion of the BF, some neurons express both GABAergic and cholinergic markers, suggesting that MCPO GABAergic neurons could exhibit a mixed phenotype (Saunders et al., 2015; Takács et al., 2018). To evaluate this possibility, we immuno-stained retrolabeled GABAergic MCPO neurons with an antibody directed against the enzyme choline acetyl transferase (ChAT), a cholinergic marker. As shown in Figure 1D, several putative cholinergic neurons are labeled in this region, however, we observed minimal labelling of ChAT protein among retrolabeled MCPO GABAergic neurons, with sections showing only a ~1 % of colocalization (GFP^+= 832 neurons; $ChAT^+$= 468; $GFP^+/ChAT^+$= 10; n= 12 slices, 3 mice). This observation is in agreement with a recent study showing absence of colocalization of OB projecting BF neurons with ChAT (Hanson et al., 2020). In contrast, when Cre-dependent expression of the fluorescent protein eGFP was achieved by direct transduction in the MCPO, 16.5% of Gad2 positive ($Gad2^+$) neurons displayed colocalization with the cholinergic marker, as previously reported (Saunders et al., 2015; Sanz Diez et al., 2019) (GFP^+= 510 neurons; $ChAT^+$= 423; $GFP^+/ChAT^+$= 84; n= 9 slices, 3 mice). Thus, although we cannot rule out the possibility of low levels of expression of ChAT that were undetected by our immunoassay, or the presence of other neurotransmitters released by $Gad2^+$ neurons, our data indicates that MCPO GABAergic neurons that project to the OB exhibit mostly a GABAergic phenotype (see also **Figure 3C**).

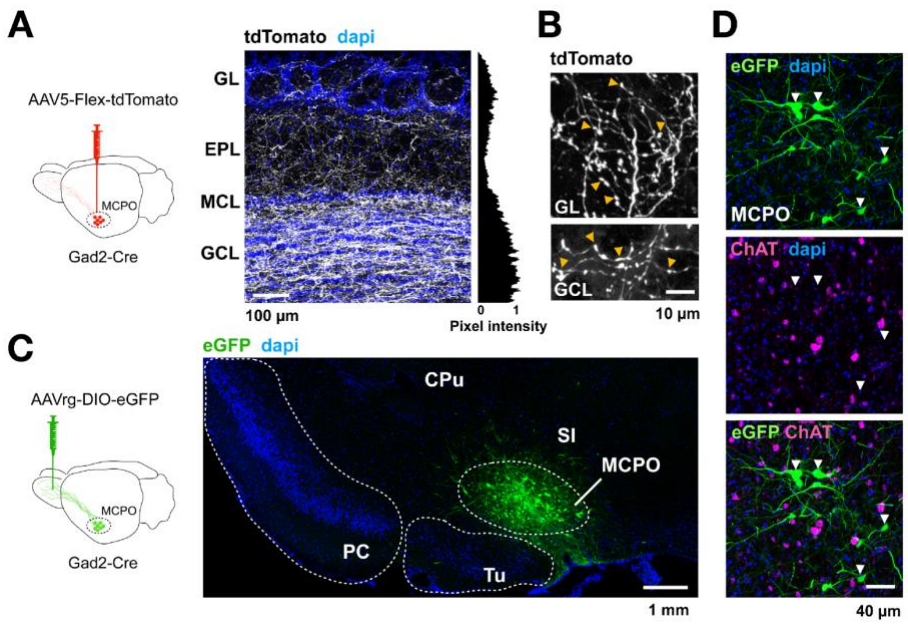

Fig. 1: *GABAergic projection neurons to the OB are clustered in the MCPO region of the BF and are different from cholinergic neurons*

(A) Left, diagram of the anterograde approach to label MCPO GABAergic neurons; a AAV5-Flex-tdTomato virus was injected in the MCPO of Gad2-Cre mice. Right, confocal image of a section of the main olfactory bulb (MOB; n= 6) showing the distribution pattern of Gad2-tdTomato axons (shown in white, to enhance the contrast of the staining) across the different cell layers, revealed by the nuclear dye dapi (blue). The mean normalized pixel intensity across layers is shown on the right. The densest distribution of Gad2 axons is found in the granule cell layer (GCL) and the glomerular layer (GL) of the MOB. MCL, mitral cell layer; EPL, external plexiform layer. **(B)** MCPO GABAergic axons innervating the GL (top) and GCL (bottom) exhibit numerous boutons (yellow arrowheads). **(C)** Left, diagram of the approach to retrogradely label the MCPO GABAergic neurons; a AAVrg-DIO-eGFP virus was injected unilaterally in the OB of Gad2-Cre mice. Right, confocal micrograph showing that transduced Gad2-eGFP positive neurons (green) are clustered in the MCPO (CPu, caudate putamen; PC, piriform cortex; Tu, olfactory tubercle; SI, substantia innominata; MCPO, magnocellular preoptic area). **(D)** High magnification confocal micrographs of the MCPO containing GFP transduced Gad2 neurons (green), immunostained with antibody against the cholinergic marker ChAT (magenta). Several neurons are positive for ChAT in the MCPO region; however, this representative image illustrates the lack of colocalization of the cholinergic marker and the GABAergic neurons retrolabeled from the OB (white arrowheads). Similar results were found in the accessory olfactory bulb and are shown in **Figure 1-1** (Appendix B).

Activation of LRGN produces a fast inhibition in local inhibitory neurons of the OB

We next examined the influence of endogenously released GABA from BF GABAergic axons in the most prominent components of the OB circuit. To selectively activate GABA release from GABAergic axons in the main OB (MOB), we expressed the light-gated cation channel channelrhodopsin-2 (ChR2) in the MCPO of *Gad2-Cre* mice and conducted targeted recordings from different cell types across the OB (**Figure 2**). We maximized the probability of detecting evoked GABA currents, by performing these recordings in symmetrical chloride conditions (see Methods), in which GABA elicits large inward currents. Light stimulation, reliably evoked short latency inhibitory postsynaptic currents (eIPSCs) in two of the most prominent inhibitory neurons of the MOB; the GCs and the PGCs (**Figure 2B**; onset: GCs, 6.8 ± 0.7 ms, n= 14; PGCs, 7.2 ± 1 ms, n= 5). The amplitude and kinetics of the currents was variable among these different cell types. Quantification of the transferred charge (see Methods) indicated that average inhibitory responses were significantly larger in the GCs (**Figure 2B**, GCs, −15.3 ± 5 pC, n= 16 vs PGCs, −2.4 ± 0.8 pC, n= 5; p= 0.02), and that GCs also exhibited eIPSCs with a slower decay time (GCs, 60.3 ± 7.2, ms n= 16 vs. PGCs, 31.7 ± 4.8 ms, n= 5, p= 0.04). Additionally, short-latency GABAergic responses were also observed in EPL medium-sized interneurons (EPL-I), which presumably correspond to the fast-spiking (FS) interneurons described in this region (EPL-I, −2.6 ± 2.2 pC, n= 3, **Figure 2A, B**) (Hamilton et al., 2005; Huang et al., 2013). In contrast, light stimulation failed to produce any detectable inhibitory current in the output neurons of the OB, the MCs and TCs (MCs, −0.4 ± 0.5 pC, n= 11; TCs, 0.2 ± 0.3 pC, n= 10). These results are consistent with a recent report

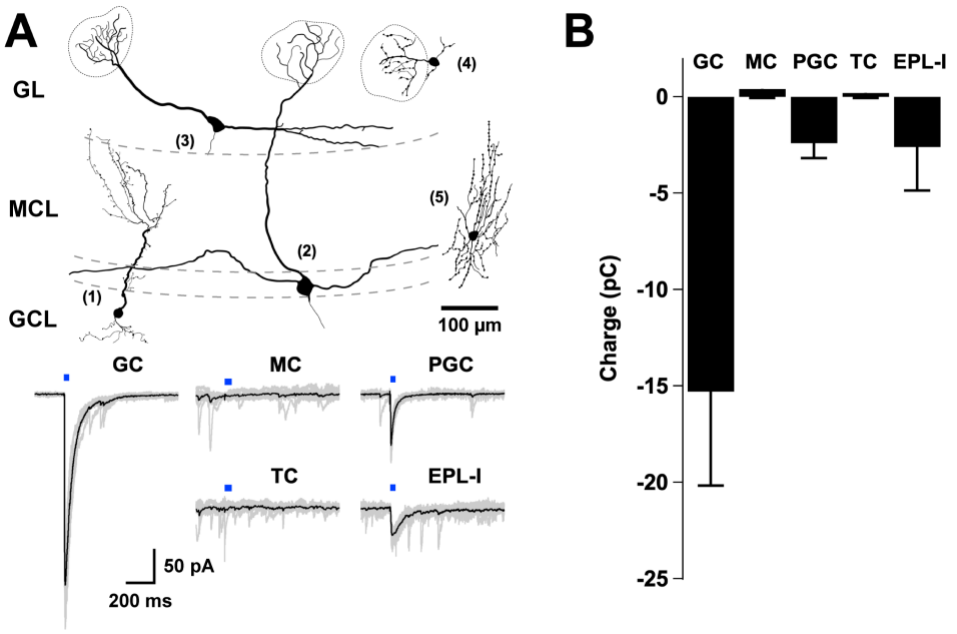

Fig. 2: *Inhibitory neurons are postsynaptic partners of MCPO long-range GABAergic neurons in the OB*

(A) Upper drawings, example of distinct reconstructed neurons, post-recording; 1, granule cell (GC); 2, mitral cell (MC); 3, tufted cell (TC); 4, periglomerular cell (PGC): 5, external plexiform layer interneuron (EPL-I). The morphology of the neurons was reconstructed from confocal images of fixed cells that were filled with Alexa Fluor-594 during the recordings. The scale bar is 100 µm. Bottom, example of eIPSCs recorded at −70 mV in symmetrical chloride conditions, upon stimulation of GABAergic axons expressing ChR2 with blue light (5 ms). LED stimulation elicited large inward currents in GC, PGC and EPL-I but not in output neurons, the MC or TC. **(B)** Bar graph showing the total charge transferred during the GABAergic eIPSCs in distinct cell types in the OB (GC, n= 16; MC, n= 11; PGC, n= 5; TC, n= 10; EPL-I, n= 3). Responses are observed in the main inhibitory types, but not in the output neurons.

that examined the targets of GABAergic neurons from a different region of the basal forebrain (Hanson et al., 2020). Additionally, BF GABAergic axons produced a similar pattern of labelling in the accessory OB (AOB), a region involved in pheromonal signal processing, with dense innervation of the GCL (**Figure 1-1A**). Similar to the main OB, GABA release from MCPO axons elicited eIPSCs only in the inhibitory cell types of the AOB (**Figure 1-1B**, C; GCs, −11 ± 4 pC, n= 12; PGCs, −5 ± 3.8 pC, n= 5; M/TCs, −0.9 ± 0.7 pC, n= 6). Together, these results indicate that, at the circuit level, BF inhibition functionally targets inhibitory but not excitatory neurons in the OB.

Synaptic activation of GCs by BF-LRGN input is synchronous and long-lasting

To further determine the impact of the BF inhibition onto the local inhibitory neurons, we examined the synaptic properties of MCPO inhibitory inputs onto GCs, which showed the densest innervation by LRGNs. GABA release in the OB was evoked from LRGN axon terminals expressing ChR2 by a brief light stimulation pulse (0.5-1 ms). The duration of the light stimulation was adjusted to reduce the probability of stimulating multiple axons simultaneously (achieving a ~40% failure rate). We termed this a minimally evoked IPSC (min-eIPSC) (Banks et al., 1998; Hagiwara et al., 2012). We recorded the min-eIPSC at 0 mV, using a Cs-gluconate based internal solution (see Methods), which allowed us to isolate the outward GABAergic currents, without affecting the function of local circuits using synaptic transmission blockers. Light stimulation elicited a short latency min-eIPSC (mean ± SD, 8.1 ± 2.8 ms, n= 5 cells), which occurred with a variable onset likely due to differences in axonal geometry and the short duration of the stimulation

(**Figure 3A**). The average amplitude of the min-eIPSC was 66 ± 3 pA (**Figure 3A**), with kinetics characterized by a fast rise time (10-90 % of the peak, 1.6 ± 0.1 ms) and a slower decay time (50.6 ± 1.8 ms) (**Figure 3B**). The min-eIPSC amplitudes exhibited a bimodal distribution, having a small amplitude peak (mean ± SD, 48 ± 15 pA) and a larger peak (mean ± SD, 100 ± 31 pA). Most of the events had fast rise times (75% <2 ms), which included the majority of the larger amplitude events, with a smaller number of events (~25%) having slower rise times. The events of larger amplitude and faster rise time may reflect a predominant perisomatic targeting of the MCPO input onto GCs, while the smaller amplitude and slower rise time event reflecting more distal GABAergic inputs (**Figure 1A**, **Figure 3B**, left). In contrast, the decay times showed a monophasic distribution due to their longer time course and thus subjected to less apparent filtering (**Figure 3B**, right). Interestingly, the decay time of the evoked min-IPSC from MCPO axons is relatively slow compared to the IPSCs driven in GCs by local GABAergic neurons such as the deep short-axon cells (dSAC, τ~10 ms) (Eyre et al., 2008). The min-eIPSC decay time in GCs is also slower than the decay time of spontaneous IPSCs from GC activity recorded in MCs under similar conditions (23 ± 0.7 ms, n= 51, not shown). The relatively slower current relaxation of the BF GABAergic inputs suggests they have a longer temporal influence in GCs compared with the influence of local inhibition. Importantly, while the light-elicited currents were completely abolished by the $GABA_AR$ blocker gabazine (Gbz; control −89 ± 21 pC vs. Gbz, 0.3 ± 1.5 pC, n= 3, p= 0.04), they were unaffected by a mixture of the cholinergic receptor blockers, mecamylamine (MM) and atropine (Atrp) (control −141 ± 55 pC vs. cholinergic blockers, −130 ± 62, p= 0.25, n= 5), further indicating that MCPO inputs onto GCs are mostly GABAergic (**Figure 3C**).

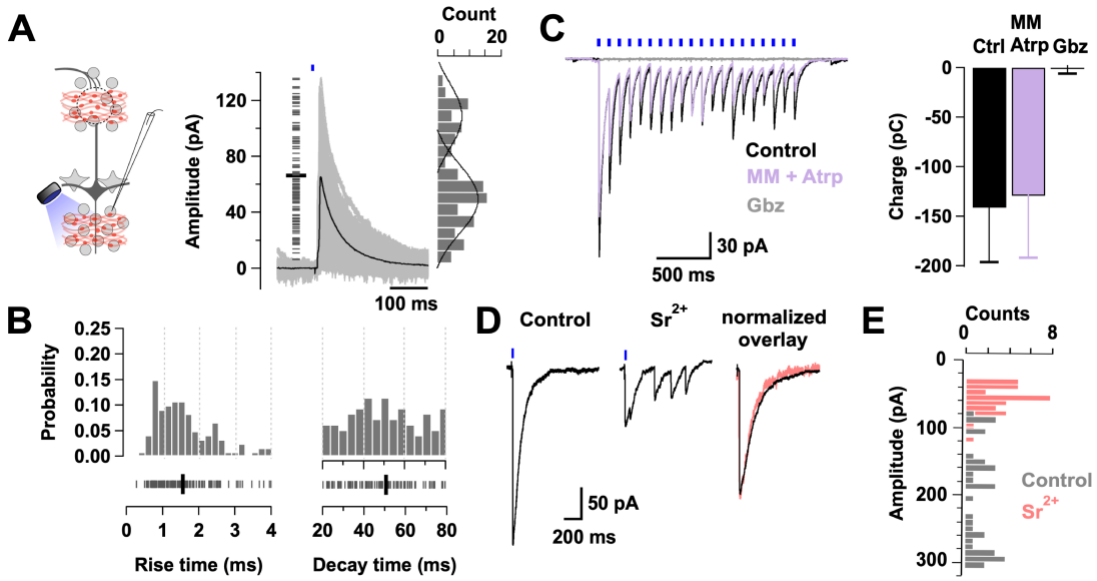

Fig. 3: *Synaptic properties of the BF long-range GABAergic inputs onto GCs*

(A) Left, diagram of the experimental configuration; GCs were recorded in voltage clamp, while GABAergic axons expressing ChR2 were stimulated with a brief pulse of light (0.5-1 ms). Right, overlay of selected inhibitory postsynaptic currents evoked with minimal stimulation (min-eIPSCs, gray traces) in GCs (n= 5 cells, 3 mice). Only min-eIPSCs with rise times of less than 4 ms are included (n= 120 events, 5 cells). The short gray lines on the left correspond to the amplitude of single events. The min-eIPSC had an average amplitude of 66 ± 3 pA (thick black line). The amplitude histogram of the min-eIPSCs is shown on the right. Amplitudes show a bimodal distribution with a small peak centered at 48 pA and a higher peak at 100 pA. The black lines correspond to the fitting of two gaussian distributions to the amplitude distribution. **(B)** Probability distribution histograms for the rise time (left, 10-90% of the peak) and decay time (right, τ_w) of the min-eIPSC events shown in A. An equivalent number of events were taken from each cell (median 26). The ticks at the bottom correspond to the values for each event. The average rise time (1.6 ± 0.1 ms) and decay time (50.6 ± 1.8 ms) are shown by thick black lines. **(C)** Evoked IPSCs (eIPSCs) recorded in GCs, using a CsCl based internal solution, in response to LED stimulation (5 ms, 10 Hz). At this frequency of stimulation, the peak decreases in time but each eIPSC appear synchronous throughout the train (black traces). The eIPSCs are unaffected by the perfusion of a mixture of the cholinergic blockers mecamylamine (MM, 10 µM) and atropine (Atrp, 3 µM) (purple trace; n= 5, p= 0.25), but completely blocked by the $GABA_AR$ blocker gabazine (Gbz, 10 µM) (gray trace; n= 3, p= 0.04). **(D)** Left, light evoked IPSCs in GCs are desynchronized by the equimolar replacement

of calcium by strontium (Sr^{2+}, 2 mM). Right, overlay of peak normalized IPSCs for control (black) and strontium (pink) showing similar kinetics. The holding potential in C and D is −70 mV. **(E)** Histogram overlaying the eIPSC amplitudes during control (gray) and strontium (pink) application (n= 3 cells).

Synchronized vesicular release is a common feature of evoked neurotransmission in the nervous system and accounts for phasic synaptic transmission, while asynchronous release provides persistent neurotransmitter release favoring delayed transmission (Atluri and Regehr, 1998; Hefft and Jonas, 2005; Südhof, 2013; Wen et al., 2013; Kaeser and Regehr, 2014). Our data indicates that MCPO inputs produce a fast-synchronized release of GABA onto GCs, as light stimulation of MCPO axons with a single pulse, or across a high frequency stimulation train, always evoked currents that decay monotonically (**Figure 3A, C, D**). Accordingly, equimolar replacement of the extracellular Ca^{2+} by Sr^{2+}, a divalent ion that disrupts synchronized vesicular release (Dodge et al., 1969; Goda and Stevens, 1994; Xu-Friedman and Regehr, 2000; Shin et al., 2003), resulted in a barrage of smaller current events upon light stimulation (**Figure 3D**, left). In normal Ca^{2+}, the eIPSC had a mean amplitude of 191 ± 12 pA, while in the presence of Sr^{2+} the current amplitude was significantly lower (mean 54 ± 4 pA, $p<0.001$, n= 3) (**Figure 3E**). Importantly, in agreement with a quantal mechanism of release at these synapses, the kinetics of eIPSC evoked in the presence of Sr^{2+} closely resembled the kinetics of those in normal Ca^{2+} (**Figure 3D**, right) (rise time, in Ca^{2+}, 1.52 ± 0.3 ms vs. in Sr^{2+}, 1.85 ± 0.1 ms, p= 0.3; decay time, in Ca^{2+}, 63.6 ± 2 ms vs. in Sr^{2+}, 60.5 ± 3 ms, p= 0.43, n= 3). Together these results suggest that activation of BF-LRGNs axons in the OB produces a fast-synchronous release of GABA onto GCs, likely from multiple synaptic contacts.

Activation of BF-LRGNs disinhibit MCs and modulates the extent of lateral inhibition

We next examined the influence of the fast and synchronous GABA release onto the local inhibitory networks of the OB by BF-LRGN. In the glomeruli, local GABAergic neurons drive feedforward inhibition onto MCs, providing a mechanism for sensory gain control and decorrelation of odor representations (Wilson and Mainen, 2006; Zhu et al., 2013b; Banerjee et al., 2015). Thus, inhibition of PGCs by BF-LRGNs (**Figure 2**) suggests that BF inhibition can modulate the extent of feedforward inhibition in glomerular domains. To examine this possibility, we evoked activity in MCs by stimulating the axons of OSNs in the olfactory nerve (ON), while locally stimulating GABA release from BF-LRGNs axons in the GL (**Figure 4A**, diagram). Stimulation of the ON produced a long-lasting depolarization in MCs, with sustained firing of action potentials (**Figure 4A**), which was significantly increased by simultaneous light stimulation of BF-LRGNs axons in the GL, in agreement with the disinhibitory effect on this afferent input (firing rate, control: 3.5 ± 1.7 Hz, + LED: 6.4 ± 1.4 Hz, n= 4, p= 0.014) (**Figure 4B**). We next recorded simultaneously excitatory and inhibitory currents in MCs evoked by ON stimulation, using symmetrical chloride, at a holding potential of −60 mV (**Figure 4C**). The ON stimulation evoked a large inward current consisting of a barrage of glutamatergic and GABAergic events which was reduced ~60 % by light stimulation directed to the GL (control, −137 ± 20 pC; +LED, −53 ± 15 pC; n= 10, p<0.001) (**Figure 4D**). In agreement with the possibility that the reduction in the inward current by light stimulation was mostly due to a reduction of the GABAergic component, blockade of $GABA_A$Rs produced a similar reduction (~57

%) in the current evoked by ON stimulation (control: −182 ± 30 pC, Gbz: −73.5 ± 11 pC, n= 4, p= 0.003).

The ON-evoked response recorded in MCs was not affected by bath perfusing the type 1 and 2 dopaminergic receptor (DAR) antagonists Sulpiride (100 µM) and SCH39166 (10 µM), respectively (control −170 ± 34 pC; DAR antagonists −180 ± 37 pC; n= 10, p= 0.62) (**Figure 4-1A, B**). Correspondingly, the reduction of the ON-evoked response in MCs by light stimulation of BF-LRGNs axons persisted in the presence of DAR antagonists (control, −104 ± 26 pC; LED + DAR antagonists, −27 ± 7 pC; n= 6, p= 0.01) (**Figure 4-1C, D**). Lastly, the ON evoked current was completely abolished in the presence of gabazine and the broad glutamate receptor blocker kynurenic acid (1 mM) (control: −142 ± 32 pC, + blockers: −6.7 ± 4.5 pC, n= 6, p= 0.01). These results are consistent with an inhibitory control of LRGNs on glomerular GABAergic neurons targeting MCs.

Dendrodendritic inhibition (DDI) at MC-GC synapses is thought to shape the output signal of MCs both in the temporal and spatial domains, through recurrent and lateral inhibition (Yokoi et al., 1995; Isaacson and Strowbridge, 1998; Christie et al., 2001; Shepherd, 2004). Therefore, we next examined how BF inhibition shapes the responses of MCs, by locally stimulating GABA release from MCPO axons in the GL and GCL. We depolarized MCs by constant current injection to produce a low firing rate (~4Hz, **Figure 4E**). In agreement with a disinhibitory action of the BF afferent input, via inhibition of GCs, light stimulation directed to the GCL significantly increased the basal firing rate in

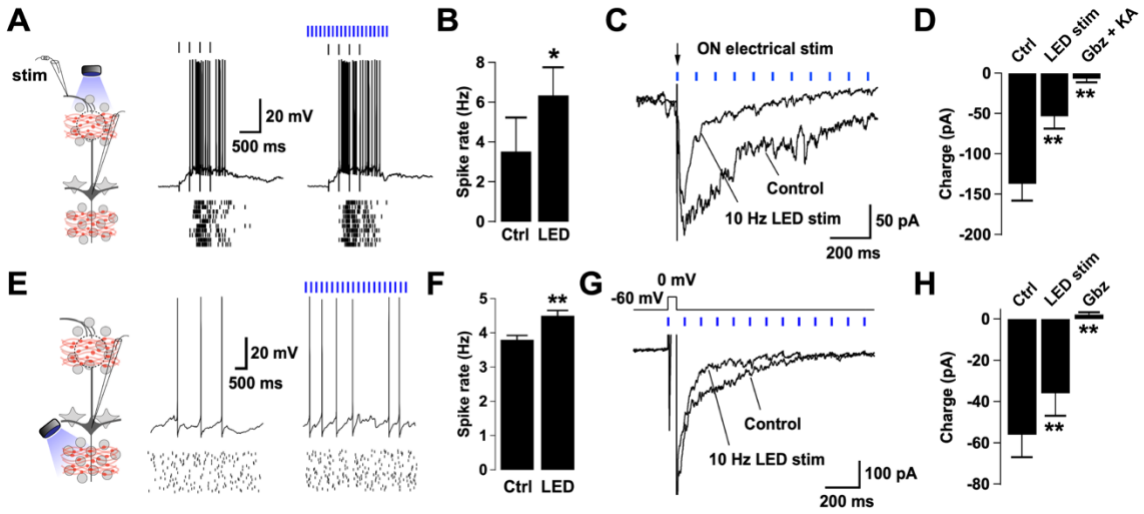

Fig. 4: *Activation of BF GABAergic inputs disinhibits mitral cells and reduces dendrodendritic inhibition*

(A) Left, diagram of the experimental configuration; MCs where recorded either in current or voltage clamp while the sensory axons in the olfactory nerve (ON) were activated by electrical stimulation. BF GABAergic axons expressing ChR2 were activated by blue light in the GL. Right, responses in a representative MC recorded while stimulating the ON with a glass electrode (100 μA, 100 μs, 4 Hz, top black ticks) in the presence (left) or absence (right) of LED stimulation (at 10 Hz, blue ticks). The stimulus intensity was adjusted to elicit firing in the MC. Bottom, spike raster plots for 10 trials in the cell shown above. The membrane potential was −57 mV (with zero current injection). **(B)** Summary bar graphs for spike frequency showing a significant increase in the firing rate during the LED stimulation compared to control (n= 4, p= 0.01). **(C)** Synaptic currents evoked in a MC by electrical stimulation of the ON (100 μA, 100 μs, arrow). Recordings were performed in symmetrical chloride, in which excitatory and inhibitory currents are seen as inward deflections. A single ON stimulation produced a long-lasting inward current, which was reduced in the presence of LED stimulation in the GL (blue ticks). The holding potential is −60 mV. The scale bar is 200 ms and 50 pA. **(D)** The large barrage of evoked synaptic activity by the ON stimulation is greatly suppressed by LED stimulation (n= 10, p<0.001), and completely abolished by blockers of $GABA_A$ and glutamate receptors (Gbz, 10 μM; kynurenic acid, KA, 1 mM, respectively; n= 6, p= 0.01). **(E)** Left, diagram of the experimental arrangement; MCs were recorded either in current or voltage clamp while LED stimulation was directed to the GCL. Right, voltage traces of a representative MC held at peri-threshold membrane potential in control and in the presence of LED stimulation (4 Hz). Spike raster plots for 20 trials are shown

in the traces below. **(F)** Summary bar graphs for spike frequency showing a significant increase in the firing rate during the LED stimulation compared to control (n= 6, p= 0.004). Light directed to the GL did not significantly change the firing rate of MCs. Results are shown in **Figure 4-2A, B** (Appendix B). **(G)** Overlaid of average current traces showing dendrodendritic inhibition on a MC evoked by a short depolarization (0 mV, 50 ms) in control and in the presence of LED stimulation (10 Hz). The holding potential is −60 mV. **(H)** Summary bar plot showing a significant difference in the synaptic charge transferred in control versus during LED stimulation (n= 8, p= 0.003). Consistently, Gbz (10 μM) completely blocked the evoked dendrodendritic current in MCs (n= 10, p= 0.0002). The reduction of the ON-evoked response and depolarization induced inhibition in MCs by light stimulation of BF-LRGNs axons persisted in the presence of dopamine receptor antagonists. These results are shown in **Figure 4-1** (Appendix B). In addition, light stimulation of the GL significantly reduced dendrodendritic inhibition in MCs, shown in **Figure 4-2C, D** (Appendix B).

MCs (control, 3.8 ± 2.3 Hz; +LED, 4.5 ± 2.5 Hz; n= 6, p= 0.004) (**Figure 4F**), but not when the light was focused in the GL (control, 4.3 ± 0.9 Hz; +LED, 5.2 ± 1.1 Hz; n= 7, p= 0.3) (**Figure 4-2A, B**). To directly examine the modulation of DDI by BF inhibition, we recorded the GABAergic currents evoked by a depolarizing pulse in MCs while holding the cells at −60 mV (**Figure 4G**). A brief stimulation (50 ms) elicited a barrage of GABAergic currents with a relaxation time of 640 ± 230 ms (n= 8) similar to the values previously described (Isaacson and Strowbridge, 1998; Schoppa, 1998). In the presence of local stimulation of GABA release from BF-LRGNs axons directed to the GCL, the DDI was significantly reduced (**Figure 4G, H**) (control, −56 ± 11 pC, LED stimulation, −36 ± 11 pC, n= 8, p= 0.003). Similarly, light stimulation of the GL produced a reduction in the current evoked in MCs during a depolarizing step (control, −102 ± 23 pA; +LED, −54 ± 19 pA, n= 5, p= 0.007) (**Figure 4-2C, D**). As expected, blocking $GABA_A$Rs completely abolished the evoked DDI in MCs (control, −52 ± 14 pC; Gbz, 2 ± 1 pC; n= 10, p<0.001). These results suggest that activation of BF-LRGNs can reduce the extent of DDI in MCs

and thus can influence odor processing by reducing lateral inhibition. Importantly, activating BF-LRGNs did not produce a change in the membrane potential of MCs (control, −64.5 ± 2 mV; +LED, −64.3 ± 2 mV; n= 6; p= 0.3).

BF-LRGNs modulate θ and γ oscillations in a layer specific manner

Inhibition from local GABAergic circuits contributes to generate a temporal framework in which low and high frequency neuronal oscillations exist in the OB (Kay et al., 2009; Wachowiak, 2011). Although the underlying mechanism is not completely understood, oscillations in the θ frequency band (2-12 Hz) entrained by the respiratory cycle, are orchestrated by PGCs (Lagier et al., 2004; Fukunaga et al., 2014), while γ oscillations (25-85 Hz) require the activation of GCs (Rall and Shepherd, 1968; Balu et al., 2007; Lagier et al., 2007; Kay, 2014). Since a main target of BF inhibition are the PGCs and GCs, we hypothesized that BF GABAergic inhibition could differentially influence the generation of oscillatory activity in the OB by regulating the activity of the glomerular and infra-mitral inhibitory circuits. To examine this possibility, we recorded the local field potentials (LFPs) evoked by stimulation of the ON (Lagier et al., 2007), while optogenetically inducing GABA release from MCPO GABAergic axons (**Figure 5A**, diagram). A brief, high frequency, electrical stimulation of the ON (100 Hz, 50 ms) elicited both slow and fast fluctuations in the LFP, that persisted for ~1 s following the cessation of the ON stimulation (**Figure 5B-C**). Frequency analysis of the LFP signals revealed that both θ and γ oscillations concurred; they were apparent in both the raw and filtered LFP traces (**Figure 5B-D**, **Figure 5-1**). Importantly, when the MCPO GABAergic axons were

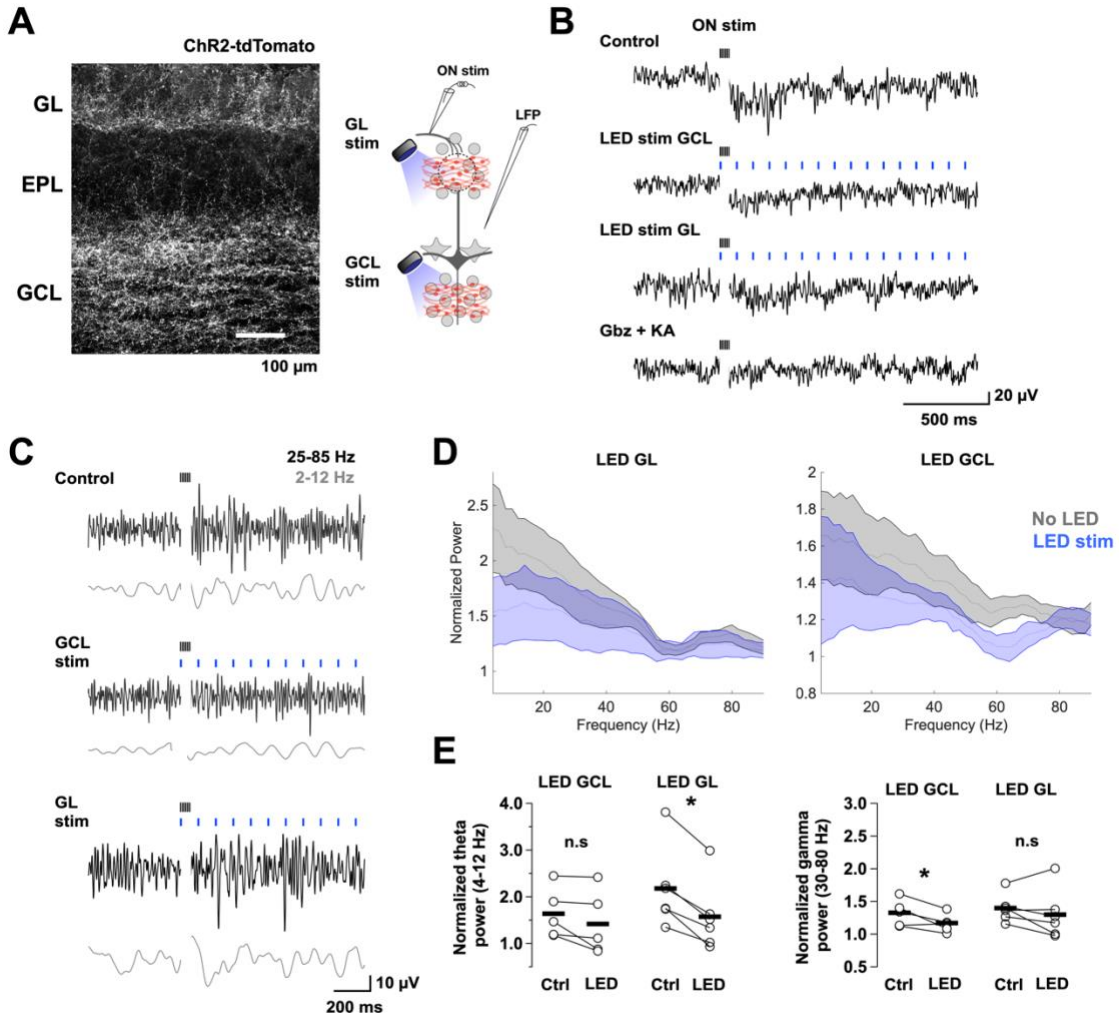

Fig. 5: *Layer specific modulation of local field potential oscillations by activation of BF GABAergic inputs*

(A) Left, image of a recorded section of OB showing expression of ChR2-tdTomato achieved by an injection of AAV5-Flex-ChR2-tdTomato virus in the MCPO. Right, diagram of the experimental configuration; a low resistance patch electrode was placed in the external plexiform layer (EPL) to record the local field potential (LFP) in OB slices containing BF GABAergic axons expressing ChR2. Oscillatory activity was elicited by stimulating the olfactory nerve (ON) with a brief high frequency stimulus (100 µA, 100 Hz for 50 ms). In alternate trials, we stimulated the BF GABAergic axons with a blue LED (5 ms, 10 Hz for 2 s) directed to the GCL or the GL using a 40x objective focused ~400 µm apart. **(B)** Raw traces of LFP recordings in the EPL during electrical stimulation of the ON (black ticks) in control

(upper trace), with LED stimulation over the GCL (blue ticks, middle trace) or the GL (bottom trace), and in the presence of the synaptic blockers kynurenic acid (KA, 1 mM) and Gbz, 10 μM). **(C)** Band pass filtered LFP traces for the different conditions; low frequency, 2-12 Hz (θ, grey), and high frequency, 25-85 Hz (γ, black). **(D)** Mean normalized 300 Hz low pass power spectra for a 1 s window of LFP recording during GL (left) and GCL (right) LED stimulation. Power was normalized respect to the pre ON stimulation period. The power spectra show significant activity below 20 Hz, as well as a shoulder at higher frequency. **(E)** Pair comparison of the normalized power of the θ (upper plots) and γ frequency bands (lower plots) in the absence (control) and presence of light stimulation (LED). Light stimulation in the GL significantly reduced the power of the θ band (n= 6, p= 0.001), but not the γ band (n= 6, p= 0.31), while LED stimulation in the GCL significantly reduced the power of the γ band (n= 5, p= 0.05), but not the θ band (n= 5, p= 0.11). Representative raw power spectrograms before and after ON stimulation, as well normalized power spectrograms in the presence of synaptic blockers are shown in **Figure 5-1** (Appendix B).

locally stimulated in the GL, the power of θ was significantly reduced (θ: control 2.17 ± 0.4, LED 1.56 ± 0.3, n= 6, p= 0.001). We also observed a trend towards a lower γ power, albeit this was not significant (γ: control 1.4 ± 0.1, LED 1.3 ± 0.2, n= 6, p= 0.31) (**Figure 5D-E**). In contrast, when the light stimulation was directed to the GCL, the power of γ, but not θ, was significantly reduced (θ: control 1.64 ± 0.2, LED 1.42 ± 0.3, n= 5, p= 0.11; γ: control 1.33 ± 0.1, LED 1.17 ± 0.1, n= 5, p= 0.05) (**Figure 5D-E**). These results suggest that the BF-LRGNs could differentially regulate the dynamics of local GABAergic circuits in the GL and GCL. We note that LED stimulation alone, in either GL or GCL, failed to induce significant changes in the LFP, owing perhaps to the low activity of inhibitory circuits in the slice. Nevertheless, a mixture of the excitatory and inhibitory synaptic blockers, kynurenic acid and gabazine, completely abolished the electrically induced oscillations, in agreement with their synaptic origin (θ: control 2.2 ± 0.2, blockers 0.9 ± 0.01, n= 4, p= 0.01; γ: control 1.45 ± 0.06, blockers 1 ± 0.02, n= 4, p= 0.01) (**Figure 5B**, **Figure 5-1B**).

Activation of BF-LRGNs inputs decreases spike precision in MCs

In other brain regions, long-range GABAergic inhibition influences rhythmic activity through direct modulation of local GABAergic interneurons, which in turn can regulate the precision of firing of principal neurons (Tamamaki and Tomioka, 2010; Melzer et al., 2012; Kim et al., 2015a). In the MOB spike precision in MCs can be regulated by inhibition from GCs (Schoppa, 2006), a main target of BF inhibition; therefore, we next examined how BF inhibition modulates spike precision of MCs. We simulated the occurrence of coincident sensory inputs of increasing synchrony onto MCs, overlaid on a 4 Hz respiration-like wave. The currents that produced the simulated excitatory postsynaptic potentials (sim-EPSPs) were adjusted to elicit a similar firing rate across trials (**Figure 6A**, top current trace) and the first 4 and last 4 stimuli were averaged to represent lower and higher synchrony, respectively. Under control conditions, the jitter in the spiking generated by the low synchrony sim-EPSCs was higher, compared to the high synchrony sim-EPSCs; in other words, the spike precision is higher with the high synchrony stimuli (Rodriguez-Molina et al., 2007) (**Figure 6A**, lower traces; low synchrony 34 ± 2.3 ms vs. high synchrony 18.9 ± 2.2 ms; n= 7, p= 0.02). As expected, the overall firing rate of MCs during the sim-EPSPs significantly increased when the MCPO GABAergic axons were locally stimulated with light (**Figure 6B**; control 7.2 ± 1.1 vs. + LED 8.3 ± 1.3 Hz, n= 7, p= 0.02). Importantly, optogenetic activation of BF-LRGNs axons significantly increased spike jitter in MCs for sim-EPSCs at both low and high synchrony (**Figure 6C**, low synchrony: control 34 ± 2.3 ms vs. LED stim 38.7 ± 2 ms, n= 7, p= 0.02; high synchrony:

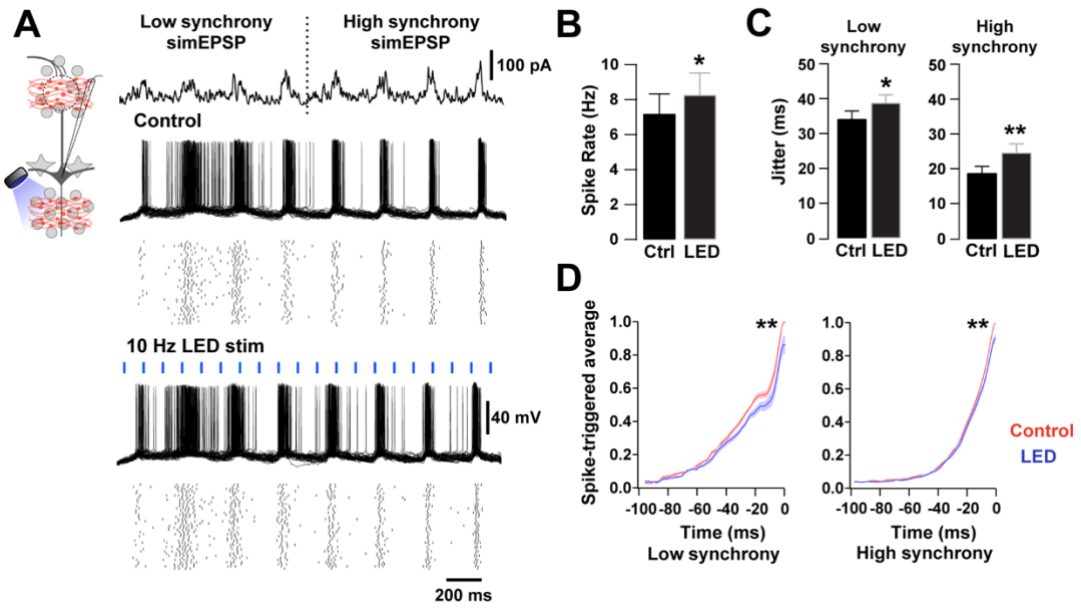

Fig. 6: *Activation of BF GABAergic inputs desynchronizes MCs*

(A) Left top, diagram of the experimental configuration; MCs were recorded in current clamp while axons of BF GABAergic neurons expressing ChR2 were locally activated in the GCL by blue light (5 ms, 10 Hz). MCs were stimulated with fluctuating currents that simulate sensory input of increasing synchrony on a 4 Hz sine wave (upper trace). The simulated current injection had low (first 4 current bursts) and high synchrony (last 4 current bursts). Overlaid voltage traces from a MC held at −60 mV in response to the current stimuli, during control (upper traces) and blue light stimulation (LED 5ms, 10 Hz, lower traces). Raster plots underneath show single cell responses in 40 trials. **(B)** The overall firing rate of MCs was significantly increased in the presence of blue light stimulation (n= 7, p= 0.02). **(C)** The spike jitter was significantly increased during low synchrony and high synchrony simulated sensory inputs in the presence of blue light stimulation (low synchrony, p= 0.02; high synchrony, p<0.001). **(D)** Spike-triggered average during low synchrony (left) and high synchrony (right) in the presence (red) or absence (blue) of blue light stimulation. The peak current needed to elicit spikes was smaller in the presence of blue light stimulation (low synchrony peak: p<0.001; high synchrony peak: p<0.001).

control 18.9 ± 2.2 vs. LED stim 24.7 ± 2.6 ms, n= 7, $p<0.001$). Additionally, the current needed to evoke a spike in MCs, across all sim-EPSPs, was significantly reduced in presence of light stimulation, in agreement with the disinhibitory action of the MCPO GABAergic inputs (**Figure 6D**, low synchrony peak: $p<0.001$; high synchrony peak: $p<0.001$). Together, these results indicate that MCPO GABAergic inhibition of local circuits results in disinhibition of MCs and a decrease in the firing precision of the output neurons.

Discussion

We provide new mechanistic insights on how long-range GABAergic inhibition shapes early sensory processing by influencing local inhibition in the OB. BF inhibition directly regulates local inhibitory neurons, including the GCs and PGCs, producing a net disinhibition of the OB output neurons (**Figure 1-3**). This disinhibition affected the function of MCs at two levels; in the temporal domain, activation of BF inhibition produced a phasic increase in the firing of MCs and a decrease in their spiking precision (**Figure 4, 6**). Additionally, activation of LRGNs reduced the extent of dendrodendritic inhibition at GC-MC synapses, suggesting that top-down GABAergic inhibition can also regulate MCs function in the spatial domain (**Figure 4**). At the circuit level, activation of the GABAergic feedback produced a specific modulation of inhibition across the glomerular and GC layers. Phasic activation of BF-LRGNs resulted in modulation of the intensity of θ and γ band oscillations across these two layers (**Figure 5**). Thus, phasic activation of BF long-range

GABAergic inhibition is poised to influence both the spatial and temporal aspects of early olfactory processing.

The MCPO is the most important source of GABAergic projections to the OB, however the function of these inhibitory neurons has been difficult to assess due to the presence of other cell types in the BF, including cholinergic and glutamatergic neurons (Zaborszky et al., 2012; Yang et al., 2017). Our functional and neuroanatomical studies provide direct evidence that MCPO GABAergic projections to the OB use GABA as a main transmitter. The cholinergic marker ChAT was not present in MCPO GABAergic neurons, and the fast-inhibitory currents elicited by their activation were insensitive to cholinergic antagonists. Thus, although we cannot rule out the possibility that ChAT is expressed at low levels in OB projecting MCPO neurons, undetected by our immunoassay, or that MCPO $Gad2^{+}$ neurons can release other neurotransmitters (Trudeau and El Mestikawy, 2018), our evidence supports a main GABAergic phenotype for these neurons. Phasic activation of MCPO GABAergic neurons produce a fast inhibition in local OB inhibitory neurons, which distinguish them from a different subtype of BF projection neurons previously described (Saunders et al., 2015; Case et al., 2017).

Functionally, fast MCPO GABAergic inhibition shapes the OB output by regulating local inhibitory circuits, instead of directly acting on the output neurons. LRGNs preferentially elicit GABAergic currents on inhibitory neurons in both MOB and AOB. Although, it is possible that small responses could exist in the output neurons, as recently suggested (Böhm et al., 2020). However, this study did not specifically target the MCPO, furthermore the absence of responses in MCs in our studies is also consistent with neuroanatomical studies indicating that BF GABAergic afferents only target inhibitory

neurons in the OB (Gracia-Llanes et al., 2010). This bias towards GABAergic targets has been reported for other long-range inhibitory projections in the brain (Freund and Antal, 1988; Gulyás et al., 1990, 1991; Freund and Gulyás, 1991; Martínez-Guijarro and Freund, 1992; Melzer et al., 2012; Caputi et al., 2013; Gonzalez-Sulser et al., 2014). The function of this biased pattern is unknown, however, given the essential participation of inhibitory circuits in network synchronization (Buzsáki and Chrobak, 1995), it has been proposed that long-range GABAergic inhibition modulates temporal dynamics in target circuits (Hangya et al., 2009; Kim et al., 2015a; Viney et al., 2018). We found that fast feedforward inhibition of local GABAergic neurons by BF-LRGNs decreases the intensity of evoked θ and γ band oscillations in the OB, through direct activation of $GABA_AR$ in a circuit specific manner. Oscillations are inherent to olfaction (Kay et al., 2009), and underlie fine odor discrimination and high cognitive tasks (Stopfer et al., 1997; Nusser et al., 2001; Beshel et al., 2007). Interestingly, disruption of $GABA_AR$ in GCs increases γ oscillations (Nusser et al., 2001), further supporting the possibility that inhibition of GCs influences synchronized activity in the OB. A similar mechanism has been proposed in the thalamus, where reduction in the $GABA_AR$ mediated inhibition intensifies thalamocortical oscillatory activity (Huntsman et al., 1999). Interestingly, studies *in vivo* have shown that cortically projecting BF GABAergic neurons increase γ band oscillations by modulating local fast spiking (FS) inhibitory neurons (Kim et al., 2015a). Thus, the EPL-I neurons in the MOB could have a similar function as they also exhibited fast inhibition upon MCPO GABAergic activation. Future experiments should evaluate the contribution of FS neurons to γ oscillations in the MOB and their regulation by BF inhibition *in vivo*. Nevertheless, these changes in synchrony at the network level can also be explained by decorrelation of activity

in the output neurons, as BF-LRGN activation reduced spike precision on MCs in response to a simulated sensory input. It is noteworthy that GCs have been proposed to participate in the generation of highly precise firing in MCs (Schoppa, 2006), which is thought to underlie temporal encoding in the OB (Kepecs et al., 2006; Shusterman et al., 2011).

Activation of BF GABAergic inhibition in the glomerular or the GCL circuits greatly reduced the extent of inhibition in MCs. Interestingly, the density of innervation by MCPO GABAergic axons was highest in the GCL and therefore, BF inhibition is well poised to influence the role of GCs in odor processing. This would be in agreement with recent findings that highlight the importance of GABAergic inhibition of GCs, including that arising in the MCPO, in odor discrimination (Abraham et al., 2010; Nunez-Parra et al., 2013; Gschwend et al., 2015). On the other hand, in the glomerular layer, the decay of the IPSC elicited by MCPO axons activation in PGCs is significantly faster than for GCs. PGCs are reciprocally connected with M/TCs, from which they receive a strong excitation (Murphy et al., 2005). Consistent with our findings, a recent report described robust IPSCs in a subpopulation of PGCs elicited by activation of BF GABAergic neurons (Sanz Diez et al., 2019). This dendrodendritic interaction is thought to gate the glomerular output by regulating the activity of M/TCs (Wachowiak and Shipley, 2006; Gire and Schoppa, 2009; Shao et al., 2012), suggesting that phasic activation of BF-LRGNs can rapidly modulate the glomerular circuits, strongly impacting the strength of the incoming sensory input. Together these results suggest that the BF GABAergic input to the OB is well suited to rapidly modulate the extent of local inhibition in the glomerulus and the lateral dendrites of MCs.

Our results underscore the view that GCs integrate inhibition from two sources: top-down inhibition from MCPO afferents and inhibition from local interneurons (Pressler and Strowbridge, 2006; Eyre et al., 2008; Burton and Urban, 2015), however these sources of inhibition may play different functions on GCs. Phasic activation of MCPO GABAergic inputs elicited a fast synchronized release of GABA, suggesting a tight coupling between presynaptic action potentials and the release events (Kaeser and Regehr, 2014). However, the IPSC elicited by MCPO inputs in GCs had a slower time course (~40 ms) compared to the decay of the IPSC elicited by local inhibitory inputs (~6 ms) (Eyre et al., 2012), suggesting that these sources of inhibition may have a different function in the temporal domain. In the hippocampus IPSCs with fast decay kinetics are thought to facilitate γ oscillations, while IPSCs with slow decays likely control postsynaptic excitability (Bartos et al., 2002). Thus, it is possible that the slower decay of top-down inhibition has a stronger influence in the excitability of GCs, while the local inhibitory inputs may facilitate γ oscillations. Furthermore, the fast rise time of the min-IPSC suggested a predominant perisomatic targeting of the MCPO GABAergic input to GCs. Thus, BF inhibition could have a strong influence on the excitatory inputs that also target the proximal region of the GCs (Balu et al., 2007), which produces an overall inhibition of the OB output (Boyd et al., 2012, 2015; Markopoulos et al., 2012; Rothermel and Wachowiak, 2014; Otazu et al., 2015), further experiments are needed to determine the temporal window in which this regulation can occur.

Interestingly, in *in vivo* recordings from OB projecting MCPO neurons, these cells can be directly excited by activation of the piriform and entorhinal cortices (Paolini and McKenzie, 1997), suggesting modulation of MCPO LRGN activity by incoming odor-

elicited activity from olfactory areas. Since GCs are targeted by the MCPO GABAergic axons, these projections could participate in an OB-BF feedback loop that can rapidly modulate the temporal code in the OB. The highly branched BF-LRGN innervation across the OB cellular layers in addition to a relatively small number of OB projecting neurons in the MCPO (~680 GABAergic neurons) (Gracia-Llanes et al., 2010), suggests that GABAergic axons could influence a large number of interneurons in the OB. Thus, we hypothesize that top-down inhibition provides a rapid disinhibitory feedback to ongoing odor-induced activity in the OB, influencing the temporal and spatial dynamics of odor coding in the OB, including gain control and tuning specificity of the output neurons.

Chapter 3

Basal forebrain GABAergic projections to the olfactory bulb are rapidly recruited by odor encounters in a stimulus specific manner

Acknowledgments

We thank Dr. Priyanka Gupta, Dr. Honggoo Chae, Dr. Ruilong Hu, Mr. Devon Cowen and Mr. Martin B. Davis for technical assistance and members of the Araneda and Albeanu laboratories for helpful discussions. This research was supported by the National Institute on Aging of the National Institutes of Health, grant AG-049937A to Dr. Ricardo C. Araneda and National Institute on Deafness and Other Communication Disorders of the National Institutes of Health, grant 5R01DC014487-05 to Dr. Dinu F. Albeanu.

Summary

The output of the olfactory bulb (OB) is tightly regulated by top-down signals from several brain regions. Among these, a heterogeneous collection of GABAergic neurons in the basal forebrain (BF) broadly integrates cortical and subcortical inputs and send neuromodulatory signals to the OB. To date, however, how these GABAergic projections participate in the formation of olfactory representations remains unknown. Here, we used slice electrophysiology and multiphoton calcium imaging in awake male and female mice to investigate how the activity of the GABAergic neurons is recruited by olfactory stimulation. We demonstrate that OB projecting BF GABAergic neurons receive monosynaptic glutamatergic inputs from the piriform cortex, supporting the existence of a fast BF GABAergic feedback projection to the OB driven by odor stimulation. By imaging calcium signals from GABAergic axons in the OB, we found that synaptic boutons were spontaneously active across all bulb layers in awake mice. Importantly, odor presentation resulted in sparse responses in boutons across different OB layers in an odorant and concentration-specific manner. Across multiple odorants, boutons responded by either enhancement or suppression of the baseline signal, while mixed-type responses were rarely observed. The response dynamics of the BF GABAergic boutons, characterized by a fast onset, occurred in a similar time scale to those exhibited by glutamatergic feedback projections that originate in the piriform cortex, further supporting the existence of a fast GABAergic feedback loop from the BF. Since both glutamatergic and GABAergic feedback projections target the local GABAergic network in the bulb, our results indicate

that the BF feedback signals rapidly change the excitation-inhibition balance of the bulb output neurons.

Introduction

Sensory perception emerges from the interplay between stimulus-driven feedforward cortical activation and feedback signals that sculpt the activity of early processing circuits. Despite detailed knowledge of the role of bottom-up inputs in sensory representation across different modalities, we lack basic insight into how descending feedback signals restructure the incoming sensory input. In olfaction, odor information is first represented in the olfactory bulb (OB) by ensembles of output neurons, the mitral/tufted cells (M/TCs), which receive direct inputs from the sensory neurons (Shepherd, 2004). Like in other sensory circuits (Isaacson and Scanziani, 2011; Pfeffer et al., 2013), the activity of M/TCs is tightly regulated by local GABAergic networks, whose activity is influenced by extensive top-down signals (Matsutani and Yamamoto, 2008; Nagayama et al., 2014). Among these top-down signals, rich glutamatergic projections from the piriform cortex (PC) and anterior olfactory nucleus (AON) primarily innervate local GABAergic neurons of the bulb, the granule cells (GCs), and periglomerular cells (PGCs) (Shipley and Adamek, 1984; Shepherd, 2004; Matsutani, 2010; Rothermel and Wachowiak, 2014). This excitatory feedback drives strong feedforward inhibition onto M/TCs and has been proposed to enable odor pattern-separation by decorrelating and sparsening the activity of M/TCs (Boyd et al., 2012, 2015; Markopoulos et al., 2012; Otazu et al., 2015).

The bulb also receives descending GABAergic projections from the basal forebrain (BF), a brain region involved in state-dependent regulation of sensory circuits (Yang et al., 2014b; Hangya et al., 2015; Zant et al., 2016). The BF contains several types of projection neurons, including GABAergic and cholinergic neurons, which are rapidly recruited during reward-seeking behaviors (Hangya et al., 2015; Nunez-Parra et al., 2020; Sturgill et al., 2020; Hanson et al., 2021). Akin to the cortical excitatory feedback, BF long-range GABAergic neurons originating in the magnocellular preoptic area (MCPO) act mostly on the inhibitory neurons of the OB and, therefore can modulate spatial and temporal dynamics of the M/TCs output by controlling their inhibition by GCs and PGCs (Gracia-Llanes et al., 2010; Nunez-Parra et al., 2013; Sanz Diez et al., 2019; Böhm et al., 2020; Hanson et al., 2020; Villar et al., 2021a).

The BF is not a direct target of OB output neurons but instead integrates corticofugal signals (Cullinan and Záborszky, 1991; Zaborszky et al., 1997), as well as neuromodulatory inputs (Gaykema and Zaborszky, 1997; Zaborszky et al., 1999, 2012), and in turn, conveys broad projections to cortical and subcortical structures. Previous studies indicated that the PC can activate neurons in the BF (Paolini and McKenzie, 1997; Zaborszky et al., 1997), suggesting that upon odor stimulation, the activation of the BF may provide olfactory areas with fast and state-dependent top-down inputs for regulating early signal processing. Consistent with this framework, lesions or chemogenetic silencing of the MCPO in the BF, a main source of OB projecting GABAergic cells, significantly impairs odor discrimination (Paolini and McKenzie, 1996; Nunez-Parra et al., 2013). However, how these GABAergic projections to the bulb are recruited by odor stimuli and their functional role in regulating olfactory representations remain unknown. Here, we

provide evidence that neurons in the PC produce direct activation of OB projecting GABAergic cells in the MCPO. Furthermore, using multiphoton imaging of GCaMP6 signals in awake mice, we provide evidence that the responses of the GABAergic feedback to the OB are rather specific to odor identity and concentration.

Methods

Animals. All experiments were conducted following the US National Institute of Health guidelines and approved by the Cold Spring Harbor Laboratory Institutional Animal Care and Use Committee (IACUC) and the University of Maryland, College Park IACUC. *In vivo* imaging experiments and slice electrophysiological recordings were performed on adult C57BL/6 (JAX, stock #664) and *Vgat-IRES-Cre* (JAX, stock #028862) female and male mice (1- to 12-month-old), obtained from breeding pairs housed in our animal facility.

Stereotaxic injections. Animals were allowed to acclimate to the procedure room for at least 1 h before surgery. Anesthesia was induced with 2% isoflurane in oxygen at a rate of 1 L/min and adjusted over the course of the procedure from 0.5 to 1% to maintain a breathing rate of approximately 60 breaths per minute. While the mouse was mounted in the stereotaxic frame (Kopf, catalog #940), the depth of the anesthetized state was frequently tested using pedal reflexes and by monitoring the breathing rate and whisking. Body temperature was maintained using a feedback-controlled heating pad (FST TR-200, Fine Science Tools). Meloxicam (subcutaneous, 2 mg/Kg) was used as an anti-inflammatory and Betadine as an antiseptic. During the surgery, the eyes were lubricated

using a petrolatum ophthalmic ointment (Paralube). The virus was delivered with a glass pipette held by a needle holder and attached to the arm of the stereotaxic apparatus. Surgical tools were sterilized in an autoclave before use and decontaminated by dry heat between animals (Germinator 500, EMS). To express GCaMP6s in MCPO GABAergic neurons, *Vgat-Cre* mice received a stereotaxic injection of the AAV5-CAG-Flex-GCaMP6s adenovirus (160 nL, Catalog #100842, Addgene) using the following stereotaxic coordinates (in mm): D/V –5.4, M/L ± 1.63, A/P +0.14. For anterograde expression of GCaMP6s in PC neurons projecting to the OB, C57BL/6 mice were injected with the AAV1-Syn-GCaMP6s adenovirus (160 nL, Catalog #100843, Addgene), using the following stereotaxic coordinates (in mm): D/V –3.5, M/L ± 2.8 and A/P 1.6. After viral injection, mice were left to recover for at least three weeks before chronical window implantation. For optogenetic stimulation in axons of PC neurons projecting to the MCPO the AAV5-CAG-ChR2-tdTomato adenovirus (80 nL, Addgene) was injected into the PC of *Vgat-Cre* mice. To label OB projecting neurons in the MCPO, the same mice received an injection of the retrograde AAVrg-hSyn-DIO-eGFP virus (50 nL, Catalog #50457, Addgene) into the OB using the following stereotaxic coordinates (in mm): D/V –0.4, M/L ± 1.8, A/P 6.0.

Brain slices. Coronal slices containing MCPO (250 µm) were prepared using vibratome sectioning (VT1000S, Leica). Brain slices were kept in oxygenated ice-cold modified artificial cerebrospinal fluid (ACSF) containing low Ca^{2+} (0.5 mM) and high Mg^{2+} (3 mM). Sections were left to recover for at least 30 min at 35°C before electrophysiological recordings. After recovery, slices were kept at room temperature for

up to 6 h. The normal ACSF had the following composition (in mM): 125 NaCl, 26 $NaHCO_3$, 1.25 NaH_2PO_4, 2.5 KCl, 2 $CaCl_2$, 1 $MgCl_2$, 1 myo-inositol, 0.4 ascorbic acid, 2 Na-pyruvate, and 15 glucose. The ACSF solution was continuously oxygenated (95% O_2, 5% CO_2) to give a pH of 7.4.

Whole cell recordings. Electrophysiological recordings were conducted as previously described (Villar et al., 2021a). Briefly, whole-cell recordings were performed using a dual EPC10 amplifier (HEKA, Harvard Bioscience) at room temperature (~21°C). Glass pipettes were filled with an internal solution of the following composition (in mM): 130 Cs-gluconate, 4 KCl, 10 HEPES-K, 10 Na phosphocreatine, 2 Na^+-ATP, 4 Mg^{2+}-ATP, and 0.3 GTP. The final pH of the internal solution was adjusted to 7.3 with CsOH (osmolarity ~290 mOsm). Optogenetic stimulation was achieved using a LED lamp (COP1-A, Thorlabs) which produced brief pulses (1-3 ms) of collimated blue light (473 nm, ~1 mW/mm^2) delivered through the objective. Recordings were analyzed in MATLAB (MathWorks) and Igor Pro (WaveMetrics).

Chronic window implant. Mice were anesthetized with a single intraperitoneal injection of a ketamine (100 mg/Kg) and xylazine (10 mg/Kg) cocktail. Subcutaneous meloxicam (2 mg/Kg) was used as an anti-inflammatory. Depth of anesthesia was frequently monitored as described above. Anesthetized mice were loosely held on stereotaxic apparatus while the dorsal surface of the skull was exposed. The skull was cleaned with a blade, and a custom-built diamond-shaped titanium headbar was cemented (C&B Metabond, Parkell) on the back and front of the skull. A 3 mm craniotomy was made

on the skull overlying the olfactory bulbs by carefully thinning the bone with a dental drill (Foredom, Bethel). This procedure was carefully done to avoid damaging the meninges and superficial blood vessels. A thin coverslip (CS-3R, Warner instruments) was placed on top of the bulbs, and the edges were sealed with a small amount of Vetbond (3M) followed by cyanoacrylate glue (Super glue). The dorsal skull surface was further reinforced with dental acrylic (Lang Dental), which was shaped like a well to contain a small amount of water for the immersion objective during the imaging sessions. Mice were left to recover for at least one week before imaging.

Imaging session procedure. Naïve mice were habituated to the headbar holder and rig for at least 30 min before imaging. A typical odor presentation routine consisted of 10 s of clean air, followed by 4 s of odor stimulation and 16 s of air. The interval between trials was at least 30 s and each stimulus was presented 5 times. Mice were imaged on consecutive days, and no more than one imaging session was performed per day. After each session, mice were returned to their home cage and kept over a heating pad before returning to the main colony.

Odor stimulation. Odors were randomly delivered using a custom-built odor machine as previously described (Soucy et al., 2009). Pure odors (Sigma, International Flavors & Fragrances) were diluted in mineral oil and stored in glass blood collection tubes (BD Vacutainer). Clean air entered each odor tube at a rate of ~1 L/min. Air flow through each tube was directed by independent solenoid valves controlled by custom-written software (LabVIEW, National Instruments). Odors were carried from the odor machine to

the test subject by a Teflon coated tubing and delivered through a 3D-printed nose piece. A photoionization device (PID, Aurora Scientific) was used to determine the time course and reliability of the odor delivery.

Multiphoton imaging. Imaging was performed with a custom-built multiphoton microscope coupled to a Ti:Sapphire femtosecond pulsed laser (Chameleon Ultra II, Coherent). A 915 nm tuned laser beam was projected onto a resonant-galvo-based scanning head (12 KHz, High Stability 8315K-CRS-12 Set, Cambridge Technologies). The scanning system steered the laser through scan and tube lenses to backfill the aperture of a 20X, 1.0 NA objective. Signals were acquired using a GaAsP PMT (H10770PB-40, Hamamatsu), amplified, filtered (DHPCA-100, Femto), and digitized at 200 MHz (NI PXIe-7966R FPGA Module, NI5772 Digitizer Adapter Module). The laser power was adjusted to minimize bleaching and typically was set below 50 mW, measured under the objective. Image acquisition was controlled by custom-written software (LabVIEW, National Instruments including Iris, courtesy of Georg B. Keller lab, FMI, Basel).

Histology. Post hoc, the brains of all mice were harvested to verify the accuracy of the targeted injection site. Mice were transcardially perfused with cold 4% paraformaldehyde (PFA) diluted in 0.1 M phosphate buffer saline (PBS), pH 7.4. Brains were then post fixed overnight at 4°C in PFA and the tissue was sliced on a vibratome. Nuclei were stained with DAPI dihydrochloride (300 nM, Catalog #D1306, Invitrogen) and mounted in a solution of Mowiol-DABCO. Mowiol mounting media was made in batches of 25 mL containing 9.6% w/v mowiol (Catalog #475904, Millipore), glycerol

24% w/v, 0.2 M Tris (pH 6.8), 2.5% w/v DABCO (antifade reagent, Catalog #D2522, Sigma) and Milli-Q water. To amplify the GCaMP6s signal in fixed slices, we used immunohistochemistry against GFP. Free floating brain sections (50 μm) were first blocked with donkey serum (10%, Catalog #S30-M, Millipore) in PBS supplemented with Triton X-100 (PBS-T, 0.1% v/v, Catalog #T8787, Millipore) for 1 h at room temperature (RT) to block unspecific binding sites. Sections were then incubated overnight at RT with a rabbit anti-GFP primary antibody (1:500, Catalog #598, MBL) and 2.5% donkey serum in PBS-T. The primary antibody was washed with PBS-T for at least 30 min before incubation with a donkey anti-rabbit antibody coupled to Alexa fluor-594 for 2 h, at RT (1:500, Catalog #A-21207, Invitrogen). Slices were stained with DAPI, dried, and mounted using Mowiol-DABCO. Images were acquired using a confocal microscope (Leica SP5X, Leica Microsystems).

Data analysis

Image registration and z-plane motion detection. x-y translations were corrected using the Fourier transform based registration method (Kuglin and Hines, 1975). A subset of 20 random frames from each trial was used to obtain an average image used as reference during the registration. Displacements of each frame with respect to the reference image were estimated by computing cross-correlation peaks using the FFT function in custom-written MATLAB software. Fast z-plane motion was detected by comparing the shape of an ROI in a particular frame to that in the reference image (Otazu et al., 2015). If the ROI in a given frame has identical shape to the reference ROI, the cosine (cos_{frame}) between

vectors of length equal to the number of pixels within the reference ROI (r_{mean}) and an individual frame (r_{frame}) has a value of 1. If the reference and frame ROIs have different shape cos_{frame} approaches to zero,

$$cos_{frame} = \frac{r_{mean} \cdot r_{frame}}{\sqrt{(r_{mean} \cdot r_{mean})(r_{frame} \cdot r_{frame})}}$$

Thus, for each ROI, we computed a cos_{frame} time series to monitor the stability of each ROI in a given field of view (FOV). Z-plane motion produced a synchronized drop in the cos_{frame} across ROIs in the FOV. To quantify this drop, we calculated the population stability for a given frame defined as the median of cos_{frame} across ROIs in the FOV. Population stability for each frame was converted to z-score by subtracting the mean population stability during the time preceding the odor (pure air application), where z-motion was less frequent, and dividing by the standard deviation of the population stability during the air period. A drop in 2.5 z-scores was classified as z-motion and the entire frame was discarded. ROIs (~1 to 2 μm) were manually selected in MATLAB based on mean registered images.

Detection of odor responses. We obtained a bootstrap estimate of the spontaneous fluorescence during the air period. For each bouton, the mean dF/F was calculated during the air period (baseline) with a window of time equivalent to the duration of odor presentation (4 s) across all trials. The mean dF/F during the odor presentation window was compared with the baseline fluorescence. An odor response in a single trial was considered

a “significant enhancement” if it exceeded the 99.9th percentile, and a “significant suppression” if it corresponded to less than 0.1th percentile of the bootstrap distribution. Boutons were considered to have a significant odor response when they responded significantly to at least 3 of the 5 presentations of a given odor.

Clustering analysis. dF/F traces from responding boutons were used to cluster odor responses using the k-means clustering function in MATLAB. To determine the number of clusters, we calculated the average distance from each point to every centroid (*d*-value) while varying the number of clusters from 1 to 10. The *d*-value was plotted against the number of clusters used for clustering, and the cutoff for the number of clusters was obtained when the *d*-value reached a plateau (Otazu et al., 2015).

Pairwise similarity. For bouton similarity, the odor response spectrum (ORS) for a given responding bouton was defined as a vector of length equal to the total number of odors used and containing the mean response value (dF/F) across trials for each odor. A value of 0 was assigned to non-significant responses. Similarly, we defined the bouton response spectrum (BRS) to an odor in a given FOV as a vector of length equal to the total number of boutons in each FOV and containing the mean response value (dF/F) across trials for each odor. Pairwise bouton similarity was defined as the cosine of the angle between two ORS vectors, ORS_i and ORS_j, and defined as follows:

$$Bouton\ similarity = \frac{ORS_i \cdot ORS_j}{\sqrt{(ORS_i \cdot ORS_i)(ORS_j \cdot ORS_j)}}$$

Likewise, pairwise odor similarity between two BRS vectors, BRS_i and BRS_j, was computed as follows:

$$Odor\ similarity = \frac{BRS_i \cdot BRS_j}{\sqrt{(BRS_i \cdot BRS_i)(BRS_j \cdot BRS_j)}}$$

Lifetime sparseness (LS). Sparseness quantifies the extent to which a given bouton is modulated by different stimuli, and it was computed as follows:

$$LS_i = 1 - \frac{(\sum_{j=1}^{m} \frac{r_j}{m})^2}{\sum_{j=1}^{m} \frac{r_j{}^2}{m}}$$

where i = bouton index, m = number of odors and r_j = mean bouton response to odor j. In this metric a value of 0 represents a dense code, while 1 represents a sparse code (Vinje and Gallant, 2000; Willmore et al., 2011).

Odor response onset. The dF/F traces showing significantly enhanced or suppressed odor responses were used to estimate the response onset time. This was defined as the time by which 5% of the response maximal amplitude was achieved. Similarly, the response rise time was computed as a time window from 10 to 90% of the maximal response amplitude.

Results

OB projecting GABAergic neurons are driven by direct inputs from piriform cortex

To date, how the activity of MCPO GABAergic neurons targeting the OB is recruited during olfactory guided behaviors is unknown. Therefore, to determine whether these neurons receive excitatory inputs from the olfactory cortex, we injected the anterograde tracer AAV-CAG-tdTomato in the PC of wild-type mice (**Figure 1A**, left). PC injections rendered abundant innervation of the MCPO that was also characterized by ample presence of synaptic boutons (**Figure 1A**). Next, to determine whether OB projecting GABAergic cells in the MCPO receive direct excitatory inputs from the PC, we retrogradely labeled GABAergic neurons in the MCPO from the OB using the broad GABAergic marker Vgat to drive Cre-dependent transduction of a retrograde adenovirus (AAVrg-DIO-GFP, see Methods). Recordings were performed in MCPO GFP^+ cells while optogenetically stimulating PC axons expressing the light-sensitive channel channelrhodopsin (ChR2) (**Figure 1B**). Light stimulation of PC axons in the vicinity of OB projecting MCPO GABAergic neurons consistently evoked short latency EPSCs (5.2 ± 0.9 ms, n= 15 EPSCs, 2 cells), suggesting monosynaptic excitatory connections (**Figure 1C**). These responses were blocked by perfusing the AMPA receptor blocker CNQX (**Figure 1C**) (control, –184 ± 148 pA vs. CNQX, –13 ± 10 pA, n= 2). These results strongly suggest that OB projecting MCPO GABAergic cells participate in a fast feedback loop that can be driven by a descending input from the PC.

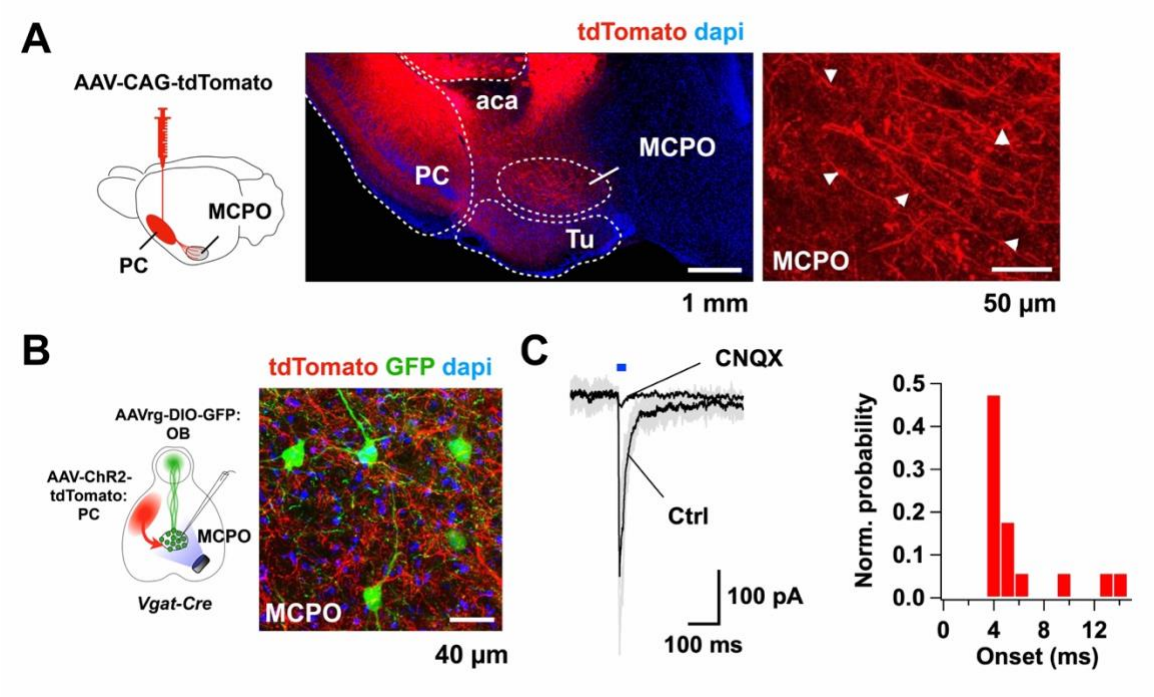

Fig. 1: *OB projecting MCPO GABAergic neurons are recruited by direct PC excitatory inputs*

(A) Left diagram, the anterograde tracer AAV-CAG-tdTomato was injected into the PC of wildtype mice to trace projections to the BF. Middle, confocal image of a coronal slice containing the MCPO, shown at a higher magnification on the right; abundant labeled axons are present in the MCPO. **(B)** Left diagram, OB projecting MCPO GABAergic cells were labeled with a retrograde AAVrg-DIO-GFP virus injected into the OB of *Vgat-Cre* mice. In addition, the anterograde AAV-ChR2-tdTomato virus was injected into the PC to label MCPO projecting axons. Right, confocal image of the MCPO of a *Vgat-Cre* mouse showing retrogradely labeled GFP GABAergic neurons (green) surrounded by abundant PC axons (red). Nuclear dapi staining is shown in blue. Targeted whole cell recordings were performed in coronal MCPO slices from neurons expressing GFP, and PC axons expressing ChR2 were optogenetically stimulated. **(C)** Right, a brief light stimulation of PC axons evoked a fast eEPSCs in GFP expressing MCPO neurons. The light-evoked excitation was completely blocked by perfusing the glutamate receptor blocker CNQX (10 µM) (n= 2 cells). Left, histogram of the onset time for the cortically evoked EPSCs recorded from OB projecting GABAergic neurons.

Monitoring the activity of the OB GABAergic feedback in vivo

Direct activation of GABAergic neurons by inputs from the PC, predicts that these neurons should be recruited by odor stimulation and provide a fast inhibitory input to the bulb. To examine this possibility, we recorded the activity of MCPO GABAergic axons in the OB using multiphoton microscopy in naïve head-fixed mice. We drove Cre-dependent expression of the calcium indicator GCaMP6s (Chen et al., 2013) in the MCPO of *Vgat-Cre* mice using an adenovirus (AAV5-Flex-GCaMP6s, see Methods) (**Figure 2A**, diagram). Targeted viral injections reliably transduced GABAergic neurons in the BF, including the MCPO and substantia innominata (SI) (Villar et al., 2021a) (**Figure 2A**, **Figure 2-1A**), and consistent with their GABAergic nature, the expression of GCaMP6s in the MCPO co-localized with the GABAergic proteins Gad65/67 (**Figure 2-1B**) (Nunez-Parra et al., 2013). In confocal images of immuno-amplified GCaMP6s fluorescence, we found that the mean raw signal intensity of axonal labeling is highest across the glomerular and granule cell layers (GL and GCL, respectively), which contain the most prominent inhibitory neurons of the OB (**Figure 2-1C**). These axons appeared homogeneously distributed across the dorso (D)-ventral (V) and medial (M)-lateral (L) axes of the bulb (intensity in arbitrary units): D-GL 16.1 ± 1.5 vs. V-GL 22.0 ± 1.7, p= 0.06; D-GCL 26.6 ± 4.3 vs. V-GCL 28.0 ± 8.5, p= 0.9; M-GL 20.7 ± 2.8 vs. L-GL 19.0 ± 4.2, p= 0.74; M-GCL 31.8 ± 2.9 vs. L-GCL 27.0 ± 4.1, p= 0.37) (**Figure 2A**, **Figure 2-1C**). However, MCPO axons were denser in the GCL compared to the GL, consistent with previous reports (Gracia-Llanes et al., 2010; Nunez-Parra et al., 2013; Hanson et al., 2020; Villar et al., 2021a) (**Figure 2-1C**). In awake mice, GCaMP6s fluorescence observed under the two-

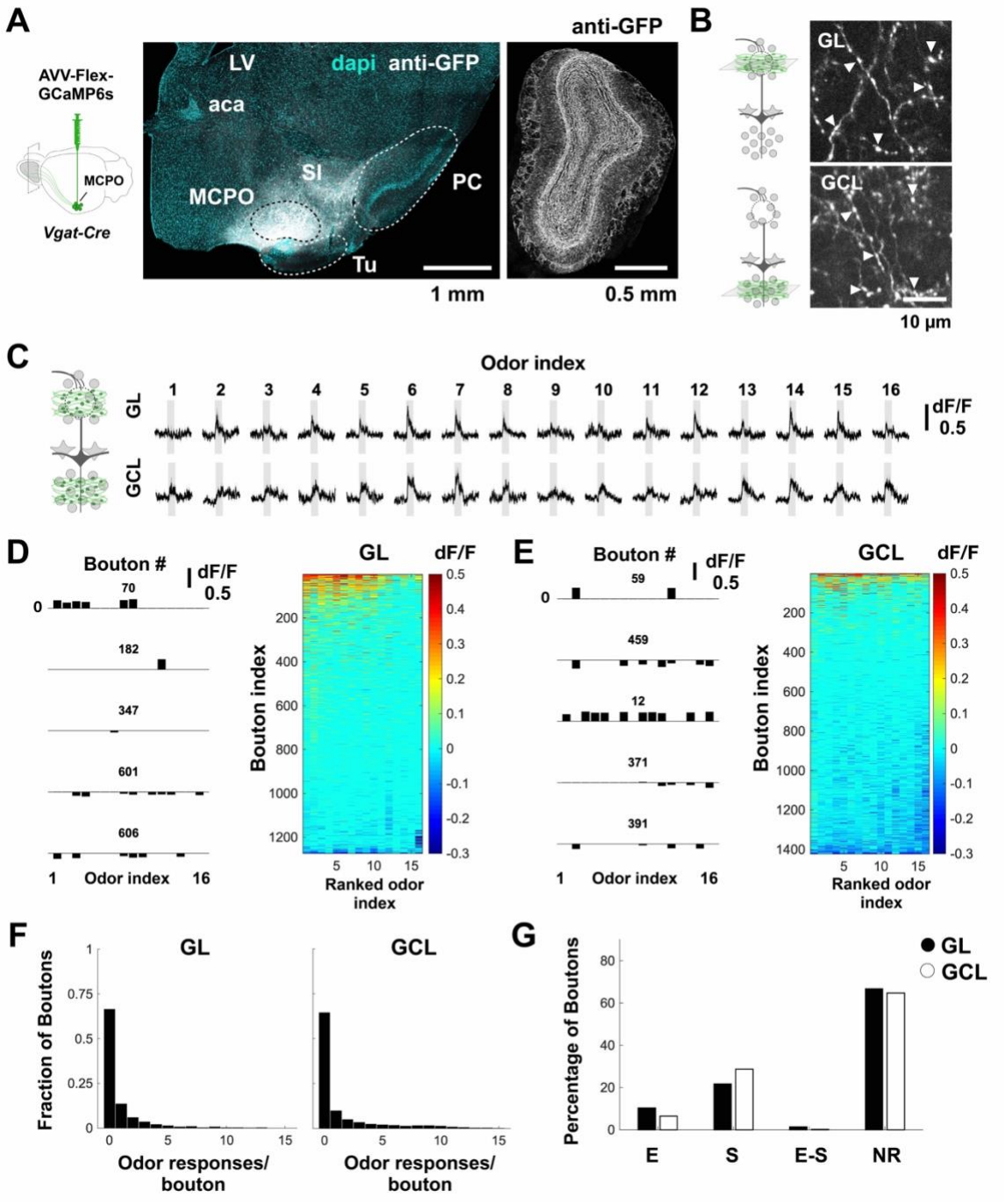
A
AVV-Flex-
GCaMP6s
MCPO
Vgat-Cre
LV
aca
dapi anti-GFP
SI
MCPO
PC
Tu
1 mm
anti-GFP
0.5 mm
B
GL
GCL
10 µm
C
Odor index
GL
GCL
1 2 3 4 5 6 7 8 9 10 11 12 13 14 15 16
dF/F
0.5
D
Bouton #
dF/F
0.5
70
182
347
601
606
1
Odor index
16
GL
dF/F
Bouton index
Ranked odor
index
E
Bouton #
dF/F
0.5
59
459
12
371
391
1
Odor index
16
GCL
dF/F
Bouton index
Ranked odor
index
F
GL
GCL
Fraction of Boutons
Odor responses/
bouton
Odor responses/
bouton
G
GL
GCL
Percentage of Boutons
E
S
E-S
NR

Fig. 2: *GABAergic boutons show diverse activity dynamics in response to odors*

(A) Left, schematic of the experimental approach. *Vgat-Cre* mice were injected in the MCPO with the Cre-dependent virus AAV-Flex-GCaMP6s to express the calcium sensor in GABAergic neurons. Center, confocal image of a coronal brain section showing abundant GCaMP6s expression in GABAergic cells of the MCPO. Right, confocal image of a coronal section of the olfactory bulb (OB) showing the distribution of MCPO GABAergic axons axon expressing GCaMP6s. Intrinsic GCaMP6s fluorescence was enhanced by immunohistochemistry against GFP that also labels GCaMP6. LV, lateral ventricle; aca, anterior commissure; SI, substantia innominata; PC, piriform cortex, Tu, olfactory tubercle. **(B)** Left, diagram of the OB indicating the imaged field of view (FOV) in the GL (top) or GCL (bottom). GABAergic axons and boutons expressing GCaMP6s are shown in green. Right, *in vivo* multiphoton images of representative FOVs showing MCPO GABAergic axons expressing GCaMP6s in the glomerular layer (GL, top, ~50 µm deep) and granule cell layer (GCL, bottom, ~300 µm deep); in both layers, axons contain abundant synaptic boutons (white arrowheads). **(C)** Sample dF/F traces for a selected bouton in the GL (top) and in the GCL (bottom) showing responses to a set of 16 odors presented to an awake head-fixed mouse. **(D)** Left, examples of odor response spectra (ORS) for five GABAergic boutons in the GL. Bouton index is indicated on top. Black bars represent the mean magnitude of odor responses which is positive for enhanced and negative for suppressed responses. Right, heatmap of mean odor-evoked responses for bouton in the GL that responded significantly to at least one stimulus in our 16-odor set (20 FOVs, 5 mice). Responsive boutons are shown ranked by magnitude from the most to the least responsive. Red shades correspond to enhancement and darker blue to suppression **(E)** Sample ORSs and response heatmap for the GCL, as described in panel D (19 FOVs, 6 mice). **(F)** Histogram showing the number of odor-evoked responses per bouton in the GL (left) and GCL (right). **(G)** Percentage of boutons in the GL (black bars) and GCL (white bars) that responded exclusively with either enhancement (E) or suppression (S), exhibited both E and S (E-S), and non-responsive boutons (NR). The laminar distribution of the MCPO GABAergic axons across the OB layers is shown in **Figure 2-1** (Appendix B). Samples of additional GABAergic bouton responses and stacked odor-boutons pairs for enhanced and suppressed responses are shown in **Figure 2-2** (Appendix B). Odor responses in boutons of glutamatergic axons from PC feedback neurons in the OB are shown in **Figure 2-3** (Appendix B).

photon microscope, was prominent in the synaptic boutons of the axonal processes across both GL and GCL (**Figure 2B**, **Figure 2-1D**). *In vivo*, the density of GABAergic boutons across layers appeared slightly higher in deeper field of views (FOV); although, these differences were not statistically significant (GL 2.2 vs. GCL 2.4 boutons/100 μm^2, n= 19 GCL FOVs, 6mice; 20 GL FOVs, 5 mice; p= 0.46) (**Figure 2-1D**).

Odors evoke enhancement or suppression of baseline activity in GABAergic boutons

Early studies suggested that the BF receives cortical olfactory information (Paolini and McKenzie, 1997; Zaborszky et al., 1997), yet to date, the response dynamics of MCPO GABAergic neurons during olfactory stimulation remain unknown. Therefore, we exposed naïve head-fixed mice to odor stimulation with a diverse panel of odors while recording the activity of the boutons of GABAergic axons in the OB. A set of 16 odors (Table S1, Appendix B), known to activate the dorsal surface of the OB (Soucy et al., 2009), were randomly delivered while imaging GCaMP6s signals from boutons in the GL and GCL. To determine whether odors evoked significant responses, we compared the changes in fluorescence during odor presentation with the fluorescence of baseline activity (see Methods) (Otazu et al., 2015). In boutons exhibiting significant responses to at least one odor in the set, activity traces (dF/F) for all trials were averaged (for either enhancement or suppression, see below) (**Figure 2C**, **Figure 2-2A, B**), and the mean response amplitude during the odor presentation is shown as a vector, or heatmap, as a function of the odor identity (**Figure 2D, E**). Odor presentations triggered significant responses to at least one odor in ~33% of the imaged boutons in the GL (1273/3816, 20 FOVs, 5 mice) and in ~35%

of the boutons in the GCL (1422/4029, 19 FOVs, 6 mice) (**Figure 2F, G**). Thus, on average, a given bouton responded to 1.1 ± 0.04 odors in the GL and 1.6 ± 0.05 in the GCL, from the 16 odors in the set. On average, a given odor in the panel evoked significant responses in ~7% of the imaged boutons in the GL and 10% in the GCL, with low variance across the different odors in the set (σ^2 GL 5.8, GCL 6.2) (**Figure 2-2C**).

Interestingly, individual odors elicited both enhancement and suppression of baseline activity in different boutons, and boutons exhibiting mixed responses were rare (**Figure 2G**). From all responding boutons imaged in the GL, ~31% responded to odors exclusively with enhancement (393/1273 boutons), while ~65% did exclusively with suppression (827/1273 boutons). Similarly, in the GCL ~18% of the responding boutons showed only enhancement (259/1422 boutons), while ~81% showed only suppression (1157/1422 boutons). In contrast, only 4% of boutons in the GL and 0.4% in GCL exhibited both enhanced and suppressed responses, suggesting that MCPO GABAergic axons show a segregation in their response mode.

Previous studies demonstrated that responses to odors in the excitatory feedback from PC to the OB also exhibit distinct temporal dynamics (Boyd et al., 2015; Otazu et al., 2015). However, we found that odor responses of MCPO GABAergic boutons were denser than responses observed in the glutamatergic PC feedback axons imaged under the same conditions (**Figure 2-3A, B**). In contrast to GABAergic boutons, significant responses in glutamatergic boutons triggered by at least one odor in the set were fewer: ~12% boutons in the GL (348/2999, 16 FOVs, 3 mice) and in ~10% of the boutons in the GCL (396/3840, 19 FOVs, 3 mice) (**Figure 2-3C**). Nevertheless, consistent with previous findings (Boyd et al., 2015; Otazu et al., 2015), the segregation in response modes was also present in the

PC glutamatergic boutons (**Figure 2-3D**). Of the responding boutons, ~52% (181/348 boutons) responded to odors exclusively with enhancement, and ~46% did exclusively with suppression in the GL (161/348 boutons), while in the GCL ~34% (133/396 boutons) showed only enhancement, while ~66% showed only suppression (261/396 boutons). Furthermore, like the GABAergic boutons, those exhibiting both enhanced and suppressed responses were very rare (0.2% in the GL and 0.05% in GCL). Interestingly, on average, a given PC feedback bouton responded to 0.3 ± 0.02 odors in the GL and 0.2 ± 0.02 odors in the GCL. Thus, the number of odors a given glutamatergic bouton responded to was lower compared to the GABAergic boutons, suggesting a difference in the degree of specificity in odor responses with lower odor specificity in the GABAergic boutons.

Interestingly, the ratio of suppressed over enhanced responses in the GCL for the GABAergic boutons was larger than for glutamatergic boutons (4.5 vs. 1.9, respectively), and a similar trend was observed in the GL (2 vs. 0.9, respectively). These results indicate that overall suppressed responses are more prominent in the MCPO GABAergic boutons than in the PC feedback boutons, suggesting that locally the reduction in the activity of the GABAergic feedback, which targets GCs (Villar et al., 2021a), would likely increase inhibition of M/TCs, especially in deeper OB layers.

MCPO GABAergic boutons show sparse and odor specific responses in the bulb

To quantify the extent to which the activity of a given bouton was modulated by the different odors, we computed the lifetime sparseness (LS). The LS metric ranges from 0 to 1, where 0 indicates an equal response to all odors (dense response), and 1 means that

all responses are concentrated in a single stimulus (sparse response) (see Methods). The distribution of LS values for both suppressed and enhanced boutons was skewed towards sparse responses, although suppressed responses were significantly sparser across the superficial and deeper layers (LS in the GL; suppressed 0.90 ± 0.003, n= 866 boutons vs. enhanced 0.77 ± 0.01, n= 455, $p< 0.001$; LS in the GCL, suppressed 0.84 ± 0.004, n= 1150 boutons vs. enhanced 0.79 ± 0.01, n= 276 boutons, $p< 0.001$). While enhanced responses were similarly sparse across the GL and GCL ($p= 0.98$), suppressed responses were significantly sparser in the GL ($p< 0.001$) (**Figure 3A, B**). Overall, these results are consistent with a sparse odor activation and suggest that the MCPO GABAergic boutons are narrowly tuned to odors.

We next examined how similarly boutons responded to the different odors in the set. We constructed vectors representing the response profile to the set of odors for each responding bouton (**Figure 3C**). Pairwise bouton similarity was computed as the cosine of the angle between two bouton response vectors (see Methods). Thus, similar boutons exhibit pairwise similarity values close to 1 while boutons having orthogonal vectors approximate to 0. Consistent with the largely sparse activation observed, the overall pairwise similarity was low across responding boutons (**Figure 3D**). Nevertheless, the mean bouton similarity was lower for suppressed compared to enhanced responses across both layers (GL, suppressed 0.04 ± 0.32 SD, n= 866 boutons vs. enhanced 0.21 ± 0.28 SD, n= 455 boutons, $p< 0.001$; GCL, suppressed 0.09 ± 0.30 SD, n= 1150 boutons vs. enhanced 0.18 ± 0.26 SD, n= 276 boutons, $p< 0.001$). In addition, odor responses were significantly different across the GL and GCL for both enhanced ($p< 0.001$) and suppressed ($p< 0.001$)

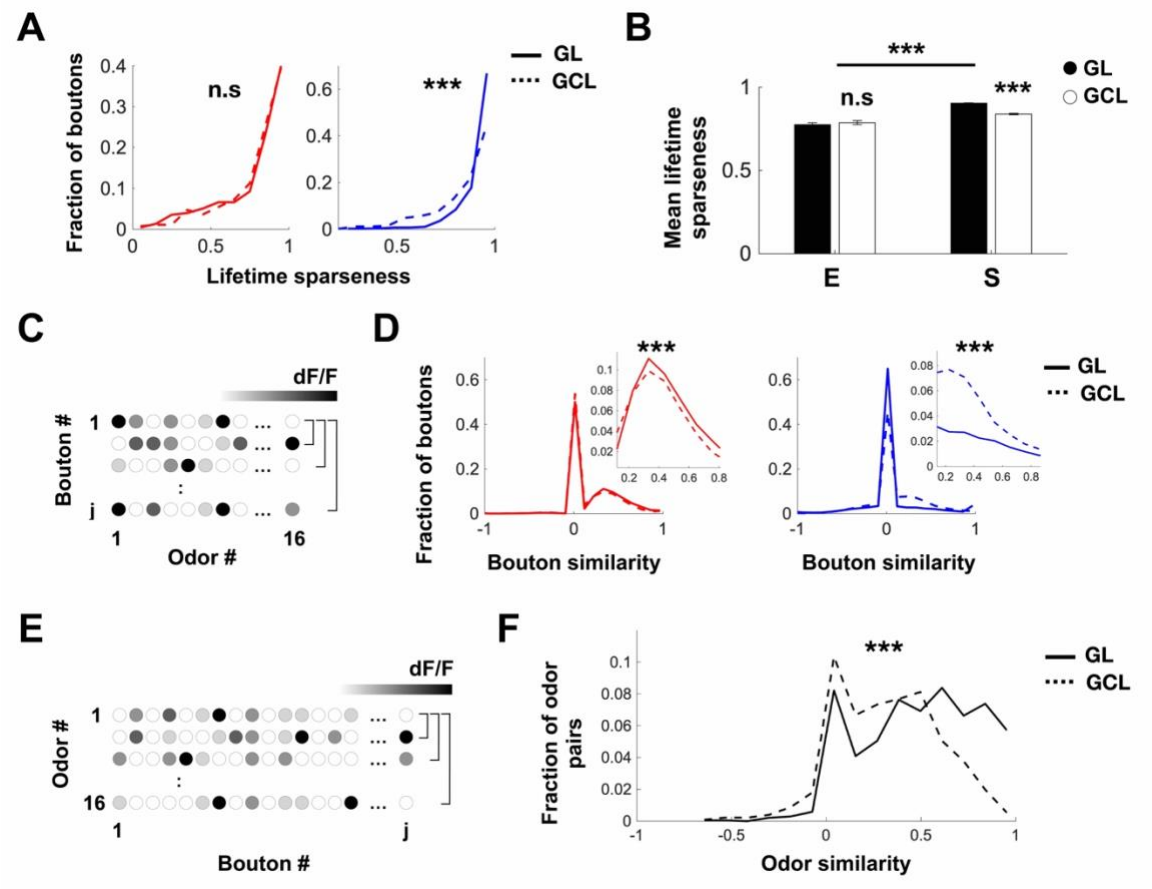

Fig. 3: *GABAergic boutons exhibit sparse and odor selective responses*

(A) Histogram of lifetime sparseness (LS) values for enhanced (red) and suppressed (blue) odor responses from boutons imaged in the GL (continuous line) and GCL (dotted line). The distribution of LS for suppression responses are significantly different between the GL and GCL ($p<0001$, Wilcoxon rank sum test). **(B)** Bar graph showing the mean LS across response modes and layers. The mean LS for enhanced responses was not significantly different across GL and GCL, while suppressed responses in the GL were significantly sparser ($p< 0.001$, Wilcoxon rank sum test). Overall, suppressed responses were sparser than enhanced responses ($p< 0.001$, Wilcoxon rank sum test). **(C)** Graphic representation of pairwise bouton similarity. Each circle represents an odor application, and the intensity of the shading corresponds to the response amplitude. The odor response spectrum (ORS, row) was defined as a vector of length equal to the number of odors, containing the mean odor responses for all odors presented. Similarity was defined as the cosine of the angle between the ORS of two boutons. **(D)** Histogram of bouton similarity values for enhanced (red) or suppressed (blue) responses in boutons imaged in the GL (continuous line) and GCL (dotted line). Bouton similarity equal to 0 indicates different responses between two given boutons, while a similarity equal to 1

indicates they exhibit the same response. A similarity value of -1 indicates opposite responses. The inset graphs show an expansion of the range for bouton similarity. Bouton similarity of enhanced responses is lower in the GL ($p < 0.001$, Wilcoxon rank sum test), while similarity is higher in the GCL for suppressed responses ($p < 0.001$, Wilcoxon rank sum test). **(E)** Graphic representation of pairwise odor similarity comparison. **(F)** Histogram of odor similarity values for GL (continuous line) and GCL (dotted line), as defined above. Odor similarity was significantly higher in the GL compared to GCL ($p < 0.001$, Wilcoxon rank sum test).

responses. These results further support differences in the odor response specificity of boutons in the superficial versus deeper layers of the bulb.

Lastly, we evaluated the pairwise odor similarity for stimuli within the panel, considering both enhanced and suppressed odor responses. We constructed vectors representing each odor in the 16-odor set and containing the mean response for all boutons in a given FOV (see Methods) (**Figure 3E**). Pairwise odor similarity was significantly lower in the GCL compared to the GL (GCL, 0.32 ± 0.27 SD vs. GL, 0.49 ± 0.31 SD, $p < 0.001$) (**Figure 3F**), suggesting that odor responses in the GL are more similar across stimuli compared to corresponding responses in the GCL. Functionally, these results indicate that deeper layers of the OB, which contain the GCs and that are critical in regulating the function of M/TCs, integrate highly specific top-down GABAergic signals that could rapidly modulate the output of the bulb in an odor-specific manner.

Odors evoke fast responses in the MCPO GABAergic boutons

To gain insight on the different odor-evoked kinetics, we clustered responsive odor-bouton pairs (**Figure 4A**) using the k-means method (see Methods) (Otazu et al., 2015; Villar et al., 2021b). Overall, we found that for both enhanced and suppressed responses,

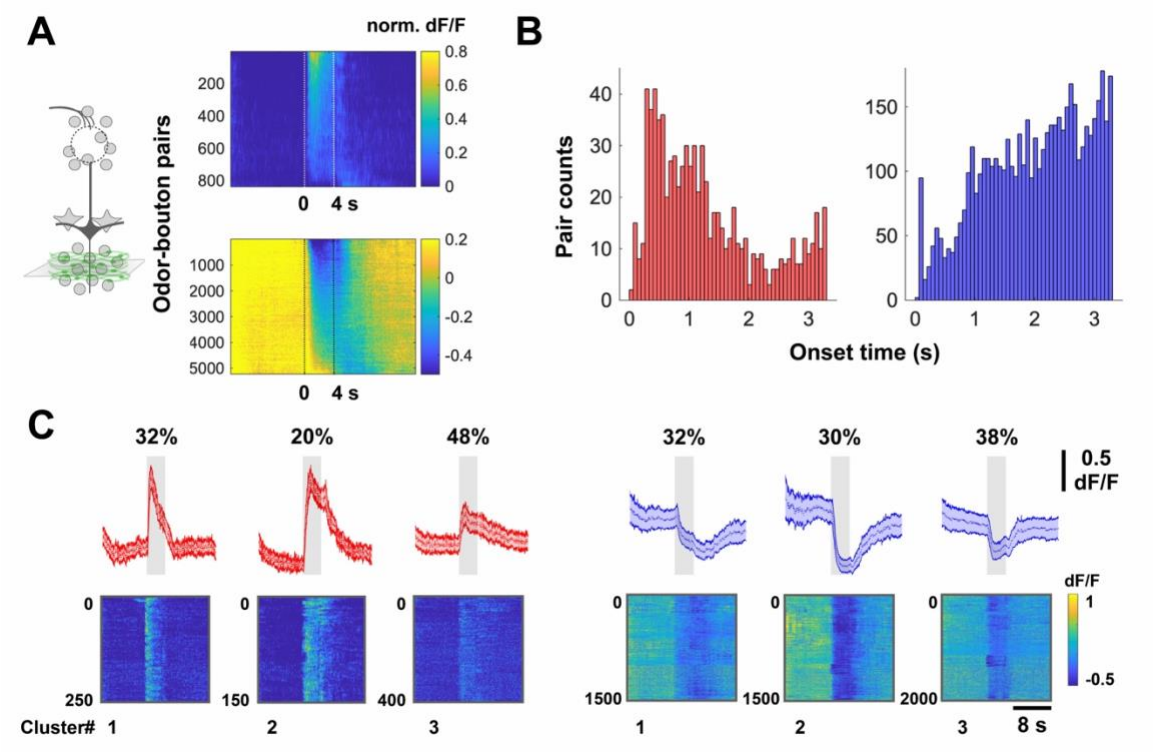

Fig. 4: *GABAergic boutons in the GCL respond to odors with transient enhancements or suppressions*

(A) Left, diagram of the OB showing a FOV in the GCL. Right, heatmaps of the normalized odor responses for all enhanced (top) and suppressed (bottom) odor-bouton pairs in the GCL. Suppressions were observed in boutons with higher baseline. **(B)** Histogram distribution of onset times for enhanced (red) and suppressed odor-evoked responses across responding boutons. The onset of enhanced responses is faster. **(C)** K-means clustering of enhanced (left) and suppressed (right) odor evoked responses obtained in the GCL using the 16-odors panel. Only dF/F traces from odor bouton pairs that had significant responses were used for this analysis. Top panels, mean odor responses obtained from all odor-bouton pairs pertaining a given cluster. The percentage of odor-bouton pairs assigned to a particular cluster is indicated on top. Vertical gray bars indicate the time of odor presentation. Bottom panels, heatmaps of the activity of all odor-bouton pairs for a given cluster. Odor-evoked kinetics of the GABAergic boutons in the GL are shown in **Figure 4-1** (Appendix B).

bouton activity in the GCL closely followed the stimulus delivery (**Figure 4C**). Enhanced responses had a fast onset (cluster 1: 0.86 ± 0.05 s, cluster 2: 1.33 ± 0.06 s, cluster 3: 1.55 ± 0.05 s) and fast time to peak (cluster 1: 0.22 ± 0.01 s, cluster 2: 0.35 ± 0.04 s, cluster 3: 0.13 ± 0.01 s), which was followed by a steep decay for enhanced responses (52% of odor-bouton pairs, cluster 1 and 2). Instead, suppressed responses had slower onset times (cluster 1: 2.25 ± 0.02 s, cluster 2: 1.91 ± 0.02 s, cluster 3: 1.84 ± 0.02 s) and rise times comparable to those of enhanced responses (cluster 1: 0.15 ± 0.01 s, cluster 2: 0.39 ± 0.02 s, cluster 3: 0.22 ± 0.01 s) (**Figure 4B**). Similar odor-evoked kinetics were observed in the GL (**Figure 4-1A, B**).

It should be noted that the baseline calcium signal of boutons exhibiting suppressed responses was significantly higher compared to boutons responding with enhancements (enhanced, –0.02 ± 0.002 dF/F vs. suppressed, 0.24 ± 0.002 dF/F, $p < 0.001$). This could, in principle, facilitate the detection of suppressed responses in boutons with high baseline activity and bias the detection of enhanced responses to boutons with lower baseline activity. The higher baseline of calcium could be due to a higher resting firing rate in these neurons.

Response modes are maintained across odor concentrations

To investigate whether the activity of the MCPO GABAergic boutons was modulated by the intensity of the stimuli, we monitored boutons while presenting odors across three orders of magnitude concentration range (**Figure 5A**). We presented a subset of five odors from the 16-odor set (**Table S2**, Appendix B), at three dilutions (1:100, 1:1000 and 1:10,000; in mineral oil). Similar to the results obtained with the 16-odor set,

we found that a minority of boutons exhibited fast-onset responses to at least one odor, with enhancement or suppression across the GL and GCL. In the GL, the percentage of responding boutons remained relatively constant as the odor concentration increased (10^{-4}: 24%, 10^{-3}: 22% and 10^{-2}: 22%; 15 FOVs, 3 mice) (**Figure 5B**). However, the percentage of boutons responding with suppression, which was the most common response type across all concentrations, slightly decreased as odor concentration increased (10^{-4}: 23%, 10^{-3}: 21% and 10^{-2}: 18%) (**Figure 5D**). In contrast, enhanced responses slightly increased at higher odor concentrations (10^{-4}: 0.8%, 10^{-3}: 1% and 10^{-2}: 3%). Consistent with our findings above (**Figure 2**), the percentage of boutons showing both enhanced and suppressed responses was low and remained unchanged at different concentrations (<0.1% for all concentrations) (**Figure 5D**). These results suggest that the specificity of the response mode in boutons is maintained across a 100-fold increase in concentration. Similarly, across concentrations, the percentage of responding boutons in the GCL remained largely invariant (10^{-4}: 39%, 10^{-3}: 40% and 10^{-2}: 40%; 12 FOVs, 3 mice), where boutons exhibiting suppressed responses were predominant (10^{-4}: 39%, 10^{-3}: 39% and 10^{-2}: 39.5%) compared to enhanced boutons (10^{-4}: 0.2%, 10^{-3}: 0.6% and 10^{-2}: 0.8%) (**Figure 5C**).

Akin the results obtained using the 16-odor set, suppressed responses were more common than enhanced responses across both layers, and the low percentage of boutons responding with enhancement likely reflects the small odor set (5 odors) used for this experiment. The population mean response amplitude (dF/F) for responding boutons was largely invariant across odor concentrations in the GL (enhanced, 10^{-4}: 0.5 ± 0.27 SD, 10^{-3}: 0.47 ± 0.2 SD and 10^{-2}: 0.54 ± 0.28; suppressed, 10^{-4}: –0.1 ± 0.1 SD, 10^{-3}: –0.1 ± 0.1

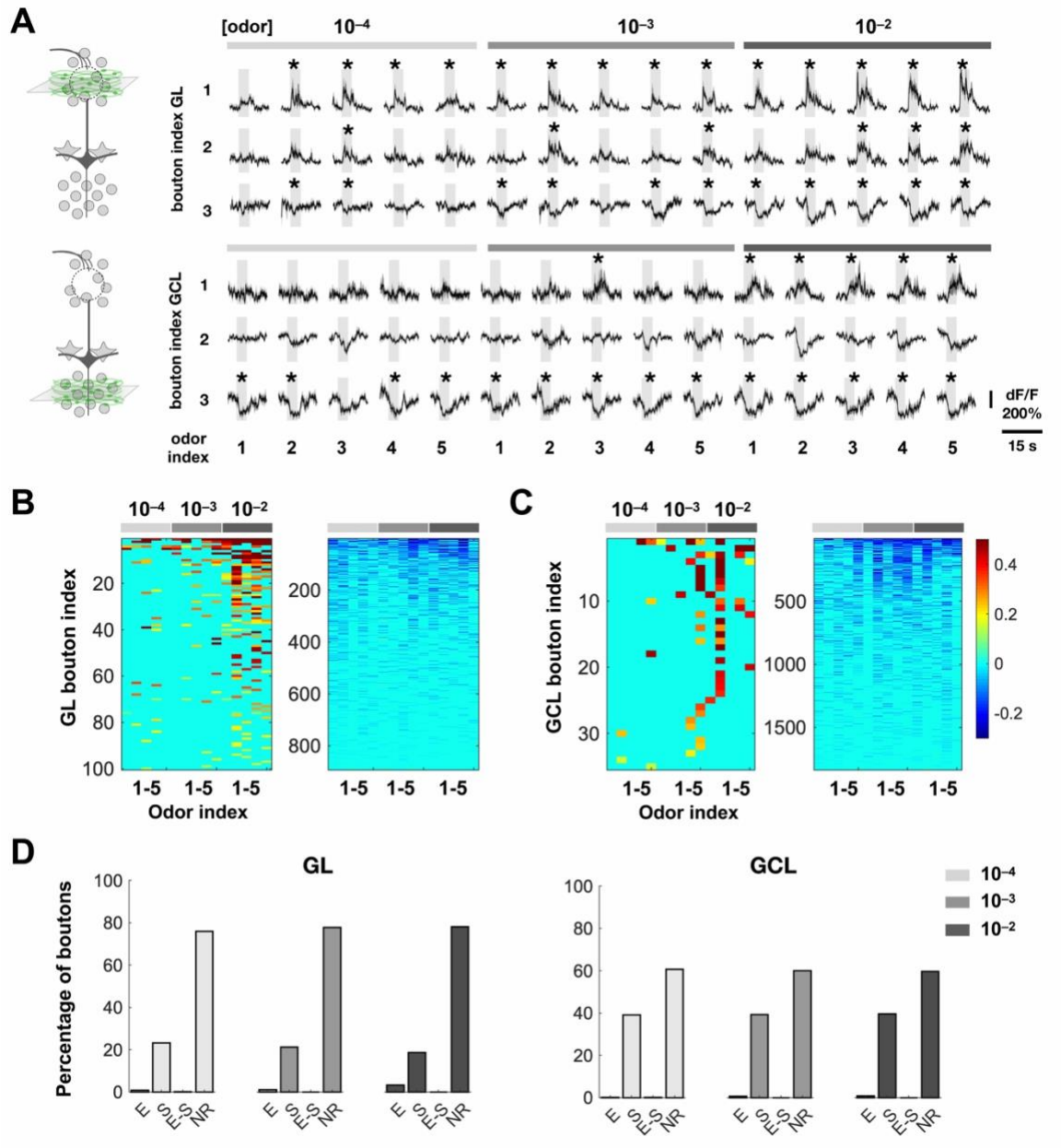

Fig. 5: *Odor responses dynamics and mode are invariant across concentrations*

(A) Mean responses for 3 boutons in the GL (top) and in the GCL (bottom) to 5 odors (ethyl tiglate, isoamyl acetate, valeraldehyde, ethyl valerate and heptanal) at 3 different dilutions (10^{-4}, 10^{-3} and 10^{-2}, top horizontal bars color coded for each concentration). Asterisks indicate significant responses (see Methods) and gray vertical bar indicates odor presentation. Heatmaps for the population of boutons in the GL (15 FOVs, 3 mice) **(B)** and GCL (12 FOVs, 3 mice) **(C)** that responded significantly to at least one odor stimulus; each row corresponds to a single bouton. Consecutive columns represent odors 1 to 5, each presented at three different

concentrations shown on the top horizontal bars. **(D)** Percentage of boutons in the GL (left) and GCL (right) that responded to an odor presentation exclusively with enhancements (E), suppressions (S), exhibited both E or S (E-S); NR, non-responsive boutons.

SD and 10^{-2}: –0.1 ± 0.1 SD), and in the GCL (enhanced, 10^{-4}: 0.65 ± 0.28 SD, 10^{-3}: 0.58 ± 0.25 SD and 10^{-2}: 0.65 ± 0.27 SD; suppressed, 10^{-4}: –0.12 ± 0.1 SD, 10^{-3}: –0.12 ± 0.1 SD and 10^{-2}: –0.13 ± 0.1 SD). In sum, the overall mode and dynamic of the responses to odors remained unaffected by changes in concentration.

Discussion

We demonstrate the existence of a fast GABAergic feedback loop driven by glutamatergic inputs from the PC onto OB projecting MCPO neurons (**Figure 1**). We further characterized the odor-evoked dynamics of calcium signals in MCPO GABAergic boutons in the OB and show that odor responses in the GABAergic boutons are sparse, specific, and diverse across the superficial and deeper layers of the bulb (**Figure 2, 3**). Odor-evoked responses had a fast time course (**Figure 4**), and across multiple odors, we observed both enhancement and suppression of baseline activity (**Figure 2, 5**). The prevalence of these opposite responses was maintained through odor intensities (**Figure 5**), suggesting high selectivity in their response mode.

The direct stimulation of MCPO GABAergic neurons by PC inputs is consistent with previous studies showing cortical innervation of the BF and supports the possibility that odor stimuli can modulate the activity of the OB projecting GABAergic neurons. A previous study showed that electrical stimulation of the piriform or entorhinal cortex

evokes monosynaptic excitation of neurons in the MCPO; however, the identity of the neurons in these studies could not be determined as in our study (Paolini and McKenzie, 1997). In addition, an anatomical analysis suggested that neocortical, prefrontal, and piriform cortex axons innervate inhibitory and non-cholinergic neurons of the BF (Zaborszky et al., 1997). Our imaging results indicate that the activity of boutons in MCPO GABAergic axons innervating the OB is rapidly modulated by odor presentations (**Figure 2, 4**), possibly reflecting the integration of direct inputs from the PC, as shown *in vitro* (**Figure 1**). However, it is possible that, in addition, the MCPO GABAergic neurons could integrate neuromodulatory activity in the BF driven by indirect inputs from other brain regions or local circuits (Gaykema and Zaborszky, 1997; Zaborszky et al., 1999, 2012; Brown and McKenna, 2015). It should be noted that changes in bouton activity in the OB could also arise from direct presynaptic regulation in the OB (Villar et al., 2021b). We have recently shown that muscarinic activation strongly suppressed GABA release from MCPO GABAergic axons in the OB (Appendix A), indicating an extra layer of complexity in the regulation of activity dynamics of the GABAergic feedback axons. Further studies will address these possibilities.

Interestingly, odor presentation resulted in both enhanced and suppressed bouton responses (**Figure 2, 4**), which suggests that upon odor presentation, local circuits in the MCPO may implement different input-output transformations on the GABAergic projection neurons, resulting in distinct output channels. In fact, the BF contains a large number of inhibitory neurons, of which only a small percentage corresponds to long-range projection neurons. Previous evidence indicates that a subpopulation of MCPO neurons that exhibit monosynaptic excitation upon piriform or entorhinal cortex electrical

stimulation also receives also polysynaptic inhibition (Paolini and McKenzie, 1997). In our recordings, we observed only fast synaptic responses. Therefore it is possible that other OB projecting GABAergic neurons, underrepresented in our recordings, exhibit polysynaptic inhibitory responses (see below, and Chapter 4). Local synaptic processing in the MCPO may give rise to more complex activation dynamics of projection GABAergic neurons, thus diversifying their effects on the target circuits. Suppressive responses were mostly observed in boutons with high basal calcium signal, suggesting a difference in the basal activity of the GABAergic neurons could lead to a different response on the output neurons. For example, enhanced GABAergic bouton activity may allow disinhibition of M/TCs by reducing the activity of local GABAergic circuits (Böhm et al., 2020; Villar et al., 2021a). In contrast, the inhibition of tonic release of GABA from boutons can have the opposite effect on M/TCs (i.e., inhibition). Most odor-evoked responses in GABAergic boutons corresponded to suppression, indicating that activation of the MCPO GABAergic feedback driven by odor encounters is likely to sparsen the output of the bulb.

Our results indicate significant differences between the response profile of GABAergic boutons in the superficial and deeper layers of the OB. These differences could, in principle, be explained by a better optical access and higher detectability of GCaMP signals in the GL compared to GCL. However, this is unlikely as recordings in the deeper GCL showed a higher percentage of responding boutons compared to the GL (**Figure 2F**), and suppressed responses, which occurred in boutons with a higher baseline activity, were more common in the GCL than in the GL (**Figure 2G**). In addition, detectable boutons were slightly more numerous in deeper layers compared to the surface (**Figure 2-1D**). Alternatively, axons innervating the GL and GCL may belong to different

populations of MCPO neurons. Consistent with this idea, subpopulations of GABAergic neuron types have been identified in the BF of rats (Gritti et al., 2003; Zaborszky et al., 2005) and mice (McKenna et al., 2013; Xu et al., 2015) (see also Chapter 4). Often, GABAergic subpopulations have biases in their projection patterns, as well as local connectivity and function (Kepecs and Fishell, 2014; Yang et al., 2017). Differential control of the GL versus the GCL by MCPO GABAergic neurons may provide the OB with a mechanism for specific regulation of local GABAergic circuits, known to play essential roles in olfactory processing (Abraham et al., 2010; Fukunaga et al., 2014; Gschwend et al., 2015; Li et al., 2018).

Functionally, the GL implements gain control mechanisms and decorrelation of odor representations by a diverse population of glomerular GABAergic neurons, which drive feedforward inhibition onto the M/TCs (Wilson and Mainen, 2006; Zhu et al., 2013a; Banerjee et al., 2015). In turn, GABAergic cells in the GCL provide spatial contrast mechanisms that sharpen the tuning of M/TCs receptive fields through a large number of reciprocal synaptic interactions between GCs and M/TCs (Yokoi et al., 1995; Urban and Sakmann, 2002; Egger et al., 2003, 2005). The difference in odor response dynamics of the MCPO GABAergic boutons in the GL and GCL may reflect independent and specific control of these functional domains of the bulb. Interestingly, odor responses by the GL GABAergic boutons were more similar across stimuli than responses in GCL boutons, suggesting that less odor-specific GABAergic signals regulate the sensory input to the OB glomeruli, while more odor-specific inhibitory signals modulate the function of the local GABAergic circuits in the GCL. Intriguingly, although the odor-evoked dynamics of the PC glutamatergic feedback also differ across layers in the bulb, the feedback boutons in

the GL exhibit a narrower tuning (i.e. more odor-specific), compared to boutons in the GCL (Otazu et al., 2015). This suggests that across layers, the influence of these opposite signals may have a different function.

The existence of distinct channels in the MCPO and PC inputs to the bulb with distinct responses to odor stimuli may provide flexible top-down feedback signals important for fine odor discrimination. Our results and previous studies (Boyd et al., 2015; Otazu et al., 2015) indicate that the glutamatergic and GABAergic feedbacks are rapidly recruited by olfactory cues and are capable of influencing the OB output neurons (Boyd et al., 2012; Villar et al., 2021a). Thus, glutamatergic and GABAergic inputs to the local GABAergic network from the PC and MCPO, respectively, are well-positioned to rapidly modulate the extent to which the local GABAergic network influences the activity of a particular population of M/TCs in a context-dependent manner. Future behavioral experiments where mice perform rapid odor discriminations and changes in stimulus contingency while monitoring the activity of the PC and MCPO axons in the bulb will be required to determine whether these descending signals support behavioral flexibility. Alternatively, the distinct feedback channels for the MCPO and PC signals may be required to implement a predictive sensory coding strategy (Keller and Mrsic-Flogel, 2018). In this model, the OB continuously compares bottom-up sensory inputs to predictive feedback signals from top-down areas; the difference between these two signals is the updated output of the bulb. Thus, when sensory information does not match the predictive signals, the comparator circuit (e.g., OB) generates negative or positive prediction errors depending on the sensory expectations. Activating the MCPO and PC feedbacks produce opposing effects on the bulb output. Therefore, they are ideally positioned to integrate sensory

predictive signals and provide the bulb with fast context-dependent modulatory feedback that can alter the polarity of the OB output. Future experiments evaluating the existence of internal sensory representations will be needed to test whether the olfactory system uses a predictive coding strategy.

Chapter 4

Parallel projections of basal forebrain GABAergic neurons to the olfactory bulb

Acknowledgments

We thank Ms. Meghan Deyesu for help in histology experiments and Dr. Arun Narasimhan for help in whole brain imaging experiments. This research was supported by the National Institute on Aging of the National Institutes of Health, Grant AG-049937A to Dr. Ricardo C. Araneda.

Summary

Early olfactory processing is flexibly adjusted by descending feedback projections from multiple brain regions. Among these areas, the basal forebrain (BF) contains varied populations of cells including GABAergic and cholinergic neurons that innervate the olfactory bulb (OB) and regulate its neural output. While the functional roles for cholinergic modulation in the OB has been proposed, less is known about the role of BF inhibition to the OB in odor processing. Here, we use viral tracing and slice electrophysiology in male and female mice acute brain slices to investigate the cellular diversity of the BF GABAergic output neurons and their innervation by the piriform cortex. Whole brain imaging indicated that most top-down GABAergic projections to the bulb concentrate in a BF nucleus called magnocellular preoptic area (MCPO), with a small number of neurons found in nearby areas. The MCPO consisted of at least two non-overlapping populations of neurons, characterized by the expression of the cellular markers somatostatin (Sst) and calretinin (Cr) which differentially targeted the glomerular and inframitral layers, respectively. We demonstrate that fast glutamatergic inputs from the piriform cortex elicited responses in Sst but not Cr neurons. Surprisingly, nearby cholinergic neurons, which like GABAergic neurons also project to the bulb, did not exhibit fast glutamatergic responses following activation of PC axons. These results suggest a high degree of circuit specialization among the BF neuromodulatory neurons that project to the OB. Furthermore, our results provide support for the existence of a long-range feedback loop that can recruit BF GABAergic cells through direct PC glutamatergic inputs that drive a fast feedback inhibition to the OB.

Introduction

Sensory perception requires the coordination of sizable neuronal assemblies across multiple brain regions; yet the mechanism that drives this coordination is not understood. Previous studies have shown that long-range projecting neurons influence the activity of interconnected brain regions, modulating specific circuit domains in the target areas (Jinno et al., 2007; Melzer et al., 2012; Kim et al., 2015a; Leong et al., 2016), and are necessary for sensory binding and memory formation (Buzsáki and Chrobak, 1995; Basu et al., 2016; Melzer and Monyer, 2020). In the mammalian olfactory system, early processing of sensory signals in the olfactory bulb (OB) is highly influenced by top-down projecting neurons (Matsutani and Yamamoto, 2008; Boyd et al., 2012, 2015; Markopoulos et al., 2012; Nunez-Parra et al., 2013; Rothermel and Wachowiak, 2014; Rothermel et al., 2014; Otazu et al., 2015). Among these projections, GABAergic and cholinergic neurons in the basal forebrain (BF) innervate the OB and modulate the activity of the bulb output neurons, the mitral and tufted cells (M/TCs) (Castillo et al., 1999; Ghatpande et al., 2006; Pressler et al., 2007b; Gracia-Llanes et al., 2010; Nunez-Parra et al., 2013; Smith et al., 2015; Sanz Diez et al., 2019; Böhm et al., 2020; Hanson et al., 2020; Villar et al., 2021a).

GABAergic cells clustered in the magnocellular preoptic area (MCPO) of the BF innervate upstream olfactory areas, including the piriform cortex (PC) and anterior olfactory nucleus (AON) (Luiten et al., 1987; Gritti et al., 1997; Zaborszky et al., 1999). However, the way in which they influence olfactory processing and whether the BF GABAergic output produces a broad regulation of these brain regions is unknown. Interestingly, electron microscopy studies have shown some degree of synaptic

organization in cortical inputs to the BF, supporting the possibility of a rapid recruitment of BF circuits by cortical excitatory neurons (Zaborszky et al., 1997, 1999, 2012).

Here, we examined the population diversity and connectivity of BF long-range GABAergic neurons (LRGN) with olfactory areas using viral tracers, conditional genetics, and whole cell electrophysiology to selectively access neuronal populations in the MCPO. We found that a heterogeneous population of GABAergic neurons in the MCPO produce a differential projection pattern to olfactory areas. Sst^+ and Cr^+ GABAergic neurons exhibited biased projection patterns to the superficial and deeper cellular layers of the OB, respectively. Importantly, we demonstrate that optogenetic activation of PC afferents to the MCPO evoked short latency glutamatergic inputs into Sst^+ but not Cr^+ GABAergic neurons. Interestingly, nearby cholinergic neurons failed to exhibit excitatory responses. Together, we provide functional evidence that supports the existence of a long-range neuronal circuit between the OB, olfactory cortex and the MCPO that can support rapid recruitment of GABAergic neuromodulation upon activation of the olfactory pathway.

Methods

Animals. All experiments were conducted following the US National Institute of Health guidelines and approved by the Institutional Animal Care and Use Committee of the University of Maryland, College Park. Histological experiments and electrophysiological recordings were performed on C57BL/6 (JAX, stock #664), *Gad2-IRES-Cre* (JAX, stock #010802), *Vgat-IRES-Cre* (JAX, stock #028862), *VGlut1-IRES-Cre* (JAX, stock #023527), *VGlut2-IRES-Cre* (JAX, stock #028863), *Sst-IRES-Cre* (JAX, stock

#013044), *Cr-IRES-Cre* (JAX, stock #010774) and *PV-IRES-Cre* (JAX, stock #017320). Experiments were conducted in female and male mice ranging 1 to 5-months old, obtained from breeding pairs housed in our animal facility.

Stereotaxic injections. The surgical procedure for targeted expression of genes of interest in the different transgenic lines was done as previously described (Villar et al., 2021a). For Cre-dependent anterograde expression of genes, *Vgat-Cre*, *Sst-Cre*, *Cr-Cre* or *PV-Cre* mice received a stereotaxic injection of either an AAV5-CAG-Flex-tdTomato or an AAV5-CAG-Flex-ChR2-tdTomato adenovirus (200 nL each, Addgene Catalog #28306 and #18917, respectively) into the MCPO. For retrograde tracing *Vgat-Cre*, *Sst-Cre*, *Cr-Cre* or *PV-Cre* mice received a stereotaxic injection of the AAVrg-hSyn-DIO-eGFP virus (50 nL, Catalog #50457, Addgene) into the OB. After the surgery, animals were left to recover for at least 3 weeks before experiments. The Sst^+ and Cr^+ retrolabeled neurons located in the same anatomical region labeled when injecting the retrograde virus in the OB of *Vgat-Cre* mice (A/P +0.25 to –0.35 mm from bregma), which corresponds to the MCPO/SI area (Paxinos and Franklin, 2004). For anterograde expression of ChR2, or for tracing of projections from PC and the AON, C57BL/6 mice received an injection of the AAV5-CAG-tdTomato or AAV5-CAG-ChR2-mCherry adenovirus (80 nL, Addgene), using the following stereotaxic coordinates (in mm): PC, D/V –3.5, M/L ± 2.8, A/P 1.6 and AON, D/V –3.2, M/L ± 1, A/P 2.7.

Confocal imaging and immunofluorescence. The visualization of the expression of the reporter genes was conducted in fixed brains as previously described (Villar et al.,

2021a). To examine cellular organization, nuclei were stained with DAPI dihydrochloride (300 nM, Catalog #D1306, Invitrogen). For immunohistochemistry experiments, 50 µm thick free floating brain slices were incubated with the following antibodies: goat anti-Cr (1:100, Millipore, Catalog #1550), rat anti-Sst (1:100, Sigma, Catalog #MAB354), mouse anti-PV (1:300, Swant, Catalog #PV235), rabbit anti-Gad65/67 (1:100, OWL, Catalog #56483), and rabbit anti-GFP (1:300, MBL, Catalog #598). Primary antibodies were developed using the following secondary antibodies (1:500, Invitrogen): donkey anti-goat coupled to Alexa-647 (Catalog #A-21447) or coupled to Alexa-488 (Catalog #A-11055), donkey anti-rat coupled to Alexa-488 (Catalog #A-21208), donkey anti-mouse coupled to Alexa-488 (Catalog #A-21202) and donkey anti-rabbit coupled to Alexa-594 (Catalog #A-21207). Control sections, not exposed to the primary antibody, were devoid of immunostaining and were used to set background values on the microscope. Images were acquired using a Leica SP5X confocal microscope, with appropriate brightness and contrast adjustments, and immunostained cells counted blindly using ImageJ (NIH) or MATLAB (MathWorks).

Whole-brain imaging. Imaging of *Vgat-Cre* brains injected with the AAVrg-DIO-eGFP virus in the OB was achieved using automated whole-brain serial two-photon tomography (STPT, TissueCyte 1000, TissueVision). Briefly, the brain was coronally imaged at a x, y resolution of 1 µm and z-spacing of 50 µm. Image files were reassembled in 2D and 3D using custom built software (Ragan et al., 2012; Kim et al., 2015b, 2017). Whole-brain 3D datasets were registered to the OstenRef reference (RSTP) brain using the auto-fluorescent background channel (Kim et al., 2015b, 2017). In brief, a 3D affine

transformation was calculated first, followed by a 3D B-spline transformation. Similarity was computed using advanced Mattes Mutual Information metric in the elastix 2.0 registration toolbox (Klein et al., 2010). We used the ImageJ plugin TRAKEM2 to manually mark the position of the labeled somas (Cardona et al., 2012). Using custom-written scripts, the centroids of these somas were registered to the RSTP brain using the same registration parameters. The region-wise counts were then extracted to provide a list of the number of neurons from each brain region that projected to the OB.

Whole cell recordings. Whole-cell recordings were performed using a dual EPC10 amplifier (HEKA, Harvard Bioscience) in coronal slices containing MCPO, PC or AON and horizontal OB slices (250 µm), prepared using as before (Villar et al., 2021a). Briefly, the different brain regions were sections in oxygenated ice-cold artificial cerebrospinal fluid (ACSF) containing lower Ca^{2+} (0.5 mM) and higher Mg^{2+} (3 mM) and let to recuperate for at least 30 min at 35°C before electrophysiological recordings. The normal ACSF had the following composition (in mM): 125 NaCl, 26 $NaHCO_3$, 1.25 NaH_2PO_4, 2.5 KCl, 2 $CaCl_2$, 1 $MgCl_2$, 1 myo-inositol, 0.4 ascorbic acid, 2 Na-pyruvate, and 15 glucose, continuously oxygenated (95% O_2, 5% CO_2) to give a pH 7.4. For voltage-clamp recordings, pipettes were filled with an internal solution of the following composition (in mM): 125 Cs-gluconate, 4 NaCl, 10 Na-phosphocreatine, 10 HEPES-K, 2 Na-ATP, 4 Mg-ATP and 0.3 GTP (pH 7.3, ~290 mOsm). For current clamp recordings, the internal solution had the following composition (in mM): 120 K-gluconate, 10 Na-gluconate, 4 NaCl, 10 HEPES-K, 10 Na-phosphocreatine, 2 Na-ATP, 4 Mg-ATP and 0.3 GTP (pH 7.3, ~290 mOsm). Under the recording conditions, the patch pipettes had a resistance of 2-8

MΩ. For optogenetic stimulation, a LED lamp (COP1-A, Thorlabs) was used to produce brief pulses (0.5-1 ms) of collimated blue light (473 nm, 1 mW/mm^2) delivered through the microscope objective.

Data analysis. Electrophysiological recordings were analyzed in MATLAB (MathWorks) or Igor Pro (WaveMetrics). The rise time of synaptic currents was calculated as the time from 10% to 90% of the current peak. The decay time was measured by fitting a double exponential decay function to the current relaxation and computing the weighted time constant (τ_w) as,

$$\tau_W = \frac{(a_1\tau_1 + a_2\tau_2)}{(a_1 + a_2)}$$

where a and τ are the amplitude and time constant of the first (1) and second (2) exponentials, respectively. Data is shown as the mean ± S.E.M, unless otherwise specified. Statistical significance was determined by student's t-test or Wilcoxon rank sum (* = $p<0.05$, ** = $p<0.01$, *** = $p<0.001$).

Pharmacological agents. Drugs were prepared from stocks stored at –20°C, diluted into ACSF and perfused at a speed of ~2 mL/min; SR 95531 (Gabazine, Catalog #1262, Tocris), 6-cyano-7-nitroquinoxaline-2,3-dione (CNQX disodium salt, Catalog #1045, Tocris), D-(-)-2-amino-5-phosphonopentanoic acid (D-AP5, Catalog #0106, Tocris), tetrodotoxin (TTX, Catalog #1078, Tocris), 4-aminopyridine (4-AP, Catalog #0940, Tocris).

Results

Sources of afferent GABAergic projections to the olfactory bulb

We have previously described the function of groups of BF GABAergic neurons that project to the OB that reside in the MCPO and demonstrated that this nucleus provides a rich source of feedback inhibition to the OB circuits (Gracia-Llanes et al., 2010; Nunez-Parra et al., 2013; Villar et al., 2021a). Intriguingly, a recent study described the function of a subset of OB projecting GABAergic neurons located in the olfactory cortex, suggesting that besides the BF other regions, including the cortex, could exert an inhibitory regulation in the OB (Mazo et al., 2020). Surprisingly, up to date there has not been a systematic analysis of the sources of GABAergic afferents to the OB. To fill this gap, we performed a detailed whole-mount brain analysis to define the regions that provide GABAergic inputs to the bulb using a Cre-dependent retrograde adenovirus (AAVrg-DIO-eGFP) (Tervo et al., 2016) injected into the OB of *Vgat-Cre* mice (**Figure 1A**). We imaged the brain at a x, y resolution of 1 µm using automated serial two-photon tomography, and to accurately map the different brain structures the images were registered to a reference brain (see Methods). In a subset of representative brain slices, the GFP fluorescence was enhanced using immunohistochemistry (**Figure 1B, C**). Interestingly, analysis of the whole brain reconstructions revealed two main sources of GABAergic projections to the OB. In

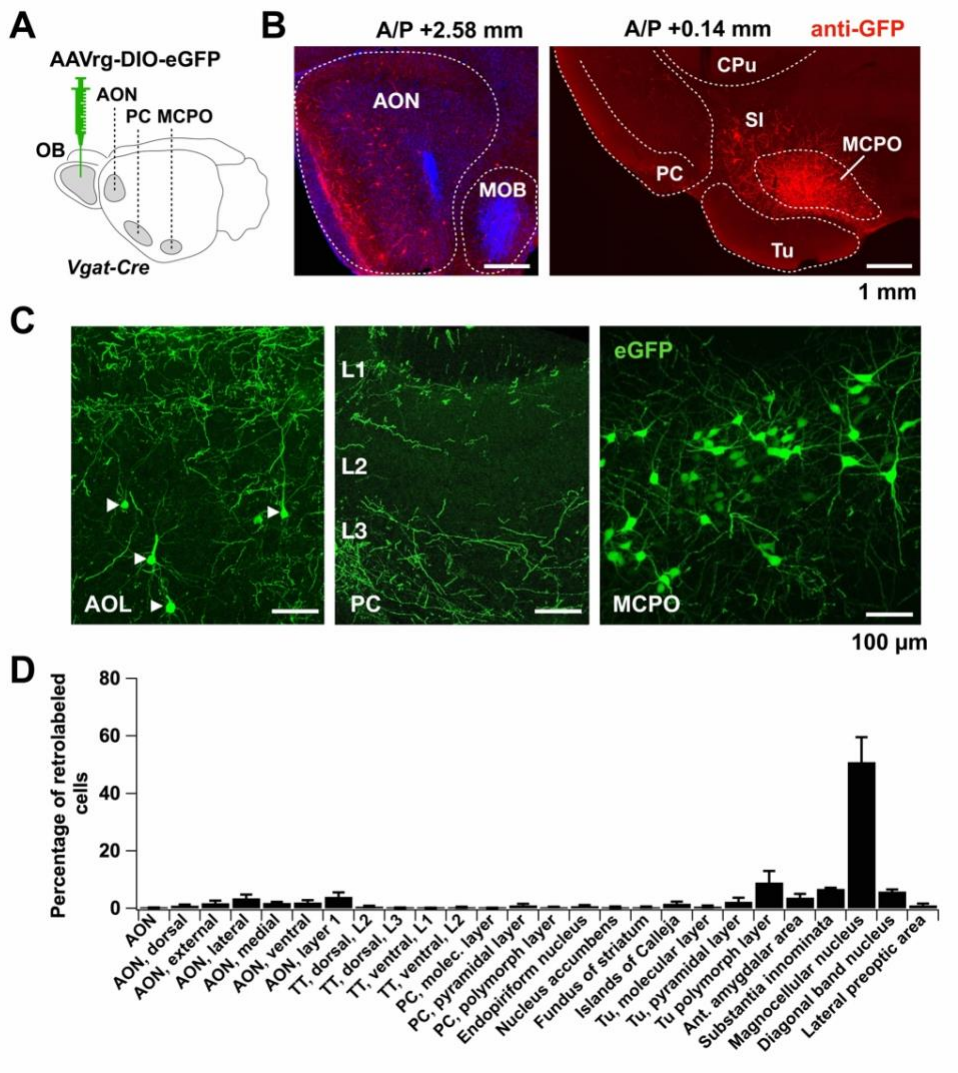

Fig. 1: *The MCPO and AON represent the main source of GABAergic efference to the bulb*

(A) The Cre-dependent retrograde tracer AAVrg-DIO-eGFP was injected into the OB of *Vgat-Cre* mice and the brain was coronally sliced and imaged using automated serial two-photon tomography to visualize fluorescently labeled neurons. **(B)** Examples of retrolabeled Vgat neurons in the AON (left) and MCPO (right). The fluorescence of the transduced neurons was enhanced using immunohistochemistry against GFP. Nuclear dapi staining is shown in blue. No significant staining was observed in the olfactory tubercle (Tu) or the piriform cortex (PC). SI, substantia innominata; CPu, caudate putamen. **(C)** Left, AON magnification showing sparse retrolabeling of neurons in deep layers of the lateral AON (AOL). Center, axonal collaterals from retrolabeled neurons in the MCPO are visible across different layers (L1, L2 and L3) of the PC. Right, magnification of the MCPO showing a cluster of retrolabeled neurons. **(D)** Bar plot showing cell body quantification across multiple brain regions (n= 4 brains). TT, tenia tecta.

agreement with previous work, the largest number of neurons in a region of the BF corresponding to the caudolateral portion of the horizontal limb of the diagonal band (HDB), that comprises the MCPO, substantia innominata (SI) and diagonal band nucleus. A significantly smaller number of labeled neurons were found in the anterior olfactory nucleus (AON) (**Figure 1D**), and an even sparser labeling was present in the anterior PC (**Figure 1C, D**). Overall, the BF contained ~65% of all retrolabeled neurons, while the AON ~14% and PC ~2% (n= 4 brains). Although, the relevance in OB regulation that the small population of GABAergic neurons located in olfactory cortex has (Mazo et al., 2020), our results strengthen the notion that the BF, and in particular the MCPO, is the main source of GABAergic regulation to the OB (**Figure 1D**). Additional experiments where OB centrifugal projections are accessed using different retrograde tracing methods, such as subunit B of cholera toxin (CTB) or latex microspheres (Lumafluor) particles together with immunohistochemistry against GABAergic markers, will be necessary to corroborate our results and rule out potential tropism by the retrograde adenovirus.

Diversity of OB projecting BF-LRGNs

The BF contains a heterogeneous group of GABAergic neurons classified according to the expression of specific cellular markers, including Sst, Cr and parvalbumin (PV) containing neurons (Caputi et al., 2013). Across cortical circuits, these cell types usually express distinctive physiological properties (Kepecs and Fishell, 2014), however the heterogeneity and physiological diversity of OB-projecting BF GABAergic neurons are unknown. Therefore, we first examined the abundance of the different GABAergic

populations in the MCPO by immunostaining against the specific cell-type markers (**Figure 2A**, **Figure 2-1**), while labeling the overall GABAergic population with an antibody that binds to both isoforms of the GABA synthesizing enzyme Gad, Gad-65 and Gad-67 (Gad65/67). Double-staining revealed that Sst, Cr and PV expressing neurons were present in different proportions among the GABAergic neurons, with Cr containing GABAergic neurons being the most abundant (**Figure 2A**, **Figure 2-1A-C**, Cr^+ 32.2%: Cr^+ 391 cells, $Gad65/67^+$ 1214 cells; n= 3). Both Sst^+ and PV^+ containing neurons were equally abundant but in a smaller number (Sst^+ 19.5%: Sst^+ 43 cells, $Gad65/67^+$ 221 cells; n= 3; PV^+ 17%: PV^+ 88 cells, $Gad65/67^+$ 517 cells; n= 3). In a subset of brain sections, we immunostained for the three markers simultaneously, and found that these neuronal types represent non-overlapping populations (n= 3) (**Figure 2A**), consistent with previous studies in the BF of rats (Gritti et al., 2003; Zaborszky et al., 2005).

Additionally, we conducted targeted whole cell recordings from fluorescently labeled subtypes of GABAergic neurons in the MCPO (see Methods) (**Figure 2B**). Sst neurons (n= 7), appear large and were characterized by a resting membrane potential (V_m) of –64 ± 0.9 mV, an input resistance (R_m) of 830 ± 112 MΩ, a capacitance of 49 ± 7.6 pC with a maximal firing rate of 22.4 ± 3 Hz (100 pA). In contrast, MCPO Cr neurons (n= 6) had a more depolarized V_m (–57 ± 2.2 mV), higher R_m 1.4 ± 0.3 GΩ, a capacitance of 57 ± 7.7 pC and a maximal firing rate of 14.3 ± 1 Hz (40 pA). In comparison, PV neurons (n= 2) had a higher maximal firing rate (114 ± 60 Hz) as previously described for this cell type (McKenna et al., 2013).

To identify the subtype of MCPO GABAergic neurons that project to the bulb, we conducted retrolabeling by injecting the AAVrg-DIO-eGFP virus into the OB of *Sst-Cre*,

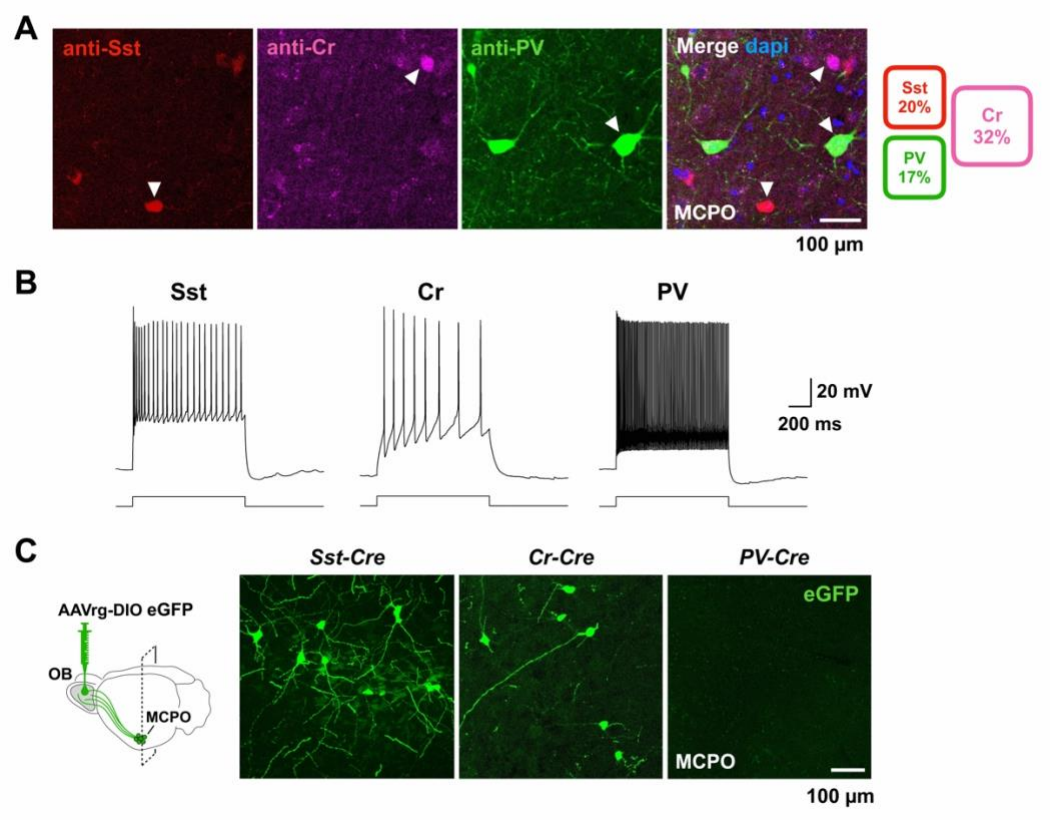

Fig. 2: *Sst and Cr subtypes of MCPO GABAergic neurons project to the olfactory bulb*

(A) Confocal images of the MCPO immunostained with antibodies against Sst (red), Cr (magenta), PV (green). Nuclear dapi staining is shown in blue. This representative image illustrates the lack of colocalization of the three GABAergic markers in neurons of the MCPO. Right, diagram illustrating the abundance of the three GABAergic subtypes over the total GABAergic population (Gad65/67); Cr 32%, Sst 20% and PV 17% (n= 3). See also **Figure 2-2** (Appendix B). **(B)** Current clamp recordings from identified somatostatin (Sst, n= 9), calretinin (Cr, n= 6) and parvalbumin (PV, n= 2) neurons in slices of the MCPO. A depolarizing current step (bottom trace) elicits a distinctive firing pattern in the GABAergic subtypes. *Sst-Cre*, *Cr-Cre* and *PV-Cre* mice were injected in the BF with an AAV-Flex-GFP virus to identify the different cell types by the expression of GFP. **(C)** Diagram, the Cre-dependent retrograde tracer AAVrg-DIO-eGFP was injected into *Sst-Cre*, *Cr-Cre* or *PV-Cre* mice to specifically access populations of MCPO-OB projecting neurons. Retrogradely labeled cells were visualized in coronal sections of BF. There are abundant retrolabeled neurons in the MCPO of *Sst-Cre* and *Cr-Cre* mice, but not in *PV-Cre* mice. Immunohistochemistry for Sst, Cr and PV over the Gad65/67 population is shown in **Figure 2-2** (Appendix B). Retrograde tracing of Vglut1 and Vglut2 projections to the OB is shown in **Figure 2-3** (Appendix B).

Cr-Cre mice or *PV-Cre* mice, respectively. For these experiments, we immunostained against GFP to increase the likelihood of detecting the transduced cell bodies. Three weeks after the injection, we found abundant retrolabeled Sst^+ neurons, and a lower number of Cr^+ neurons in the MCPO (**Figure 2C**). Intriguingly, we found no retrolabeled PV^+ neurons, indicating that this GABAergic neuron subtype does not project to the OB. Sst^+ retrolabeled cells were characterized by a large cell body area of 471 ± 157 SD μm^2 (81 cells, 13 slices, range 128 – 859 μm^2) and a mean long axis of 24 ± 5 µm, which was similar for Cr^+ neurons 492 ± 244 SD μm^2 (24 cells, 7 slices, range 186 – 1292 μm^2) and mean long axis of 23 ± 6 µm. The cell body size distributions for both subtypes were not significantly different (Wilcoxon, rank sum, p= 0.79), indicating that morphologically these two populations were indistinguishable. We found a similar homogeneous distribution of cell body size when we used the *Vgat-Cre* mouse to retrolabel the MCPO GABAergic neurons (**Figure 1B, C**); the average cell body size was 515 ± 204 SD (270 cells, 11 slices, range 203 – 1191 μm^2) and mean long axis of 24 ± 5 µm.

In addition to GABAergic neurons, the BF contains a population of glutamatergic neurons which has been shown to innervate the frontal cortex (Hur et al., 2009), lateral hypothalamus and somatosensory cortex (Hur and Zaborszky, 2005; Henny and Jones, 2008). Therefore, we wondered whether a similar projection of these excitatory neurons to the OB exist. To examine this possibility, we injected the AAVrg-DIO-eGFP virus into the OB of *Vglut1* and *Vglut2-Cre* mice and analyzed the GFP expression across multiple brain regions and did not find retrolabeled neurons in the MCPO (**Figure 2-2A, B**). In contrasts, abundant transduced Vglut1 or Vglut2 neurons were present in olfactory areas known to send glutamatergic feedback to the OB, such as the PC, AON and nucleus of the lateral

olfactory tract (nLOT) (**Figure 2-2C, D**). In sum, these results indicate that the feedback projections from the MCPO to the OB is mostly inhibitory, consisting of at least two distinct set of GABAergic neurons; Sst and Cr containing neurons.

Somatostatin and calretinin MCPO LRGNs differentially innervate layers of the bulb

To examine the projection patterns of the two OB-projecting GABAergic neurons, we injected the anterograde viral tracer AAV-Flex-tdTomato in the MCPO of *Sst-Cre* and *Cr-Cre* mice (**Figure 3A**). We found axonal innervation from both populations of GABAergic neurons in the OB; however, the projection pattern of Sst^+ neurons to the GL was significantly denser than those of Cr^+ neurons (**Figure 3B**). Instead, axonal projections of Cr^+ neurons were slightly denser in the GCL compared to GL (mean normalized pixel intensity; GL: Sst^+ axons 0.47 ± 0.001, Sst^+ axons 0.67 ± 0.005, n= 3; GCL: Cr^+ axons 0.73 ± 0.003, Sst^+ axons 0.47 ± 0.003, n= 3) (**Figure 3B**). These results indicate differential targeting of the OB layers by the MCPO Sst^+ and Cr^+ GABAergic neurons.

Previous studies have shown that MCPO GABAergic neurons form functional connections with inhibitory neurons of the OB (Gracia-Llanes et al., 2010; Nunez-Parra et al., 2013; Sanz Diez et al., 2019; Hanson et al., 2020; Villar et al., 2021a). The differential innervation pattern of these identified subpopulations prompted us to examine whether they also differ in their postsynaptic targets. Therefore, we drove cell-specific expression of channelrhodopsin-2 (ChR2) by injecting the Cre-dependent anterograde virus AAV-Flex-ChR2 into the MCPO of *Sst-Cre* and *Cr-Cre* mice. Consistent with the anatomical distribution of Sst^+ axons (**Figure 3C**), we found that a brief (0.5-1 ms) light stimulation

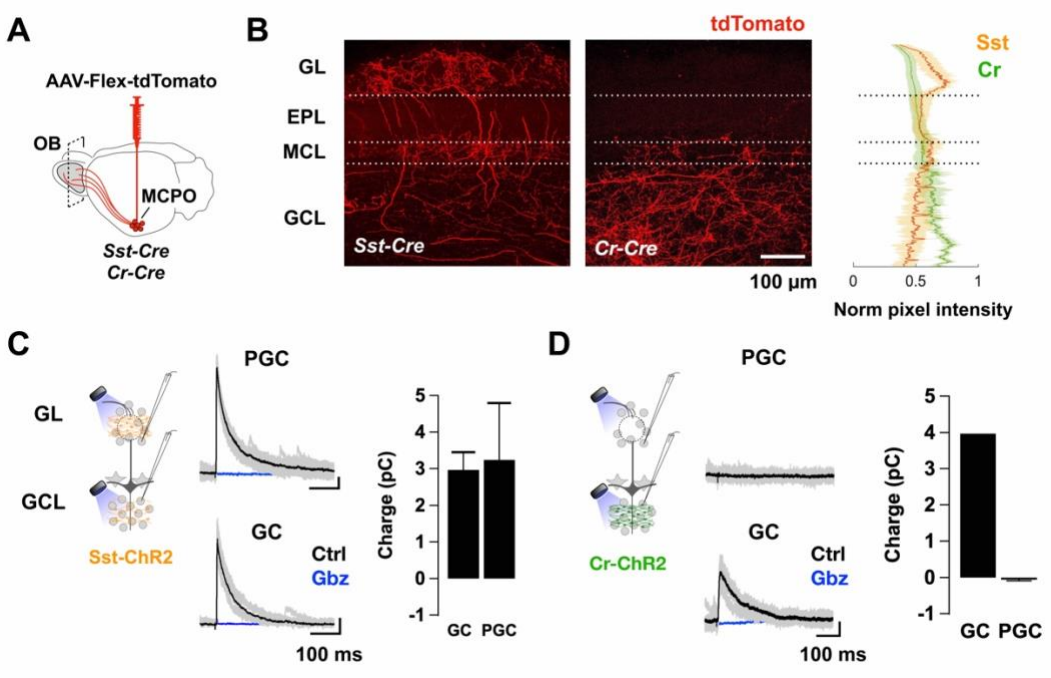

Fig. 3: *Sst and Cr GABAergic neurons of the MCPO exhibit a differential pattern of projections to the olfactory bulb*

(A) Diagram, the anterograde Cre-dependent viral tracer AAV5-Flex-tdTomato was injected in the MCPO of *Sst-Cre* or *Cr-Cre* mice to label a specific population. **(B)** Confocal images showing the axonal distribution of MCPO Cr and Sst neurons across the OB layer; projections of Cr-expressing neurons are absent in superficial layers of the OB (n= 3), while Sst-expressing neurons densely innervate the GL and the GCL (n= 3). Right, fluorescence intensity profile for Sst (orange) and Cr (green) axons across the OB layers. **(C)** Left diagram, ChR2 expression was achieved by injecting the AAV5-Flex-ChR2-mCherry virus in the MCPO of *Sst-Cre* mice (orange axons in the MOB). Targeted whole cell recordings were performed in both PGCs (top) and GCs (bottom). Right, examples of GABAergic currents obtained at 0 mV, using a Cs-gluconate based internal solution. A brief LED stimulation (~1 ms) elicited large outward currents in both cell types; individual trials are shown in gray and the average trace in black. The light-evoked currents were blocked by the $GABA_AR$ blocker gabazine (10 µM, Gbz) (blue trace). Right, quantification for Sst-ChR2 evoked responses as charge; prominent responses are found in both classes of inhibitory neurons of the OB. **(D)** Left diagram, Cre-dependent expression of ChR2 in Cr axons (green). Right, optogenetic stimulation reliably evoked gabazine sensitive currents in this GCs but not in PGCs. Right, charge quantification for Cr-ChR2 evoked responses in the different OB cell types.

evoked fast eIPSCs (Sst eIPSCs) in both GCs and PGCs (**Figure 3C**) (mean onset time, GCs: 5.5 ± 1.7 ms; PGCs: 4 ± 0.3 ms). In GCs, eIPSCs were characterized by a mean amplitude of 56.4 ± 1.4 pA, a rise time of 1.6 ± 0.06 ms and a decay time of 52.1 ± 1.3 ms (n= 294 events), while the eIPSCs in PGCs had a mean amplitude of 88 ± 2.7 pA, rise time 1.4 ± 0.05 ms and decay time of 56.9 ± 1.3 ms (n= 157 events) (**Figure 3C**). Interestingly, light activation of Cr^+ axons evoked GABAergic currents only in GCs. These elicited currents (Cr eIPSCs) were characterized by a mean amplitude of 40 ± 2.3 pA, a rise time of 8.8 ± 0.74 ms and a decay time of 182.7 ± 30.6 ms (n= 10 events) (**Figure 3D**). In contrast, light stimulation of Cr^+ axons failed to elicit IPSCs in PGCs (–0.06 ± 0.04 pC, n= 4 cells). As expected, the GABAergic responses were completely blocked by the $GABA_A$ receptor blocker gabazine (Gbz, 10 μM) (Sst IPSCs: GC, control, 3 ± 0.5 pC vs. Gbz, –0.05 ± 0.04 pC, n= 5, p= 0.004; PGC, 3.2 ± 1.6 pC vs. Gbz, 0.02 ± 0.005 pC, n= 3. Cr IPSCs: GC, control, 4 ± pC vs. Gbz, 0.1 ± pC, n= 1).

Olfactory cortical projections selectively target MCPO somatostatin neurons

We have previously shown that optogenetic stimulation of PC inputs onto MCPO produces a fast activation of GABAergic neurons (Chapter 3), however the identity of these neurons was not determined. Here, we investigated whether PC inputs innervate the two identified MCPO cell types that project to the OB, Sst and Cr containing GABAergic neurons. We identified MCPO Sst or Cr neurons by Cre-dependent expression of GFP and optogenetically stimulated PC axons expressing ChR2 in the PC (**Figure 4A**). Surprisingly,

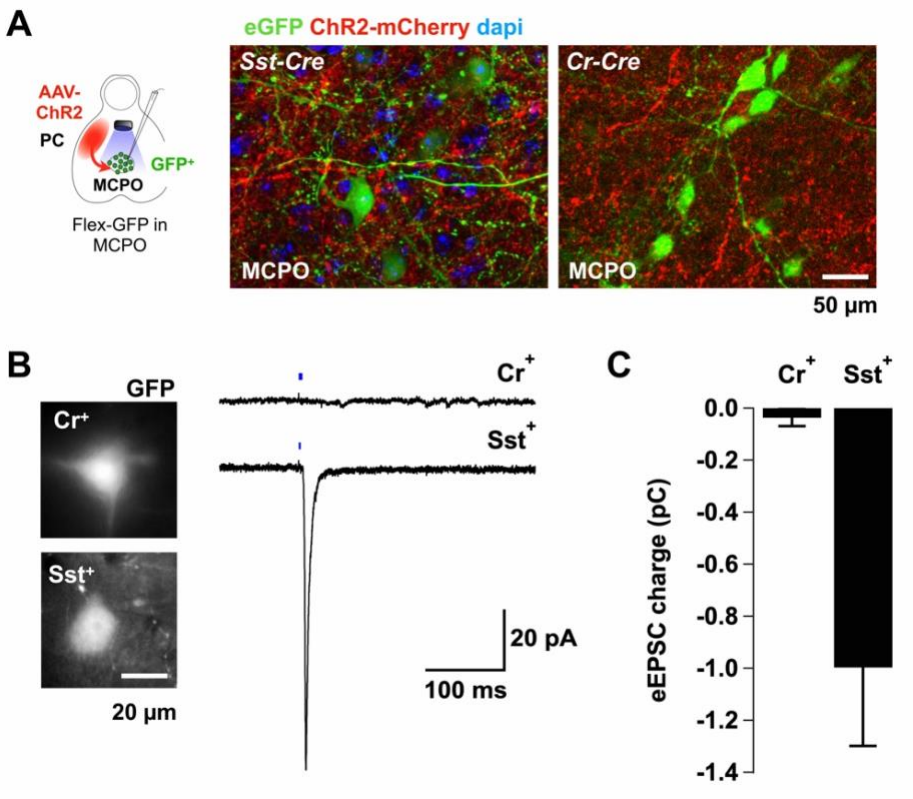

Fig. 4: *Excitatory projections from the PC target Sst but not Cr GABAergic neurons in the MCPO*

(A) Left diagram, anterograde ChR2 expression in PC neurons was driven by an injection of an AAV-ChR2-mCherry virus. Sst or Cr GABAergic neurons were labeled with GFP by injecting the AAV-Flex-eGFP virus in the MCPO of *Sst-Cre or Cr-Cre* mice, respectively. Left, confocal image of the MCPO of a *Sst-Cre* mouse showing GFP expressing Sst neurons (green) surrounded by abundant PC axons (red). Nuclear dapi staining is shown in blue. Right, image of the MCPO of a *Cr-Cre* mouse as shown on the left. **(B)** Left, targeted whole cell recordings were performed in brain slices containing MCPO from Cr (top image) or Sst (bottom image) GFP expressing neurons. Optogenetic stimulation of PC axons expressing ChR2 in the MCPO (5 ms) evoked excitatory currents in Sst neurons (bottom) but not Cr neurons (top). **(C)** Mean transferred charge during light stimulation of PC axons in Cr (n= 7) and Sst (n= 6) neurons. The holding potential was –70 mV.

light stimulation of PC axons (1-3 ms) in the MCPO elicited large excitatory postsynaptic currents (EPSC) in Sst but not Cr neurons (Sst, –1 ± 0.3 pC, n= 6; Cr, –0.04 ± 0.003 pA, n= 7) (**Figure 4B, C**). Importantly, light evoked EPSCs were observed in the same slices when recording from non-Cr MCPO neurons (GFP^-, –0.6 ± 0.4 pC, n= 3). These results indicate that PC descending inputs into the MCPO selectively target Sst neurons.

The excitatory currents evoked in Sst neurons exhibited short onset times (5.4 ± 0.5 ms, n= 7), suggesting monosynaptic inputs. Accordingly, the light evoked EPSCs were sensitive to TTX blockade (1 µM) (control, –1 ± 0.3 pC vs. TTX, 0.08 ± 0.01 pC, n= 6, p= 0.01), which was restored by the potassium channel blocker 4-AP (100 µM) (control, –1 ± 0.3 pC vs. TTX + 4-AP, –1.4 ± 0.5 pC; n= 6, p= 0.13) (Petreanu et al., 2009) (**Figure 5A, B**). In addition, the EPSC had a fast a rise time (2.1 ± 0.4 ms), a peak amplitude of 69 ± 7.3 pA and a decay time of 6.7 ± 1 ms (n= 7 cells). These values are similar to those reported for optogenetic stimulation of glutamate release from PC axons in other synaptic targets (Boyd et al., 2012; Russo et al., 2020). Delivery of a high frequency stimulation train (10 Hz LED) produced reliable post synaptic responses in Sst^+ neurons, however the responses showed a strong depression in amplitude (last/first response, 0.12 ± 0.02, n= 5), suggesting that these PC synapses onto MCPO Sst^+ neurons exhibit a high probability of neurotransmitter release (**Figure 5C**). Consistent with this result, low frequency (4 Hz) light stimulation of PC axons drove reliable firing, while higher stimulation frequencies (10 and 25 Hz) increased light-induced spike failure (**Figure 5D**). Last, the evoked EPSCs were completely blocked by the ionotropic glutamate receptor blockers CNQX (10 µM) and D-AP5 (100 µM) (control, –14.7 ± 5 pC vs. CNQX/D-AP5, –1.7 ± 1 pC; n= 5, p=

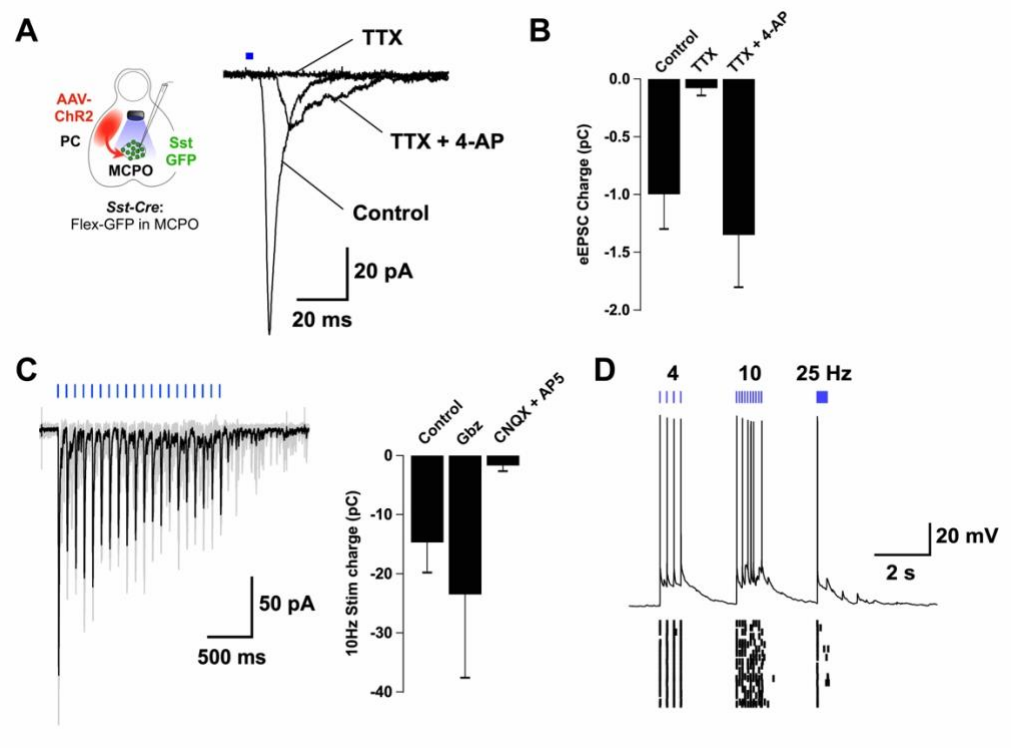

Fig. 5: *Stimulation of PC projections produce direct excitation of Sst GABAergic neurons in the MCPO*

(A) Left diagram, anterograde ChR2 expression was driven in PC neurons using the AAV-ChR2-mCherry virus while GFP was selectively expressed in Sst neurons by injecting the AAV-Flex-eGFP virus in MCPO of the *Sst-Cre* mice. Right, voltage clamp recording in a GFP^+ Sst neuron. At –70 mV, a brief light stimulation (5 ms) elicited large inward currents (control), which were completely abolished by the sodium channel blocker TTX (1 µM). In the additional presence of 4-AP (100 µM) the currents persisted, suggesting the existence of monosynaptic inputs. **(B)** Summary plot for the quantified EPSC charge under the different conditions (n= 6). **(C)** Left, high frequency LED stimulation (blue ticks, 10 Hz) elicited inward currents that rapidly decayed in amplitude, suggesting synaptic depression. Right, summary plot of the charge carried by the eEPSCs under the different conditions (n= 5). The eEPSC was unaffected by application of gabazine but completely blocked by the glutamatergic receptor blockers CNQX and AP5 (10 and 100 µM, respectively) (n= 5). **(D)** Current clamp recording from a Sst neuron showing that light stimulation trains of 4, 10 and 25 Hz evoked reliable depolarization of the cells; however, spike failure increased at higher stimulation frequency consistent with the synaptic depression of the PC to MCPO synapse (n= 5).

0.04), but unaffected by gabazine (control, –14.7 ± 5 pC vs. Gbz –23.5 ± 14 pC; n= 5, p= 0.4) (**Figure 5C**).

Piriform cortex drives excitation of MCPO GABAergic but not cholinergic neurons

GABAergic and cholinergic neurons are present along the BF axis (Záborszky et al., 1986; Zaborszky et al., 2012) and both populations have been shown to regulate olfactory circuits (Nunez-Parra et al., 2013; Rothermel et al., 2014; Liu et al., 2015; Smith et al., 2015; Villar et al., 2021b, 2021a). OB-projecting GABAergic neurons receive direct excitatory inputs from PC but whether cholinergic neurons are also driven directly by PC is unknown. To examine this possibility, we conducted targeted recordings from cholinergic neurons identified by their expression of GFP after injecting the Cre-dependent virus AAV-Flex-eGFP into the BF of *ChAT-Cre* mice. An additional injection was conducted in the PC to enable the expression of ChR2 in PC axons (**Figure 6A**). Surprisingly, unlike the fast EPSC elicited by light stimulation in GABAergic neurons, the same protocol failed to elicit detectable currents in MCPO cholinergic cells (EPSC –0.08 ± 0.06 pC, IPSC 0.1 ± 0.09 pC, n= 9 GFP^+ cells) (**Figure 6B-D**). However, the same stimulus produced large and reliable EPSCs (–3.7 ± 2 pC, n= 5) and IPSCs (7.2 ± 3 pC, n= 5) in nearby non-cholinergic cells (GFP^-) (**Figure 6C, D**). Likely, the evoked IPSC in non-cholinergic neurons was produced by disynaptic feedforward inhibition driven by PC excitatory inputs onto the local GABAergic circuit. Accordingly, the current onset for the IPSCs was significantly slower compared to EPSCs in non-cholinergic cells (IPSC onset 7.7 ± 0.6 ms vs. EPSC 4.8 ± 0.2 ms, n= 4 cells, p< 0.001).

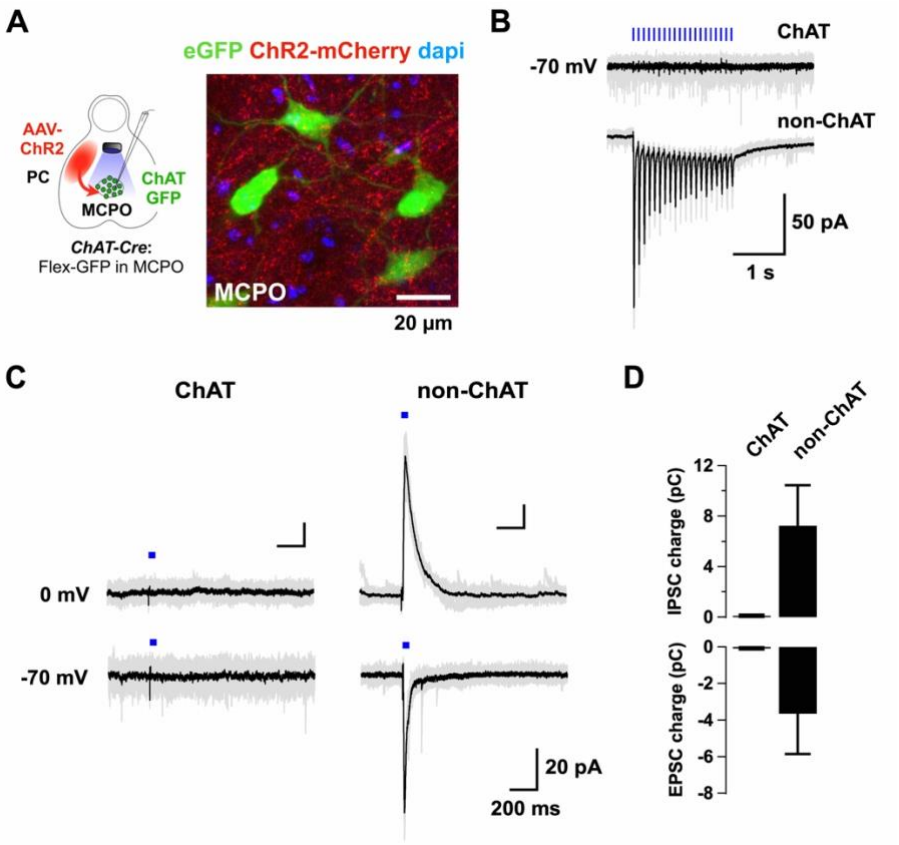

Fig. 6: *Stimulation of PC projections does not produce responses in cholinergic neurons in the MCPO*

(A) Left diagram, anterograde ChR2 expression was driven in PC neurons using the AAV-ChR2-mCherry virus and the labeling of cholinergic neurons with the Cre-dependent AAV-Flex-eGFP virus injected in the BF of *ChAT-Cre* mice. Right, confocal image of the HDB/MCPO showing ChAT cells expressing GFP and the presence of abundant PC axons (red) expressing ChR2-mCherry. **(B)** Targeted whole cell recordings were performed in coronal BF containing slices from GFP^+ and GFP^- cells. High frequency light stimulation (blue ticks, 10 Hz) reliably evoked excitatory currents recorded in GFP^- neurons (bottom), but responses were absent in GFP^+ neurons (cholinergic cells, top). The internal solution was Cs-gluconate based and the holding potential was –70 mV. **(C)** Voltage clamp recordings from GFP^+ (cholinergic, left) and GFP^- cells in the BF. A brief light stimulation pulse (5 ms) evoked large IPSC (top) and EPSC (bottom) in GFP^- cells (right traces) but failed to evoke any detectable current in cholinergic neurons (left traces). (**D**) Bar graphs showing the transferred charge for the light evoked IPSC (top) and EPSC (bottom) in cholinergic (n= 9) and GFP^- cells (n= 5).

Discussion

Our results provide anatomical and functional evidence for the existence of at least three populations of GABAergic neurons in the MCPO, two of which project to the bulb, Sst and Cr, with biases in their synaptic targets. We show fast and cell type specific glutamatergic inputs from the PC onto MCPO neurons; fast excitatory responses were present in Sst neurons but are absent in the nearby Cr and cholinergic neurons. We propose that this specialized PC-MCPO pathway is recruited upon odor encounter and provides a fast GABAergic feedback input to the OB that regulates ongoing odor-induced activity.

Using brain-wide viral tracing we found that both the BF and AON represent the main sources of extrinsic GABAergic inhibition in the OB, accounting for ~85% of all OB-projecting GABAergic neurons in the brain. A recent study indicated that OB projecting AON GABAergic neurons target both local GABAergic neurons as well as M/TCs (Mazo et al., 2020). These results contrast with the specificity for local interneurons previously reported by others for MCPO GABAergic neurons (Gracia-Llanes et al., 2010; Nunez-Parra et al., 2013; Sanz Diez et al., 2019; Hanson et al., 2020; Villar et al., 2021a). Furthermore, while activation of the AON GABAergic input to the OB reduces the activity of MCs (Mazo et al., 2020), the MCPO GABAergic feedback disinhibits the firing of MCs, as expected by their action on the local GABAergic neurons (Villar et al., 2021a). This different effect on MC activity suggests a different role for these parallel channels of inhibitory feedback to the OB. Nevertheless, given the greater number of OB-projecting GABAergic neurons in the MCPO, we hypothesize that they are uniquely positioned to provide a positive top-down feedback signal to the OB that counters the extensive overall

negative feedback exerted by the excitatory input from olfactory cortices (Balu et al., 2007; Boyd et al., 2012; Markopoulos et al., 2012; Oswald and Urban, 2012). In this scenario, odor-driven activation of PC produces excitation of the MCPO GABAergic neurons that opposes the predominantly suppressive effect of the corticofugal feedback on the OB output neurons by balancing the activity of local GABAergic neurons through feedforward long-range inhibition.

We identified two GABAergic populations in the MCPO with differential projections patterns to the OB, Sst and Cr expressing neurons. Sst expressing neurons preferentially innervate the superficial (glomerular) layer of the OB, while Cr expressing axons are denser in deeper (inframitral) layers. Functionally, the glomerular and inframitral circuits engage in different neuronal computations (Shepherd, 2004; Lledo et al., 2005). Glomerular GABAergic circuits provide a mechanism for sensory gain control and decorrelation of odor representations (Wilson and Mainen, 2006; Zhu et al., 2013a; Banerjee et al., 2015), while inframitral circuits modulate the temporal and spatial output of MCs and TCs through recurrent and lateral inhibition (Yokoi et al., 1995; Isaacson and Strowbridge, 1998; Christie et al., 2001; Shepherd, 2004). The existence of at least two MCPO GABAergic output channels could provide layer specific control of gain and output dynamics to circuits that process early olfactory signals. We hypothesize this anatomical arrangement can support parallel top-down pathways, allowing integration of spatially and temporally diverse inputs in the MCPO thus facilitating feedback flexibility. Intriguingly, we found that PV neurons in the MCPO do not exhibit projections to the OB. Instead, previous studies have reported the presence of PV containing neurons in BF GABAergic projections to other brain targets including neocortex and hippocampus (Freund and Antal,

1988; Freund and Gulyás, 1991; Gulyás et al., 1991; Freund and Meskenaite, 1992; Gritti et al., 2003; Henny and Jones, 2008; Korotkova et al., 2010; Brown and McKenna, 2015). This anatomical distinction suggests that the BF GABAergic neurons may influence neocortical circuits separately from outputs directed to paleocortical areas, as the olfactory regions. Future experiments will examine the projection pattern of the MCPO GABAergic subtypes to other brain regions, including olfactory cortices.

Interestingly, we demonstrate the existence of a monosynaptic excitatory pathway from the PC to MCPO Sst neurons while it is absent in cholinergic cells. Our results are consistent with an electron microscopy examination of input projections to the BF showing the absence of cortical innervation to cholinergic cells (Zaborszky et al., 1997). This highly specific synaptic organization suggests that cortical inputs from PC can recruit BF GABAergic neurons independent from the nearby cholinergic cells. Although to date we lack information about the odor-evoked dynamics of acetylcholine release in the OB, our results suggest that likely cholinergic and GABAergic BF feedback projections to the OB act in different temporal domains. We hypothesize that the MCPO Sst feedback pathway is rapidly recruited by odors, while the cholinergic, and possibly Cr, projections are recruited by activation of downstream neuromodulatory areas as the ventral tegmental area, amygdala and nucleus accumbens (Zaborszky et al., 2012), thus conveying context dependent information to the OB. Consistent with this idea, recent studies showed that BF cholinergic neurons are recruited during reward-seeking behaviors and its activity is modulated by the stimulus contingency (Sturgill et al., 2020; Hanson et al., 2021).

Parallel inhibitory streams have been previously reported in other brain regions (Melzer and Monyer, 2020). GABAergic projections from medial septum (MS) to

hippocampus originate from PV^+ and calbindin (CB^+) neurons (Smith et al., 1994; Unal et al., 2015), where PV^+ projections preferentially innervate GABAergic targets in dentate gyrus, CA3 and CA1, while MS CB^+ neurons are biased towards CA1 neurons (Melzer and Monyer, 2020). The differential innervation of hippocampal targets by MS GABAergic neurons has been proposed to act with different temporal dynamics, thus independently regulating the oscillation phase preference in the target interneuron types (Borhegyi et al., 2004; Somogyi et al., 2014; Unal et al., 2015). Similarly, MS projections to the medial entorhinal cortex (MEC) originating from PV^+ and CB^+ target distinct GABAergic neurons in MEC layer 2, yet the role of this differential long-range modulation of MEC circuits by the BF remains unclear (Fuchs et al., 2016).

In sum, our findings on the diversity and connectivity pattern of the BF GABAergic output to the OB and its selective activation by the PC output reveals a complex mechanism by which top-down BF neuromodulatory systems are recruited to influence ongoing odor processing. Future experiments will examine how these systems are influenced by odor-driven behaviors performed under different contexts.

Chapter 5

Concluding remarks

How higher-order feedback signals modulate the coding of incoming sensory inputs to shape perception and ultimately behavior, remains as an open question in Neuroscience. To date, a substantial body of literature describes how sensory cues are transduced by sensory organs and transformed by feedforward neural pathways to support the emergence of a given percept or behavior. However, further research exploring the underlying logic of the interplay between feedforward and top-down flow of information in a behavioral context will be required to ultimately understand the nature of sensory perception. In this dissertation, using mammalian olfaction as a model system, we investigated how top-down GABAergic inhibition from the basal forebrain (BF) shapes early sensory processing.

In Chapter 2, we showed that descending BF GABAergic inputs fine tune the activity of the bulb output neurons by influencing the local GABAergic network. Top-down MCPO GABAergic projections target exclusively local inhibitory neurons in the OB. These synapses are characterized by a phasic and synchronized release of GABA with a slower relaxation time compared to that of local inhibition, indicating a longer temporal influence on target neurons. Furthermore, activation of MCPO GABAergic inputs produced inhibitory currents capable of a strong control of the membrane potential in the target neurons. At the circuit level, activation of MCPO top-down projections produced an overall disinhibition of MCs due to a significant reduction of the amount of dendrodendritic interactions of MCs with the local inhibitory neurons. This circuit effect is sufficient to

modulate the spike precision of MCs and regulate the intensity of electrically induced oscillations in a layer-specific manner in the OB.

In Chapter 3, we characterized how the activity of the BF GABAergic feedback is modulated by odor stimuli, as a function of odor identity and concentration, in behaving mice. First, we demonstrated that OB projecting BF GABAergic neurons receive fast glutamatergic inputs from the piriform cortex (PC), supporting the existence of fast GABAergic feedback to the OB, modulated by odor-driven activation of the PC. Accordingly, odor presentation evoked an enhancement or suppression of calcium signals, used as a proxy of activity in GABAergic axonal boutons imaged in the OB. These two types of response modes are largely stable across orders of magnitude of odor concentration. The response dynamics of these boutons are tightly coupled to the odor timing and are characterized by a fast onset, followed by a rapid decay. The temporal features of odor-evoked responses in the GABAergic boutons are comparable to those in the fast excitatory feedback from PC to the OB, imaged under similar conditions. Since the glutamatergic and GABAergic feedbacks share the same postsynaptic targets in the OB, these results indicate that both feedbacks can act synergically to rapidly balance the neural output of the OB. Intriguingly, pure odors trigger sparse activation of GABAergic boutons, and they do so in an odor specific manner, suggesting a high degree of specificity in the activation of BF GABAergic neurons by olfactory stimulation. Furthermore, odor responses in GABAergic boutons imaged in the glomerular layer, where the peripheral sensory inputs arrive, show higher similarity than odor responses in infraglomerular layers, suggesting that the GABAergic feedback provide the bulb with layer specific inputs which could differentially modulate the distinct functional circuit domains of the OB.

In Chapter 4, we further defined the neural components and functional role of the excitatory PC pathway that recruits OB projecting BF GABAergic neurons. We demonstrated the existence of a subset of excitatory projections from the PC that target exclusively GABAergic neurons; these cortical inputs avoid the nearby cholinergic neurons, also located in the BF. These results indicate a high degree of circuit specialization that could produce a differential control of two critically important sources of neuromodulatory inputs to the bulb. Furthermore, the BF GABAergic feedback to the OB consists of at least two non-overlapping populations of inhibitory neurons, distinguished by their expression of the cellular markers somatostatin (Sst) and calretinin (Cr). Interestingly, while both populations establish functional synapses with the local inhibitory network, Sst and Cr neurons differentially target the functional circuit domains of the OB, providing an anatomical substrate for a parallel top-down control of early olfactory processing.

Together, the work described in Chapters 2, 3 and 4 of this dissertation provides a physiological framework by which the BF GABAergic feedback can influence the processing dynamics of incoming odor information in the OB. Our results represent a starting point in understanding how fast neuromodulation influences ongoing olfactory processing, thus multiple facets remain unexplored and shall be subject of further investigation.

Future directions

Determine how BF GABAergic feedback influences odor responses of the OB output neurons.

Activation of the BF GABAergic feedback disinhibits MCs, reduces their spike precision, and modulates the intensity of neural oscillations in the OB. Yet, how these circuit-mediated effects result in changes in odor representation by MC and TCs remains unknown. The use of optogenetic methods to transiently silence (e.g., NpHR3.0 or JAWS) the activity of the BF GABAergic feedback to the OB, combined with multiphoton calcium imaging of MCs and TCs or electrophysiological recordings in the awake mouse, will be necessary to systematically characterize odor responses in the output neurons, in the absence of the MCPO GABAergic feedback projections. Imaging the activity of large ensembles of MCs and TCs using fast-scanning multiphoton microscopy will allow study changes in odor-response correlation of populations of MC and TCs when manipulating the GABAergic feedback. We do not know whether these two types of output neurons of the OB, which have biased projections to the PC and AON (Fukunaga et al., 2012; Igarashi et al., 2012), will be regulated similarly by the feedback inhibition. In addition, *in vivo* electrophysiological recordings will allow study subtle modulations of sniff phase coupling of the activity of the output neurons by the BF GABAergic feedback. We hypothesize that a reduction in the activity of the OB inhibitory feedback will favor the recruitment of the local inhibitory circuit driven by odor stimulation and therefore increase decorrelation of MCs compared with the no stimulation condition, thus favoring odor discrimination.

Furthermore, since the trial-to-trial timing precision of MCs depends on local inhibition, we hypothesize that suppressing the activity of the OB GABAergic feedback will increase MCs precision compared with the no stimulation condition.

Monitor the activity of BF GABAergic feedback during rapid odor discriminations

Odor encounters result in fast, sparse and odor specific responses across the BF GABAergic boutons in the OB. Yet, the activity dynamics of the GABAergic feedback boutons in response to motivated and attentive behavior in mice remains unexplored. To determine how these feedback signals support behavioral flexibility, future experiments shall monitor GABAergic top-down projections in the OB of mice performing rapid odor discriminations. These studies should consider simultaneous multiphoton imaging of boutons in the BF GABAergic and cortico-bulbar glutamatergic feedback projections to the OB to examine the interplay of two fast top-down feedbacks able to transiently change the output polarity of the OB. Simultaneous imaging of excitatory and inhibitory feedback axons in a single field of view can be achieved with dual expression of GCaMP and a red-tag protein (mRuby) in one type of feedback, while only GCaMP in the other. Expressing the same calcium sensor in both axonal feedbacks, rather than different sensors (e.g., GCaMP vs. jRGECO), will facilitate direct comparisons between their response dynamics. We hypothesize a higher recruitment of the MCPO GABAergic feedback in mice engaged in a behavioral task, due to extensive interactions of the GABAergic and cholinergic systems in the BF. Furthermore, other neuromodulatory systems known to innervate the

BF, as the noradrenergic and dopaminergic systems, likely play a role in modulating the activity of the MCPO GABAergic feedback during active olfactory behavior.

Determine how inputs from the PC to the BF modulate odor discrimination

BF GABAergic neurons integrate fast glutamatergic inputs from the PC. However, whether this pathway is recruited during active odor discrimination and is necessary for olfactory function remains unknown. Future experiments shall examine the importance of this descending cortical pathway to the BF by optogenetically suppressing it (NpHR3.0 or JAWS) in mice engaged in an olfactory discrimination task. Since glutamatergic inputs from PC to BF do not target cholinergic neurons, silencing PC axons in the MCPO is expected to only affect the input to the GABAergic population. Light stimulation of PC axons in the MCPO can be achieved by implanting a thin optical fiber into the target region, while freely behaving animals perform an olfactory task. We hypothesize that inhibiting the input from the PC to the MCPO will extensively reduce the recruitment of the OB projecting GABAergic neurons. This will likely alter the excitation to inhibition balance across the OB circuits and degrade the performance of mice engaged in an olfactory task.

Appendix A

Cholinergic modulation of distinct inhibitory domains in granule cells of the olfactory bulb

Citation

Villar PS, Hu R, Teitz B and Araneda RC (2021). Cholinergic modulation of distinct inhibitory domains in granule cells of the olfactory bulb. BioRxiv. doi.org/10.1101/2021.10.15.464603.

Author contributions

P.S.V, R.H and R.C.A designed research; P.S.V, R.H and B.T performed research; P.S.V, R.H and B.T analyzed data; P.S.V and R.C.A wrote the paper.

Acknowledgments

We thank Drs. Rodrigo Andrade and Richard S. Smith for helpful comments on this manuscript and Mr. Eric Segev for assistance with the laser uncaging software. This research was supported by the National Institute on Deafness and Other Communication Disorders, grant DCR01-DC-009817 and National Institute on Aging, grant AG-049937A of the National Institute of Health to Dr. Ricardo C. Araneda and National Science Foundation-Graduate Research Fellowships Program/Division of Graduate Education, grant 1322106 to Dr. Ruilong Hu.

Summary

Early olfactory processing relies on a large population of inhibitory neurons in the olfactory bulb (OB), the granule cells (GCs). GCs inhibit the OB output neurons, the mitral and tufted cells (M/TCs), shaping their responses to odors both in the spatial and temporal domains, therefore, the activity of GCs is finely tuned by local and centrifugal excitatory and inhibitory inputs. While the circuit substrates underlying regulatory inputs onto GCs are well-established, how they are locally modulated remains unclear. Here, we examine the regulation of GABAergic inhibition onto GCs by acetylcholine, a main neuromodulatory transmitter released in the OB, by basal forebrain (BF) neurons. In acute brain slices from male and female mice, we show that activation of muscarinic acetylcholine receptors (mAChRs) produces opposing effects on local and centrifugal inhibition onto GCs. By using electrophysiology, laser uncaging and optogenetics we show that the kinetics of GABAergic currents in GCs could be correlated with distal and proximal spatial domains from where they originate, along the GC somatodendritic axis. Proximal inhibition from BF afferents, is suppressed by activation of M2/M4-mAChRs. In contrast, distal local inhibition from deep short axon cells (dSACs) is enhanced by activation of M3-mAChRs. Furthermore, we show that the cholinergic enhancement of distal inhibition in GCs reduces the extent of dendrodendritic inhibition in MCs. Interestingly, the excitatory cortical feedback, which also targets the proximal region of GCs, was not modulated by acetylcholine, suggesting that muscarinic activation shifts the synaptic balance towards excitation in GCs. Together, these results suggest that BF

cholinergic inputs to the OB fine tune GC-mediated inhibition of M/TCs by differentially modulating the proximal and distal domains of inhibition in GCs.

Introduction

GABAergic inhibition has a crucial role in shaping sensory processing, precisely regulating both temporal and spatial aspects of signal processing in sensory circuits (Isaacson and Scanziani, 2011; Wood et al., 2017; Cardin, 2018). Inhibition by GABAergic granule cells (GCs) is a prominent physiological mechanism in the olfactory bulb (OB), the first brain region where odor processing occurs (Price and Powell, 1970a; Shepherd, 2004; Abraham et al., 2010; Li et al., 2018). GCs synapse onto mitral and tufted cells (M/TCs), the output neurons of the OB, and the GC function is finely regulated by local and top-down signals (Price and Powell, 1970b; Yokoi et al., 1995; Isaacson and Strowbridge, 1998; Schoppa, 1998; Christie et al., 2001; Shepherd, 2004; Matsutani and Yamamoto, 2008). Among these regulatory signals, both glutamatergic feedback from the olfactory cortices and cholinergic inputs from the BF have been shown to influence odor processing by modulating GCs excitability, in the latter case with a predominant contribution of muscarinic acetylcholine receptors (mAChRs) (Castillo et al., 1999; Ghatpande et al., 2006; Pressler et al., 2007b; Smith et al., 2015). Furthermore, the excitatory feedback to GCs is regulated by local GABA release (Mazo et al., 2016); however, less is known about the regulation of GABAergic inhibition of GCs.

GCs receive inhibitory inputs from local deep short-axon cells (dSACs) (Pressler and Strowbridge, 2006; Eyre et al., 2008; Burton and Urban, 2015) and from long-range

GABAergic neurons (LRGNs) of the BF (Gracia-Llanes et al., 2010; Nunez-Parra et al., 2013; Sanz Diez et al., 2019; Böhm et al., 2020; Hanson et al., 2020; Villar et al., 2021a). Interestingly, these two sources of inhibition appear to be segregated along the proximal-distal axis of GCs, suggesting they could differentially regulate GC function. Inputs from dSACs provide distal, and to a lesser extent proximal, feedforward inhibition to GCs (Eyre et al., 2008; Burton and Urban, 2015), while BF-LRGNs densely innervate deeper layers of the OB, where the somas of GCs are localized, suggesting a predominant perisomatic influence in GCs (Gracia-Llanes et al., 2010; Villar et al., 2021a). Furthermore, through dendrodendritic synapses with the M/TCs at their distal dendrites, GCs engage in two types of inhibitory mechanisms to regulate M/TCs activity: localized recurrent inhibition (Isaacson and Strowbridge, 1998; Mori et al., 1999; Egger et al., 2003; Shepherd, 2004), and lateral inhibition, which involves widespread activation of the distal dendrite and the inhibition of several neighboring M/TCs. Thus, proximal vs. distal regulation of GC excitability is expected to have a different influence in tuning recurrent and lateral inhibition, with global excitation of GC dendrites having a larger impact on overall inhibition on M/TCs.

Here, we examined the regulation of inhibition to GCs by acetylcholine (ACh). By using electrophysiology, laser uncaging and optogenetics we show that proximal and distal anatomical domains of inhibition can be distinguished in GCs, based on the waveforms of inhibitory currents onto GCs. Events originating in distal regions of the GC's dendrites corresponded to inputs from dSACs. Accordingly, depolarization of dSACs by activation of M3-mAChRs produced a robust increase in the occurrence of distal sIPSCs. Importantly, the increase in distal inhibition onto GCs decreased recurrent inhibition in mitral cells

(MCs). In contrast, inhibitory inputs from the BF, targeting the proximity of the soma, were strongly suppressed by activation of M2-mAChRs. Interestingly, the excitatory feedback from the piriform cortex (PC), which similar to LRGNs targets the somatic region of GCs, was not affected by ACh, suggesting that at the somatic level, ACh promotes excitation of GCs. Together, these results suggest that topologically distinct sources of inhibition of GCs are differentially modulated by ACh through the activation of muscarinic receptors, which we propose will facilitate global excitation of GC, while enhancing inhibition onto distal dendritic compartments.

Methods

Animals. All experiments were conducted following the US National Institute of Health guidelines and approved by the Institutional Animal Care and Use Committee of the University of Maryland, College Park. Electrophysiological experiments were performed on adult C57BL/6 (JAX, stock #664), *Gad2-IRES-Cre* mice (JAX, stock #010802), *Thy1-EYFP-ChR2* (JAX, stock #007612) and *ChAT-tau GFP* (generously provided by Dr. Sukumar Vijayaraghavan, University of Colorado, School of Medicine) female and male mice, ranging in age from one to four months, obtained from breeding pairs housed in our animal facility.

Stereotaxic injections. Anesthesia was induced with 2% isoflurane at a rate of 1 L/min and adjusted over the course of the surgery. Body temperature was maintained using a heating pad. Carprofen (intraperitoneal, 5 mg/Kg) was used as analgesic and Betadine as

antiseptic. During the surgery, the eyes were lubricated using a petrolatum ophthalmic ointment (Paralube). To express ChR2 in LRGNs, *Gad2-Cre* mice received a stereotaxic injection (200 nL) of the AAV5-CAG-Flex-ChR2-tdTomato adenovirus (Catalog #18917, Addgene) into the MCPO, using the following stereotaxic coordinates (in mm): D/V –5.4, M/L ± 1.63, A/P +0.14. Alternatively, to visualize the innervation of BF-LRGNs across the OB layers, the anterograde tracer AAV5-CAG-Flex-eGFP-WPRE (Catalog #51502, Addgene) was injected into the MCPO as detailed above. For anterograde expression of ChR2 in the cortical feedback projections, C57BL/6 mice were injected with the AAV5-CAG-ChR2-mCherry adenovirus (200 nL, Addgene) in the PC, using the following stereotaxic coordinates (in mm): D/V –3.5, M/L ± 2.8 and A/P 1.6. After surgery, animals were left to recover, and electrophysiological recordings or histological experiments were conducted at 3 weeks or later.

Histology. Mice were transcardially perfused with cold 4% PFA prepared in 0.1 M phosphate buffer saline (PBS) at pH 7.4. Brains were then harvested and post fixed overnight (ON) at 4°C in the same fixative solution. The brain was sliced horizontally in sections of 50-100 μm, nuclei were stained with DAPI (Catalog #D1306, Invitrogen) and mounted in a solution of Mowiol-DABCO. The mowiol mounting media contained 9.6% w/v mowiol (Catalog #475904, Millipore), glycerol 24% w/v, 0.2 M Tris (pH 6.8), 2.5% w/v DABCO (used as antifade reagent, Catalog #D2522, Sigma) and Milli-Q water. BF cholinergic axons were visualized using the *ChAT-tau GFP* mouse line, in which the intrinsic eGFP expression was amplified by immunohistochemistry. Briefly, free floating brain slices of 50-100 μm were blocked with donkey serum (10%, Catalog #S30-M,

Millipore) in PBS supplemented with Triton X-100 (0.1% v/v, Catalog #T8787, Millipore, PBS-T) for 1 h at room temperature (RT). Sections were then incubated ON at RT with a rabbit anti-GFP primary antibody (1:500, Catalog #598, MBL) and 2.5% donkey serum in PBS-T. The primary antibody was washed with PBS-T for at least 30 min before incubation with a donkey anti-rabbit antibody coupled to Alexa fluor-594 for 2 h, at RT (1:500, Catalog #A-21207, Invitrogen). Images were acquired using a Leica SP5X confocal microscope and analyzed using ImageJ (NIH) and a custom written MATLAB software (MathWorks).

Whole-cell recordings. Horizontal OB slices (250 µm) were prepared as before (Villar et al., 2021a). Briefly, slices were prepared in oxygenated ice-cold artificial cerebrospinal fluid (ACSF) containing low Ca^{2+} (0.5 mM) and high Mg^{2+} (3 mM). Sections were then transferred to an incubation chamber containing normal ACSF (see below) and left to recover for at least 30 min at 35°C, before the recordings. In all experiments the extracellular solution is ACSF of the following composition (in mM): 125 NaCl, 26 $NaHCO_3$, 1.25 NaH_2PO_4, 2.5 KCl, 2 $CaCl_2$, 1 $MgCl_2$, 1 myo-inositol, 0.4 ascorbic acid, 2 Na-pyruvate, and 15 glucose, continuously oxygenated (95% O_2, 5% CO_2) to give a pH 7.4. Neurons were visualized with an Olympus BX51W1 microscope using a 40x water immersion objective (LUMPlanFI/IR, Olympus) and recorded using a dual EPC10 amplifier interfaced with the PatchMaster software (HEKA, Harvard Bioscience). Whole-cell recordings were performed at RT. Patch pipettes were made of thick wall borosilicate glass capillaries (Sutter instruments, 3-6 MΩ resistance) using a horizontal pipette puller (P-97, Sutter Instrument). Spontaneous inhibitory postsynaptic currents (sIPSCs) were

recorded with pipettes filled with an internal solution of the following composition (in mM): 125 Cs-gluconate, 4 NaCl, 10 HEPES-K, 10 Na phosphocreatine, 2 Na-ATP, 4 Mg-ATP, and 0.3 GTP. Alternatively, the sIPSCs were recorded at −70 mV using an internal solution of the following composition (in mM): 150 CsCl, 4.6 $MgCl_2$, 0.1 $CaCl_2$, 10 HEPES, 0.2 EGTA, 4 Na-ATP, 0.4 Na-GTP and 5 QX-314. The final pH of the internal solution was adjusted to 7.3 with CsOH. The measured osmolarity was ~290 mOsm. For current clamp recordings, the internal solution had the following composition (in mM): 120 K-gluconate, 10 Na-gluconate, 4 KCl, 10 HEPES-K, 10 Na phosphocreatine, 2 Na-ATP, 4 Mg-ATP, and 0.3 GTP adjusted to pH 7.3 with KOH. For optogenetic stimulation, a LED lamp (COP1-A, Thor Labs) was used to produce brief pulses (0.5-5 ms) of collimated blue light (473 nm, 1 mW/mm^2) delivered through a 40x water immersion objective.

Single photon GABA uncaging. We performed single-photon GABA uncaging as previously described (Nunez-Parra, et al. 2013). To visualize the morphology of the recorded neurons we included Alexa fluor-594 (20 μM, Invitrogen) in the recording pipette and used custom written ImageJ μManager software to track and aim the uncaging laser spot along the somatodendritic axis of the GC. The recorded sequence of coordinates was interpolated and recreated by discretized movements of a motorized stage from the proximal to distal coordinates (in ~ 10 μm steps). Similar results were obtained when the uncaging sequence was reversed to start at the most distal coordinate instead. The collimated output of a 405 nm laser (Coherent, LLC) was expanded to 60% of the back aperture of a 60x Olympus objective. The spot has a Gaussian profile in the focal plane

with a $1/e^2$ radius= 0.87 μm. Fluorescence illumination was achieved using a green LED (exciter 594 nm center wavelength) (Chroma), and the emitted light was collected by a CCD camera (Hamamatsu). The concentration of DPNI-GABA was 2 mM (Tocris). Laser flashes were of 100 μs duration with power intensities at the surface of the slice up to 2 $mW/\mu m^2$.

Data analysis. Electrophysiological recordings were analyzed in MATLAB (MathWorks) and Igor Pro (WaveMetrics). Synaptic currents were detected and analyzed with a custom written script in MATLAB. Rise time was calculated as the time from 10% to 90% of the current peak. The decay time was measured by fitting a double exponential decay function to the current relaxation and computing the weighted time constant (τ_w) as $\tau_w = (a_1\tau_1 + a_2\tau_2)/(a_1 + a_2)$, where a and τ are the amplitude and time constant of the first (1) and second (2) exponentials, respectively. The IPSC waveforms from all cells were used to cluster the GABAergic events using the k-means clustering function in MATLAB. To determine the number of clusters we calculated the average distance from each point to every centroid (*d*-value), while varying the number of clusters from 1 to 10. The *d*-value was plotted against the number of clusters used for clustering, and the cutoff for the number of clusters was obtained when *d*-value plateaued (Otazu et al., 2015) (**Figure 2-1B**).

Data is shown as the mean ± S.E.M, unless otherwise specified. Statistical significance was determined by student's t-test or Wilcoxon rank sum (*= $p<0.05$, **= $p<0.01$, ***= $p<0.001$).

Pharmacological agents. Drugs were prepared from stocks stored at –20°C, diluted into ACSF and perfused at a speed of ~2 mL/min; acetylcholine chloride (Catalog # A6625, Sigma), muscarine iodide (Catalog #3074, Tocris), oxotremorine (Catalog #1067, Tocris) 4-DAMP (Catalog #0482, Tocris), AFDX-384 (Catalog #1345, Tocris), pirenzepine dihydrochloride (Catalog #1071, Tocris), atropine (Catalog #A0132, Sigma), nicotine ditartrate (Catalog # 3546, Tocris), PNU-120596 (Catalog #2498, Tocris), 6-cyano-7-nitroquinoxaline-2,3-dione (CNQX disodium salt, Catalog #1045, Tocris), (R)-Baclofen (Catalog #0796, Tocris).

Results

Muscarinic ACh receptor activation increases inhibitory activity in GCs

The BF GABAergic and cholinergic projections to the OB exhibit a considerable overlap in most layers, especially in the GC and periglomerular layers where abundant synaptic boutons can be observed (**Figure 1A**, insets) (mean normalized pixel intensity ± SD, Gad2 MCPO axons: GL 0.3 ± 0.1, EPL 0.3 ± 0.1, GCL 0.6 ± 0.1, n= 14 slices, 3 mice; ChAT BF axons: GL 0.7 ± 0.2, EPL 0.5 ± 0.1, GCL 0.5 ± 0.1, n= 22 slices, 4 mice). The extent of overlap of these systems suggests that as in other brain regions, ACh can modulate GABAergic inhibition in GCs. To examine this possibility, we bath perfused ACh (100 μM) while recording sIPSCs in GCs (**Figure 1B**). We found that in 50% of the GCs recorded (9/18), ACh strongly increased the frequency of inhibitory events (control 1.1 ±

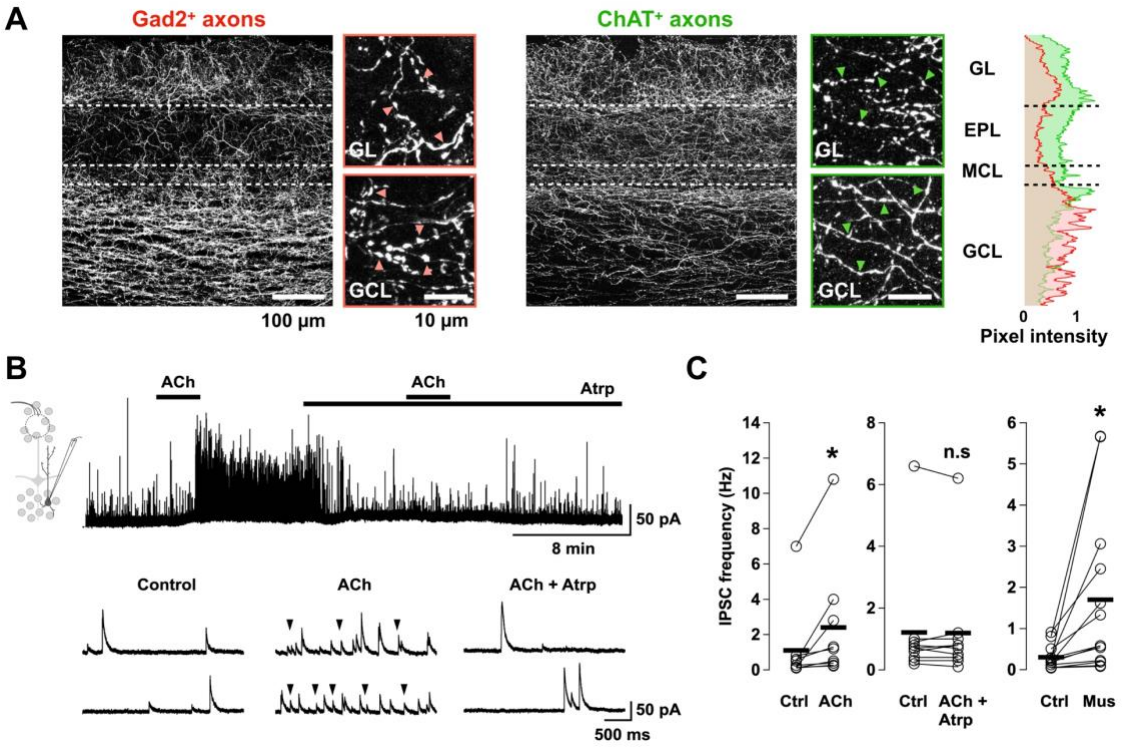

Fig. 1: *Acetylcholine enhances inhibitory currents in granule cells via muscarinic activation*

(A) Left, horizontal section of the OB of a *Gad2-cre* mouse containing axons from MCPO LRGN expressing eGFP. Right, horizontal section of the OB of a *ChAT-tau GFP* mouse. The panels on the right of each image are magnifications of the GL and GCL showing the presence of abundant axonal boutons (arrowheads) in the GABAergic and cholinergic axons, across the superficial and deeper layers of the OB. Right, quantification of peak normalized pixel intensity distributions for the GABAergic (red) and cholinergic (green) axonal projections shown on the left. There is an extensive colocalization of cholinergic and GABAergic axons, especially in the superficial and deeper layers of the OB. **(B)** Top, spontaneous IPSCs (sIPSCs) were recorded at 0 mV in GCs. In this cell, the basal rate of inhibitory currents was 0.48 Hz. Application of acetylcholine (ACh, 100 µM) produced a large increase in the frequency of sIPSCs (4 Hz), which was prevented by the application of the muscarinic receptor blocker atropine (Atrp, 3 µM, 0.46 Hz). Bottom, selected traces in an expanded time scale, before and after the drugs application shown in the top trace. Arrowheads indicate the increase in frequency of small amplitude events. **(C)** Summary of the effect of ACh and muscarine (Mus, 10 µM) on the sIPSC frequency in GCs; ACh significantly increased the frequency of sIPSC in GCs (n= 9, p= 0.04), and this effect was blocked by Atrp (n= 10, p= 0.82). Similarly, Mus significantly increased the sIPSC frequency in GCs (n= 13, p= 0.02).

0.7 Hz vs. ACh 2.4 ± 1.1 Hz, n= 9, p= 0.04) (**Figure 1C**), especially sIPSCs of smaller amplitude (**Figure 1B**, arrowheads). The effect of ACh on GCs was completely abolished in the presence of atropine (Atrp, 3 μM), a broad muscarinic receptor blocker (control 1.2 ± 0.6 vs. ACh in Atrp 1.2 ± 0.5 Hz, n= 10, p= 0.82) (**Figure 1B, C**), indicating the enhancement of inhibition in GCs results from mAChR activation. Accordingly, the mAChR agonist muscarine (Mus, 10 μM), produced a significant increase in the frequency of sIPSCs in ~50% of the recorded GCs (13/24) (control 0.3 ± 0.08 Hz vs. Mus 1.7 ± 0.55 Hz, n= 13, p= 0.02) (**Figure 1C**). As with ACh, the increase in event frequency produced by Mus was accompanied by a small reduction in the mean amplitude of the overall population of sIPSCs (control 19.6 ± 0.4 pA vs. Mus 17.3 ± 0.3 pA, n= 13 cells, p< 0.001) (**Figure 2-1A**).

In the non-responding GCs, neither ACh nor Mus produced a change in the frequency or the amplitude of the sIPSCs (data not shown). The lack of muscarinic effect in these GCs is unknown, however, both responding and non-responding GCs had a similar basal frequency of sIPSCs (ACh responding 1 ± 0.7 Hz vs. ACh non-responding 0.5 ± 0.1 Hz, p= 0.45; Mus responding 0.3 ± 0.1 Hz vs. Mus non-responding 0.5 ± 0.2 Hz, p= 0.3), arguing against the possibility the non-responding neurons correspond to unhealthy GCs.

Muscarinic ACh receptor activation enhances distal inhibition of GCs

In the presence of mAChR activation small amplitude events were more prominent, therefore, we examined the possibility that Mus enhanced a selective population of

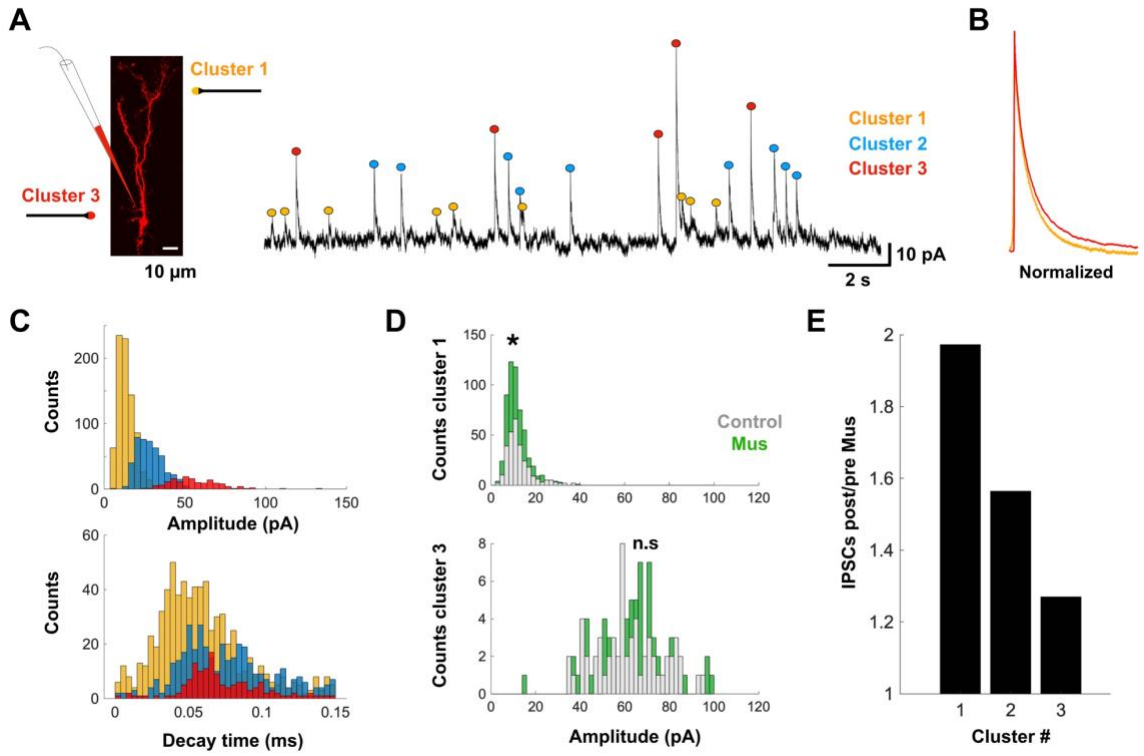

Fig. 2: *Differential enhancement of inhibitory currents in granule cells by muscarinic AChR activation*

(A) Left, confocal image of a GC filled with Alexa fluor-594 during the whole-cell recording highlighting the presence of intact dendritic processes. Right, sample trace of spontaneous inhibitory postsynaptic currents (sIPSCs) recorded in a representative GC. Recordings were conducted in voltage clamp at 0 mV, using a Cs-gluconate based internal solution. sIPSC waveforms were clustered into three populations using the k-means method. The colored markers on top of each sIPSC indicate the assigned cluster (yellow, cluster 1; blue, cluster 2; red, cluster 3). **(B)** Overlay of normalized waveforms (to the peak current) for clusters 1 and 3 which exhibit different rise time kinetics. **(C)** Histograms of sIPSC amplitude (top) and decay time (bottom) for each cluster. **(D)** Effect of Mus on events classified as belonging to clusters 1 and 3 (1420 events); the sIPSC amplitude histograms for each cluster are shown, before (light gray) and after the application of Mus (green). Mus significantly increased the number of sIPSC in cluster 1 ($p = 0.044$) but not in cluster 3 ($p = 0.72$). **(E)** Summary plot showing the ratio for the occurrence of IPSCs during the application of Mus (post) compared with baseline (pre) (post/pre ratio, cluster 1: 1.97, cluster 2: 1.56, cluster 3: 1.27). The **Figure 2-1** (Appendix B) shows the un-clustered amplitude distribution for sIPSCs in GCs and mean waveforms for each cluster.

spontaneous GABAergic currents in GCs. Under resting conditions, sIPSCs recorded at 0 mV occurred at low frequency (0.24 ± 0.05 Hz, n= 29) (**Figure 2A**) and exhibited a wide range of amplitudes (5-132 pA, mean ± SD: 23 ± 15 pA, 1411 events), with similar variability in rise (1.1-7.6 ms, mean ± SD: 2.5 ± 2 ms) and decay times (21-145 ms, mean ± SD: 69.1 ± 36 ms), possibly reflecting variations in their origin along the somatodendritic axis (Nusser et al., 1999). To explore this possibility, we clustered the current waveforms of isolated sIPSCs using the k-means method, which rendered three distinct populations of events that we termed clusters 1 to 3 (**Figure 2A** and **Figure 2-1B**). These sIPSC populations had differences in their time course and occurred with different relative frequencies (**Figure 2B, C**). Events in cluster 1, characterized by smaller amplitude, slower rise time and faster decay time, were the most abundant (**Figure 2C**, n= 808 events; mean ± SD: amplitude 13.9 ± 6.3 pA, rise time 3.2 ± 2.7 ms, decay time 62.5 ± 35.4 ms). In contrast, events in cluster 3, characterized by larger amplitude, faster rise times and slower decay, occurred less frequently (**Figure 2C**, n= 150 events; mean ± SD: amplitude 55.2 ± 15.8 pA, rise time 1.3 ± 0.3 ms, decay time 74 ± 29.3). Cluster 2 was characterized by events with intermediate amplitude and occurrence (**Figure 2C**, n= 453 events; mean ± SD: amplitude 28.6 ± 8.3 pA, rise time 1.7 ± 1.4 ms, decay time 79.5 ± 36.3 ms). Interestingly, clustering of the sIPSC waveforms showed that the prevalence of large amplitude sIPSCs (cluster 3) was unaffected by Mus (Wilcoxon rank sum, p= 0.72), while the largest proportional increase occurred with the smaller amplitude sIPSCs (cluster 1 and 2, Wilcoxon rank sum; cluster 1, p= 0.044, cluster 2, p= 0.045) (**Figure 2D**). Consistently, the ratio of sIPSCs after bath perfusion of Mus, compared with baseline, was higher for cluster 1 than for cluster 2 and 3 (**Figure 2E**).

Oxotremorine (Oxo, 10 μM), another non-selective mAChR agonist, produced a similar increase in sIPSC frequency in 50% of GCs (events in clusters 1 and 2; control 0.7 ± 0.3 Hz vs. Oxo 1.4 ± 0.4 Hz, p= 0.05, n= 4 out of 8 cells; not shown), without altering the representation for events in cluster 3. In summary, the clustering method described above allows us to distinguish at least two distinct populations of sIPSCs, clusters 1 and 3. We surmise that cluster 1, with smaller amplitude events, corresponds to sIPSCs originating at distal regions of GC, while events comprising cluster 3, with larger amplitudes, originate at proximal sites; activation of mAChRs mostly increases inhibitory currents originating at distal regions of GCs (see also below). Events in cluster 2, likely correspond to an overlap of inputs that mainly target these proximal and distal regions of GCs; therefore, we concentrated our analysis on clusters 1 and 3.

Inputs to GCs from dSACs and BF-LRGNs generate IPSCs with distinct properties

GCs receive inhibitory inputs from dSACs found in the external plexiform layer (EPL-dSAC) that directly synapse onto the distal dendrites of GCs (Eyre et al., 2008), and from LRGNs of the BF, which densely innervate deeper layers in the bulb suggesting a greater influence on the somatic region of GCs (Villar et al., 2021a). We reasoned that events in clusters 1 and 3 correspond to these sources of inhibition to GCs and examined this possibility by selectively activating these inhibitory inputs using optogenetics. We activated dSACs by stimulating M/TCs expressing the light-gated cation channel channelrhodopsin-2 (ChR2), under the *Thy1* promoter (Arenkiel et al., 2007) (**Figure 3A, B**). To isolate the inhibitory input from dSACs we recorded GCs at the reversal potential

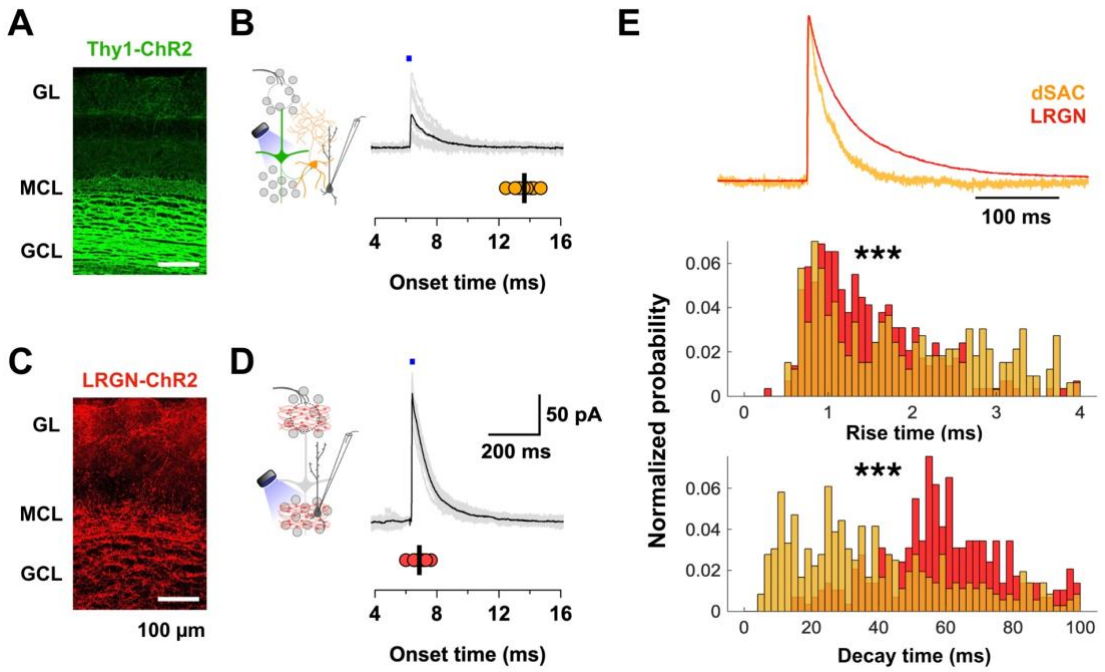

Fig. 3: *Centrifugal and local GABAergic inputs on granule cells exhibit distinct kinetics*

Confocal image of an OB section showing the expression of ChR2-YFP in Thy1^{+} neurons (M/TCs). (B) Left, diagram of the experimental configuration to elicit disynaptic inhibition in GCs; we optogenetically stimulated M/TCs in a *Thy1-EYFP-ChR2* mouse while recording at 0 mV. Right trace, overlay of light-evoked disynaptic IPSCs in a representative GC (gray traces) elicited by feedforward excitation of dSACs, the mean evoked IPSC is shown overlaid in black. Bottom, scatter plot of the onset time for the responses in this GC; the average onset time was 13.7 ± 0.2 ms, consistent with a disynaptic nature. **(C)** Confocal image of an OB section showing abundant axonal labeling from MCPO LRGNs expressing ChR2-tdTomato, in a *Gad2-Cre* mouse. **(D)** Left, diagram of the experimental configuration; we recorded from GCs at 0 mV, eliciting minimal optogenetic stimulation of LRGN axons expressing ChR2 (in red). Right trace, overlay of light evoked IPSCs in a representative GC (gray traces), the mean evoked IPSC is shown overlaid in black. Bottom, scatter plot of the onset times for the responses in the cell above; the average onset time was 7 ± 0.8 ms, consistent with their monosynaptic nature. **(E)** Top, overlay of normalized waveforms (to the peak current) for the dSAC evoked IPSC (yellow) and LRGN evoked IPSC (red) recorded in GCs to illustrate their different decay kinetic. Bottom, probability distribution histograms of rise and decay times for minimally evoked IPSCs with stimulation of BF-LRGNs axons (red; events= 291; n= 10 cells) and the disynaptically evoked IPSC (yellow, events= 451; n= 8 cells). The disynaptic IPSC elicited by dSAC activation exhibits faster decay times, as well as a slightly slower rise times

compared with the LRGN evoked IPSC (dSAC evoked IPSC: decay time 38.89 ± 1.3 ms, rise time 1.9 ± 0.05 m; MCPO evoked IPSC: decay time 59.1 ± 1 ms, rise time 1.5 ± 0.04 ms. Wilcoxon rank sum $p < 0.001$).

of glutamatergic currents (0 mV). Consistent with their disynaptic nature, brief light pulses (0.5-1 ms), reliably evoked IPSCs with slow onset (9 ± 0.2 ms). The evoked IPSCs (n= 451 events, n= 8 cells) had variable amplitude (5-108 pA, mean 23 ± 0.8 pA) and a mean decay of 38.9 ± 1.3 ms (**Figure 3E**).

To selectively activate the BF GABAergic inputs to GCs, we expressed ChR2 in the MCPO of *Gad2-Cre* mice (Villar et al., 2021a). Light activation evoked IPSCs (n= 291 events, 10 cells) of faster onset (7 ± 0.8 ms), larger amplitude (mean 130 ± 5.5 pA), and slower decay (mean 59.1 ± 1 ms), compared to those evoked by dSACs activation. As shown in Figure 3E, the normalized currents for the dSAC mediated inhibitory events and those elicited by LRGN activation, show a significant difference in rise and decay times, reminiscent of the events in cluster 1 and 3 respectively (comparison for amplitude, rise time and decay time Wilcoxon rank sum $p < 0.001$). Together, these results suggest that sIPSCs in cluster 1 correspond to events elicited by GABA release from dSACs, preferentially targeting the distal dendrites of GCs, whereas events in cluster 3 represents inhibitory inputs from BF-LRGN targeting the perisomatic region of GCs.

To further corroborate that the differences in amplitude and kinetics of the somatically recorded sIPSCs correspond to their spatial origin, we analyzed the properties of GABA evoked currents in GCs using single-photon uncaging (**Figure 4A**). In these experiments, the photolysis of caged GABA (DPNI-GABA) was calibrated to obtain photo-evoked inhibitory postsynaptic currents (uIPSC) of similar amplitude to the sIPSCs (~10-100 pA). To visualize the dendritic arbor of GCs, we included the red fluorophore

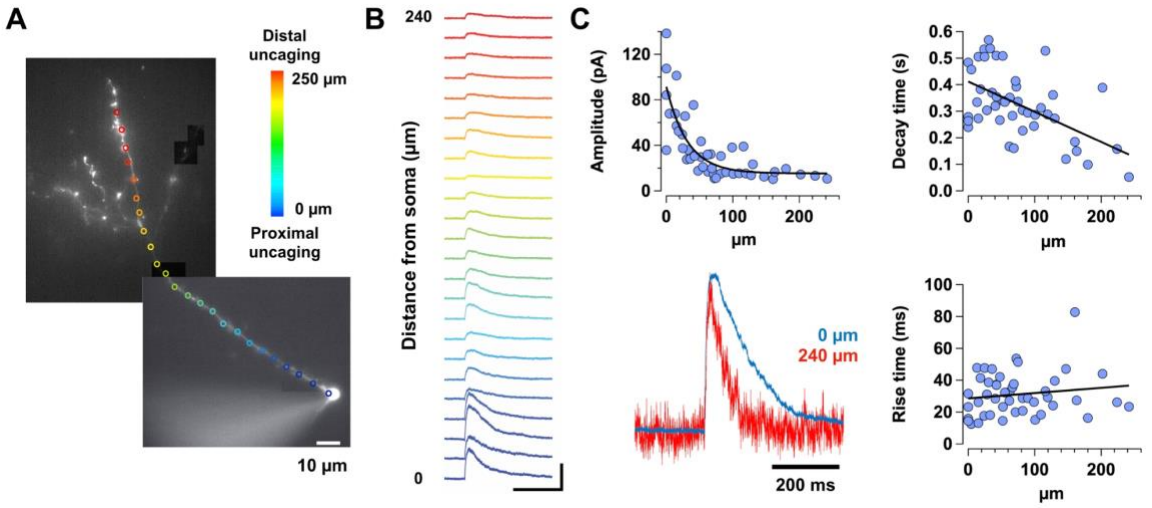

Fig. 4: *Spatial differences in the kinetics of GABAergic currents elicited by laser uncaging along the GC somatodendritic axis*

(A) Representative GC loaded with Alexa fluor-594 and recorded in voltage-clamp, at a holding potential of 0 mV. DPNI-GABA was uncaged along the somatodendritic axis (colored circles) with a 405 nm laser focused through a 60x objective. Cold colors represent proximal spots while warm colors represent distal focused spots. **(B)** Mean traces for the IPSCs elicited by GABA uncaging at different distances from the soma. The color of each trace corresponds to the uncaging position as shown in A. The scale is 100 pA and 200 ms. **(C)** Scatter plots of the amplitude, and the rise and decay time as a function of distance from the soma (n= 4 cells). The amplitude and the decay time of the responses (top graphs) decreased as GABA was uncaged further away from the soma (amplitude: double exponential fit, R-squared= 0.675; decay time: Pearson's linear correlation, r= –0.55). Lower left graph, overlay of representative normalized (to the peak current) traces obtained by uncaging in the proximal (blue trace) and distal (red trace) regions of a GC dendrite illustrating their different kinetics. In contrast, the rise time was not affected by the uncaging distance (bottom right, Pearson's linear correlation, r= 0.15).

Alexa fluor-594 (20 µM) in the internal solution, and the stimulation was ~10 µm apart along the GC somatodendritic axis (**Figure 4A**; see Methods). GABA uncaging in the perisomatic region (0-20 µm), resulted in uIPSCs with an average amplitude of 79.1 ± 10.6 pA and a decay time of 360 ± 30 ms, while at most distal regions (150-250 µm from the soma) both the amplitudes and decay times of the uIPSC were smaller (14.1 ± 1.4 pA; 170 ± 50 ms; n= 4 cells) (**Figure 4B, C**). In contrast, the rise time was not significantly different with distance (proximal 25 ± 4 ms vs distal 36 ± 10 ms, n= 4 cells, p= 0.24) (**Figure 4C**). Together, these results further support the notion that sIPSCs in cluster 1, enhanced in frequency by Mus, correspond to events elicited by GABA release from dSACs and preferentially target the distal dendrites of GCs, whereas events in cluster 3 represents inhibitory inputs from BF-LRGN targeting the perisomatic region of GCs.

dSAC are excited by M3-mAChR activation

To further examine the possibility that the increase in distal inhibition results from dSACs activation by Mus, we recorded from morphologically and physiologically identified dSACs loaded with Alexa fluor-594 in the recording pipette (**Figure 5A**). Morphological analysis indicated that these cells exhibit numerous basal dendrites as well as axonal projections directed toward the EPL (see also Eyre et al., 2008). As previously described (Pressler and Strowbridge, 2006), under resting conditions, a current-stimulus elicited a train of spikes that was followed by an afterdepolarization (ΔV 2 ± 0.8 mV; n= 4), (**Figure 5A**, arrow). As shown in **Figure 5B**, application of Mus produced a robust depolarization of dSACs (ΔV= 5.7 ± 1.1 mV, n= 4, p= 0.01), which was abolished by

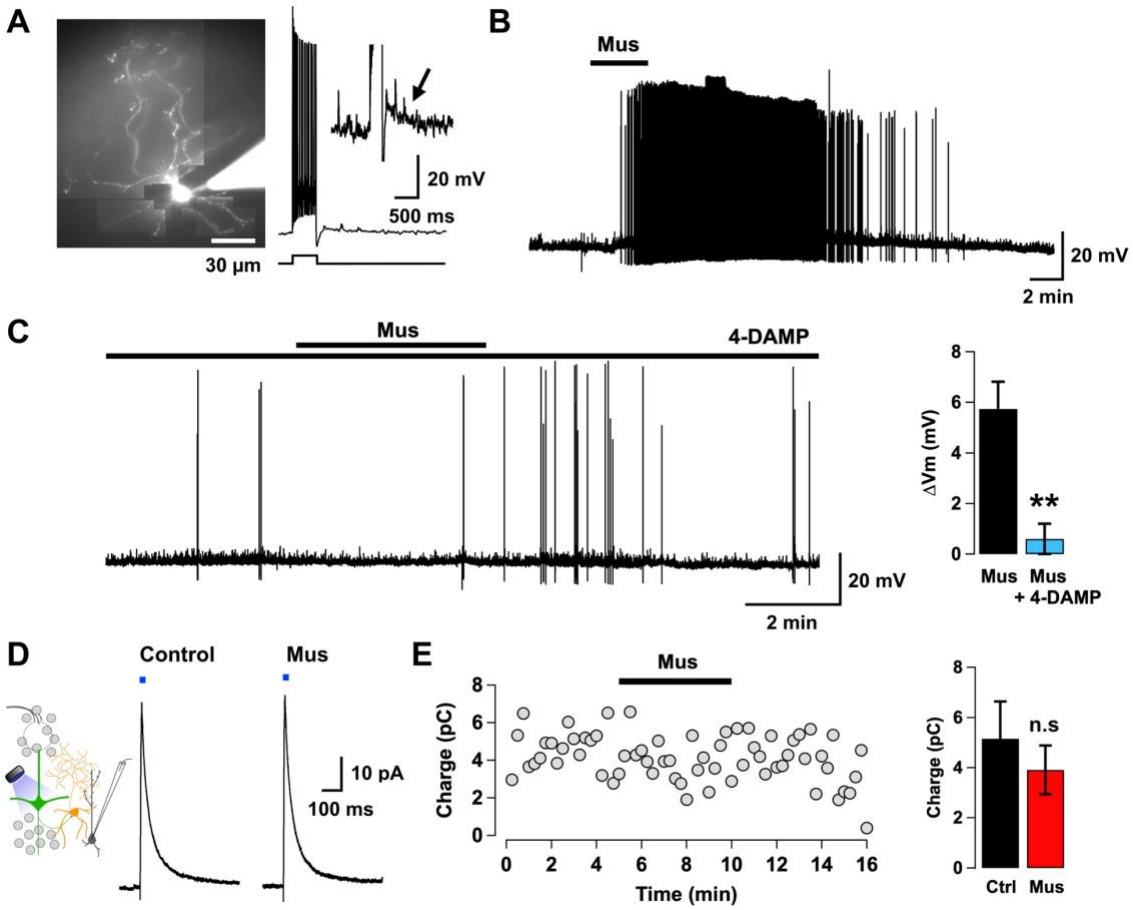

Fig. 5: *Deep short axon cells are excited by M3-mAChR activation*

(A) Left, image of a dSAC loaded with Alexa fluor-594 during a whole-cell recording. Right, these cells exhibit an afterdepolarization (inset, arrow) following a stimulus-induced train of action potentials (150 pA, 500 ms). **(B)** Application of muscarine (Mus, 10 µM) produced a suprathreshold depolarization in this dSAC, with long-lasting spiking. The baseline membrane potential is –60 mV. **(C)** Left, the muscarinic depolarization was significantly reduced in the presence of 4-DAMP (100 nM), a selective M3-mAChR blocker. Right, summary of the effects of Mus and the M3 antagonist in dSACs (n= 4, p= 0.01). (**D**) Diagram showing the experimental configuration used to examine the effect of Mus on the dSAC-mediated inhibition of GCs. Optogenetic stimulation of M/TCs in the *Thy1-EYFP-ChR2* mouse reliably evoked disynaptic IPSCs in GCs recorded at 0 mV. (**E**) The charge of the IPSC evoked by optogenetic stimulation of M/TCs, is not significantly different in the presence of Mus (n= 7, p= 0.3).

application of the selective M3-mAChR antagonist 4-DAMP (100 nM, **Figure 5C**, Mus ΔV 5.74 ± 3.7 mV, Mus in 4-DAMP ΔV 0.35 ± –0.52 mV, n= 4, p= 0.04). Importantly, the disynaptically evoked IPSC recorded in GCs upon M/TCs activation using the *Thy1 EYF-ChR2* mouse was not significantly affected by the activation of mAChRs (control 5.2 ± 1.5 pC vs. Mus 3.9 ± 1 pC, n= 7, p= 0.3) (**Figure 5D, E**).

Depolarization of dSACs by M3-mAChRs activation, is expected to increase GABA release onto GCs, and accordingly, application of 4-DAMP (100 nM) completely abolished the increase in sIPSC frequency in GCs elicited by Mus (**Figure 6A, B**, control 0.54 ± 0.19 Hz vs. Mus in 4DAMP 0.49 ± 0.14 Hz, n= 11, p= 0.41). As expected, the enhancement of inhibition in GCs produced by Mus was not prevented by selective blockade of M1- and M2/M4-mAChRs with pirenzepine (Pir, 1 μM) and AFDX-384 (300 nM), respectively (**Figure 6B**, control in Pir + AFDX-384 0.46 ± 0.1 Hz vs. Mus in Pir + AFDX-384 0.79 ± 0.2 Hz, n= 6, p= 0.04). Together, these results indicate that distal inhibition is enhanced in GCs via an excitatory effect on dSACs that is mediated by M3-mAChRs activation.

Activation of M2/M4-mAChRs suppresses proximal inhibition onto GCs

We next examined the effect of ACh (100 μM) on inhibitory currents elicited in GCs by optogenetic activation of BF-LRGNs axons in the OB. In contrast to the effect on distal inhibition, ACh produced a significant reduction in the light-evoked IPSCs (**Figure 7A**, control 14 ± 4 pC vs. ACh 2.8 ± 0.9 pC, n= 7, p= 0.03), and this effect was completely blocked by Atrp (**Figure 7A, B** control 11 ± 2.2 pC vs. ACh in Atrp 11 ± 2 pC, n= 6, p=

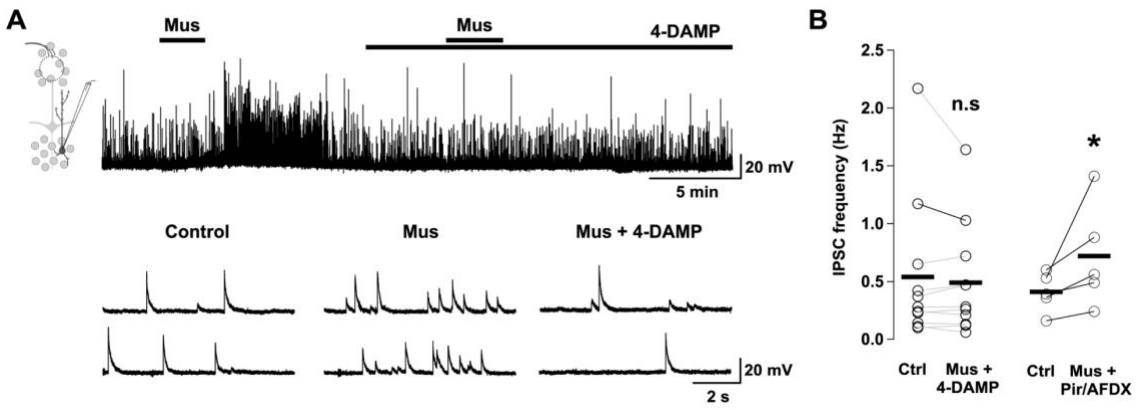

Fig. 6: *M3-mAChR activation is necessary for the enhancement of inhibition in GCs*

(A) Top, the increase in sIPSC frequency in GCs produced by muscarine (Mus, 10 μM) is abolished in the presence of the selective M3-mAChR blocker 4-DAMP (100 nM). The holding potential is 0 mV. Bottom, selected traces of sIPSCs in an expanded time scale, before and after the drug applications as shown in the top trace. **(B)** Summary plots showing the effect of Mus and specific mAChR antagonists. Left, 4-DAMP abolishes the effect of Mus (n= 11, p= 0.4); however, the effect of Mus is not antagonized by a mixture of the M1 and M2/4-mAChR blockers pirenzepine (Pir, 1 μM) and AFDX-384 (300 nM), respectively (n= 6, p= 0.04).

0.8). Likewise, Mus (10 μM) produced a strong reduction in the light-evoked IPSCs (**Figure 7C**, control 9.0 ± 2.3 pC vs. Mus 1.5 ± 0.4 pC, n= 4, p= 0.05), and this effect was blocked by AFDX-384 (300 nM), a selective M2/M4-mAChR antagonist (**Figure 7C**, control, 7.5 ± 1 pC vs. Mus + AFDX-384, 6 ± 0.6 pC, n= 4, p= 0.1), suggesting a presynaptic inhibitory action of M2/M4-mAChRs activation on GABA release from BF-LRGNs axons. In contrast, bath perfusion of the nicotinic ACh receptor (nAChR) agonist nicotine (Nic, 60 μM) had no effect on the light evoked IPSC in GCs (**Figure 7D**, control 14.5 ± 3 pC vs. Nic 13.4 ± 3 pC, n= 6, p= 0.11). Even in the presence of PNU-120596 (PNU, 10 μM), a positive allosteric modulator of nAChRs (Hurst et al., 2005) that reduces their

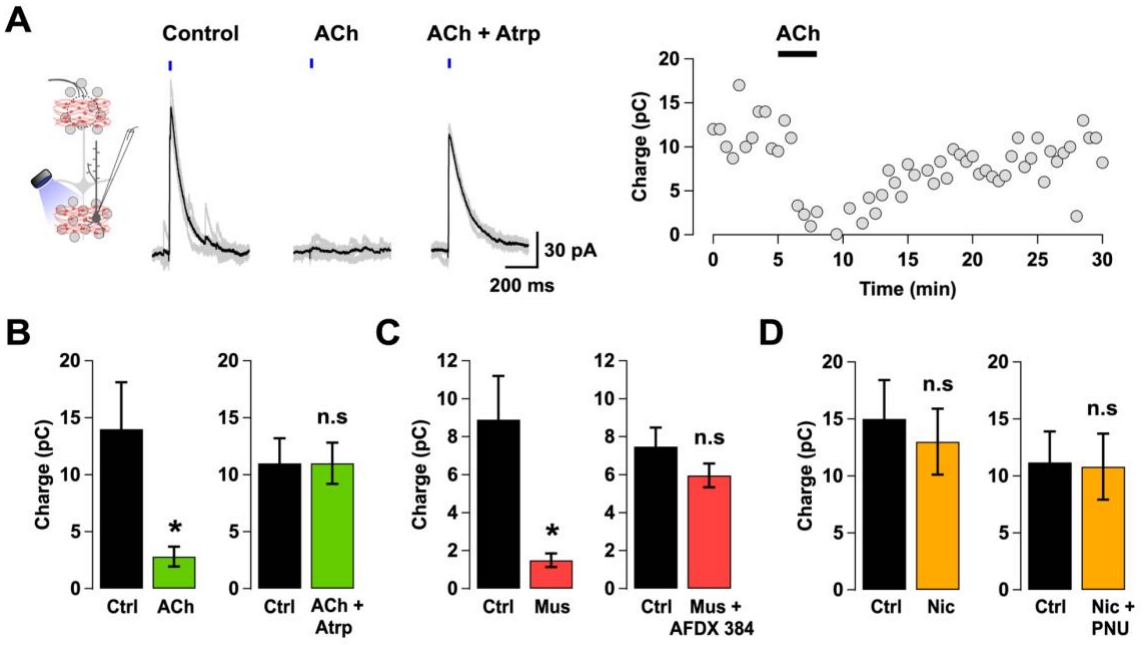

Fig. 7: *Activation of M2/M4-mAChR suppresses afferent inhibition onto GCs*

(A) Recordings were conducted in GCs at 0 mV, in slices of mice expressing ChR2 in MCPO LRGNs (shown in red in the diagram). Left, stimulation with a brief light pulse (1-5 ms) reliably elicited IPSCs in GCs (gray traces); the average amplitude is 122 pA in this cell (black trace). In the presence of ACh (100 μM), optogenetic stimulation failed to evoke the IPSC. The suppressive effect of ACh was blocked by the muscarinic antagonist atropine (Atrp, 3 μM). Right, time course of the effect of ACh in a representative GC where light evoked IPSCs occurred every 30 s; ACh reversibly decreased the charge of the IPSC. **(B)** Summary of the effects of ACh on the light evoked IPSC (left, n= 7, p= 0.03) and the blockade by Atrp (right, n= 6, p= 0.8). **(C)** Left, summary of the effect of Mus (10 μM) on the light evoked IPSC (n= 4, p= 0.05). Right, the suppression of the evoked IPSC by Mus is reversed in the presence of the M2/M4-mAChR antagonist AFDX-384 (300 nM) (n= 4, p= 0.1). **(D)** The light-evoked IPSC was not affected by nicotine (Nic, 60 μM; n= 6, p= 0.11), or by the application of Nic together with the nAChR positive allosteric modulator PNU-120596 (PNU, 10 μM; n= 5, p= 0.74).

desensitization, Nic did not affect the inhibitory currents elicited in GCs by light stimulation (**Figure 7D**, control 11.2 ± 3 pC vs. Nic + PNU 10.8 ± 3 pC, n= 5, p= 0.74). Together, these results indicate that BF GABAergic inhibition of GCs is negatively modulated by cholinergic inputs to the OB, via activation of mAChRs in the LRGN axon terminals, and that local and top-down inhibition onto GCs are differentially modulated by the cholinergic innervation through the activation of distinct mAChRs.

M3-mAChR activation reduces the extent of dendrodendritic inhibition in MCs

Increased inhibition at the distal dendritic segments of GCs is expected to negatively impact the extent of inhibition at GCs to MCs synapses. To examine this possibility, we recorded inhibitory currents in MCs evoked by a brief depolarizing train, while holding the cell at −60 mV, using a CsCl based internal solution. This stimulation elicited a barrage of GABAergic currents with a relaxation time of 564 ± 176 ms (n= 9 cells), similar to values previously reported (Isaacson and Strowbridge, 1998; Schoppa, 1998; Villar et al., 2021a). In the presence of Mus, dendrodendritic inhibition (DDI) in MCs was significantly reduced (**Figure 8A** control: –55 ± 7 pC vs. Mus: –40 ± 4 pC, n= 18, p= 0.04). Intriguingly, in the presence of Mus, application of the M3-mAChR blocker, 4-DAMP, produced a significant increase in DDI in MCs (**Figure 8B**, control –39 ± 4 pC vs. Mus in 4-DAMP –51 ± 7 pC, n= 16, p= 0.01). We suspect this is due to an increase in excitability in GCs produced by M1-mAChRs activation (Smith et al., 2015), and accordingly, blockade of both M1 and M3-mAChRs abolished this effect (control, –45 ± 8 pC vs. Mus + 4-DAMP + Pir, –42 ± 9 pC, n= 13, p= 0.44; not shown). Last, the reduction

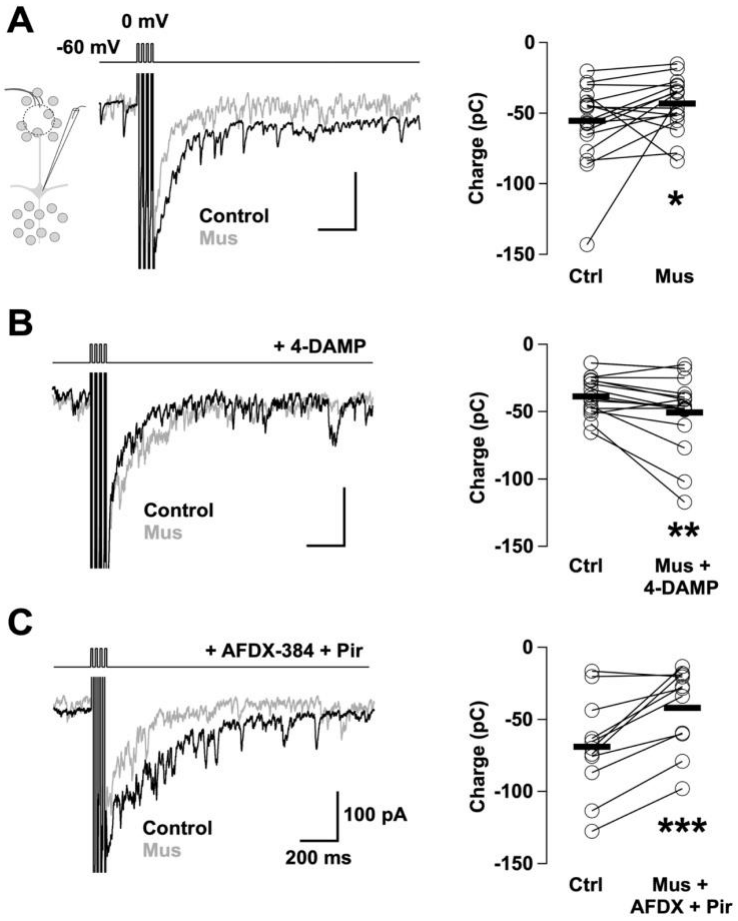

Fig. 8: *Activation of M3-mAChRs modulates the extent of dendrodendritic inhibition in MCs*

(A) MCs were recorded in voltage-clamp at –60 mV using a CsCl based internal solution; dendrodendritic inhibition (DDI) was elicited by a brief depolarizing train of depolarizing steps (4 x10 ms). The average evoked GABAergic current (black trace) was decreased in the presence of Mus (gray trace, Mus 10 μM). Right, summary of the effect of Mus in DDI quantified as the charge (n= 18, p= 0.04). **(B)** Left, in the presence of the M3-mAChR antagonist, 4-DAMP (100 nM), Mus failed to reduce DDI, but instead produced a small but significant increase in DDI. These effects are summarized in the right plot (n= 16, p= 0.01). **(C)** Left, the decrease in DDI elicited by Mus was still present in the presence of AFDX-384 (300 nM) and pirenzepine (Pir, 1 μM), antagonists of the M2 and M1-mAChRs, respectively. These effects are summarized in the right plot (n= 11, p< 0.001).

in inhibition produced by Mus persisted in the presence of the selective M2/M4 and M1-mAChR blockers, AFDX-384 and Pir, respectively (**Figure 8C**, control in AFDX-384 + Pir: –69 ± 10 pC vs. Mus + AFDX-384 + Pir: –42 ± 9 pC, n= 11, p< 0.001). These results support the hypothesis that the activation of M3-mAChRs in dSAC reduces the extent of DDI in MCs by increasing incoming GABAergic inhibition in the distal dendrites of GCs.

Inhibitory and excitatory top-down inputs onto GCs are differentially modulated by mAChRs

The OB integrates glutamatergic feedback from the PC, which decorrelates the activity of output neurons by driving strong excitation onto the OB local GABAergic circuits (Boyd et al., 2012; Otazu et al., 2015). This excitatory feedback, like the BF inhibitory input, mainly targets the proximal region of GCs (Balu et al., 2007), and therefore, we wondered whether this excitatory input was also inhibited by muscarinic activation. To this extent, we injected the adenovirus AAV-ChR2-mCherry into the PC of wild type mice, which resulted in abundant axonal labeling distributed across the different OB layers, especially in the GCL (**Figure 9A**). In voltage-clamp recordings brief light stimulation (1-5 ms) reliably evoked large inward currents in GCs, which were sensitive to the AMPA receptor blocker CNQX (10 μM) (control –1.3 ± 0.2 pC vs. CNQX –0.2 ± 0.05 pC; n= 7, p= 0.001), as previously shown (Boyd et al., 2012). Intriguingly, application of Mus did not alter the light-evoked EPSC (control –1.3 ± 0.3 pC vs. Mus –1.3 ± 0.2 pC, n=

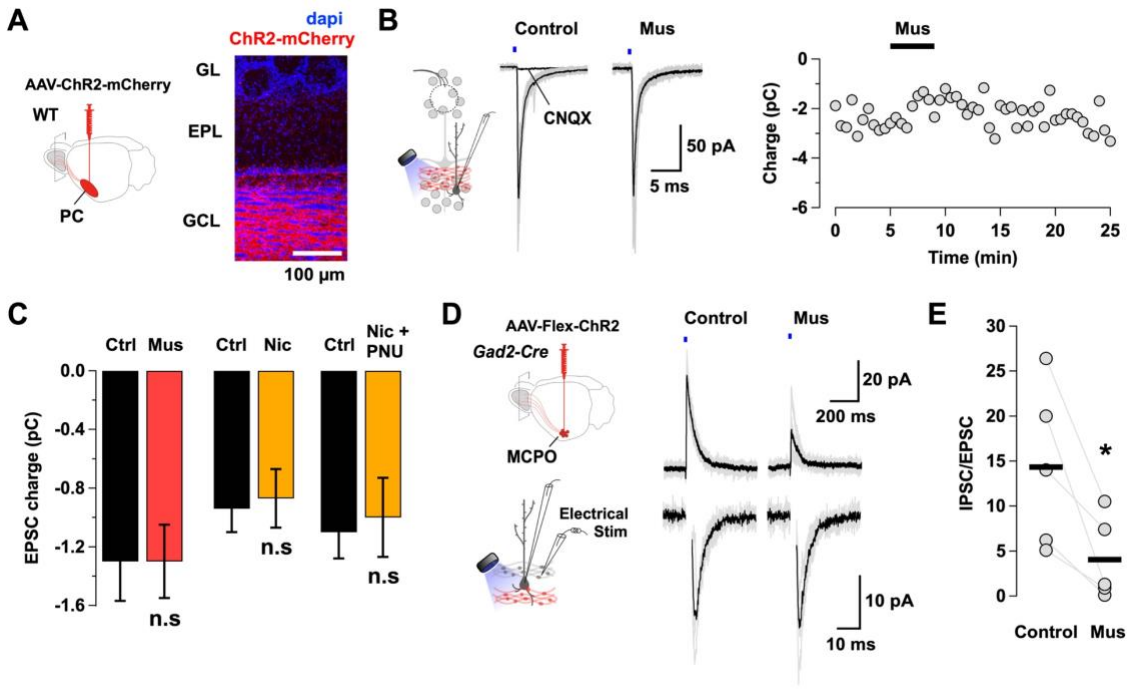

Fig. 9: *Activation of mAChRs suppresses extrinsic inhibition but not extrinsic excitation of GCs*

(A) Left, cortical feedback projections were transduced with ChR2 by injecting the anterograde virus AAV-ChR2-mCherry in the PC of wild type mice, which resulted in extensive labeling of the GC layer (right). **(B)** We conduced voltage-clamp recordings in GCs while optogenetically stimulating the PC excitatory axons (red). Stimulation with a brief light pulse (1-5 ms) in this GC elicited large inward currents (gray traces), with an average amplitude of 170 pA (black trace). The inward current was completely abolished by the AMPA receptor blocker CNQX (10 µM, n= 7, p= 0.001) but not significantly affected by Mus (10 µM), shown on the right-hand side plot. **(C)** Left, bar graphs summarizing the effects of different cholinergic drugs on the light evoked EPSC. The PC excitatory input was not affected by Mus (n= 6, p= 0.88), Nic (60 µM, n= 5, p= 0.2) or Nic in the presence of PNU-120596 (PNU, 10 µM) (n= 4, p= 0.6). **(D)** We recorded simultaneously both the afferent excitatory and inhibitory inputs onto GCs in *Gad2-Cre* mice injected with AAV-Flex-ChR-mCherry in the MCPO. The cortical feedback was stimulated by placing an electrode in the GCL (bottom). Right, in this GC, light stimulation at 0 mV elicited outward currents (upper gray traces) with an average of 46 pA (black trace), which was greatly reduced by Mus (18 pA). In the same GC, recorded at –60 mV, brief electrical stimulation in the GCL (100 µA, 100 µs) evoked inward currents (lower gray traces) with an average of 20 pA (black trace), which was not affected by Mus (21 pA). **(E)** The IPSC to EPSC ratio of the synaptic charge (absolute value) evoked by light

(inhibition) and electrical stimulation (excitation) in the same GC decreases in the presence of Mus (n= 5, p= 0.02).

6, p= 0.88) (**Figure 9B, C**). Similar results were obtained when we applied Nic (60 µM) alone or in the presence of PNU (10 µM) (control, –0.9 ± 0.2 pC vs. Nic, –0.9 ± 0.2 pC, n= 5, p= 0.2; control, –1.1 ± 0.2 pC vs. Nic + PNU, –1 ± 0.3 pC, n= 4, p= 0.6) (**Figure 9C**). Nevertheless, consistent with a previous study (Mazo et al., 2016), activating $GABA_BRs$ with the agonist baclofen (Bac, 50 µM) strongly suppressed the light-evoked EPSC in GCs (control –0.9 ± 0.2 pC vs. –0.2 ± 0.1 pC, n= 6, p= 0.02; not shown). These results suggest that the excitatory/inhibitory balance in GCs can be modulated by mAChR activation.

Thus, in a subset of GCs, we optogenetically activated the MCPO GABAergic axons (as in **Figure 3** and **Figure 7**), while the cortical feedback was electrically stimulated by placing a stimulating electrode in the GCL (**Figure 9D**) (Balu et al., 2007). The optogenetically evoked IPSC (top trace) and electrically evoked EPSC (bottom trace) were isolated by recording at 0 and –60 mV, respectively, using a Cs-based internal solution. At –60 mV, brief current pulses (100 µA, 100 µs) reliably evoked EPSCs in GCs, which were completely blocked by CNQX (control –0.4 ± 0.2 pC vs. CNQX –0.1 ± 0.05 pC, n= 5, p= 0.05; not shown). In the same GC, Mus selectively suppressed the light-evoked IPSCs, but not the electrically evoked EPSC (IPSC control, 2.6 ± 0.2 pC vs. in Mus, 0.6 ± 0.2 pC n= 5, p< 0.01; EPSC, control, –0.3 ± 0.1 pC vs. in Mus, –0.3 ± 0.1, n= 5, p= 0.7). Consistently, Mus produced a strong decrease in the IPSC to EPSC ratio in GCs (**Figure 9E**) (|IPSC/EPSC|, control 14.3 ± 4 vs. Mus 4 ± 2, n= 5, p= 0.02), suggesting an increase in the overall proximal excitatory weight in GCs upon cholinergic activation.

Discussion

Here, we provide new mechanistic insights on how synaptic inputs onto proximal and distal dendritic domains of GCs are modulated by the cholinergic system and shape the output of the bulb. Analysis of the waveform of spontaneously occurring GABAergic currents revealed at least two groups of events with distinguishing features; events of small amplitude with fast decay (cluster 1), and events of large amplitude with slower decay (cluster 3) (**Figure 1, 2**). Photo-uncaging of GABA indicated that events in cluster 3 originate in the proximity of the soma, while events in cluster 1 originate in distal regions of GCs (**Figure 4**). Furthermore, optogenetic activation of dSACs or BF-LRGN axons, elicited IPSCs with properties resembling distal and proximal inputs, respectively, suggesting a spatial segregation of inhibitory inputs in GCs (**Figure 3**). Interestingly, activation of mAChRs produced opposite effects on these inhibitory inputs; activation of M3-mAChRs greatly enhanced the occurrence of inhibitory currents in GCs, by depolarization of dSACs that synapse onto GCs (**Figure 5, 6**). In contrast, activation of the M2/M4-mAChRs depressed GABAergic currents elicited by activation of BF inputs (**Figure 7**). These distinct effects on proximal vs. distal inhibition in GCs are expected to regulate the degree of inhibitory output at M/TC-GC synapses. Activation of M3-mAChRs reduced the extent of dendrodendritic inhibition in MCs, suggesting a local regulation of inhibition (**Figure 8**). Interestingly, the glutamatergic feedback to the OB was not affected by Mus, suggesting that the overall effect of proximal muscarinic modulation is to shift the balance towards excitation of GC, enhancing global inhibition (**Figure 9**).

The activity of M/TCs is functionally regulated by several types of inhibitory neurons, which target their primary and secondary dendrites (Price and Powell, 1970a; Shepherd, 2004). Among the inhibitory neurons of the OB, the most prominent in number are the GCs, which participate in recurrent and lateral inhibition through synapses with lateral dendrites of M/TCs (De Olmos et al., 1978; Luskin and Price, 1983). Most dendrodendritic synapses (DDS) are located in the distal dendrites of the GCs, where they also receive dense inhibition from local dSACs (Eyre et al., 2008; Burton and Urban, 2015). In contrast, the proximal dendritic compartment and soma of the GCs receive dense innervation from top-down afferent axons (Záborszky et al., 1986; Matsutani and Yamamoto, 2008; Zaborszky et al., 2012; Nagayama et al., 2014), including excitatory cortical feedback, and cholinergic and GABAergic inputs from the BF (Matsutani and Yamamoto, 2008; Gracia-Llanes et al., 2010; Boyd et al., 2012; Markopoulos et al., 2012; Nunez-Parra et al., 2013; Villar et al., 2021a). This synaptic organization of inputs suggests two separate functional domains of inhibition in GCs: a proximal domain, largely containing top-down GABAergic inputs from the BF (Eyre et al., 2008; Villar et al., 2021a), and a distal domain, comprised by local feedforward inhibition from dSACs (Eyre et al., 2008). Using a waveform clustering approach, we were able to distinguish between these two populations of inhibitory currents based on their amplitudes and decay times. Our results with selective optogenetic control of proximal (LRGNs) and distal (dSACs) inhibitory inputs onto GCs are consistent with this idea. While LRGNs activation evoked IPSCs with larger amplitude and slower decay time, disynaptic stimulation of dSACs elicited IPSCs with smaller amplitude and faster decay times (clusters 3 and 1, respectively). Segregated inhibitory inputs onto GCs are supported by previous studies

indicating that a subpopulation of dSACs preferentially target the distal dendrite of GCs (Eyre et al., 2008), while BF-LRGN axons are notoriously more abundant in the GCL, suggesting a perisomatic innervation of GCs (Gracia-Llanes et al., 2010; Villar et al., 2021a). Nevertheless, the amplitude and decay times of the IPSCs evoked by these stimulations overlap to a considerable degree, which comprised cluster 2, suggesting topologically overlapping inputs from LRGNs and dSACs along the GC somatodendritic axis (Burton and Urban, 2015). Intriguingly, the increase in frequency of inhibitory events was observed in half of the population of GCs examined. The reason for this is unknown but we note that the frequency of inhibitory events was not different between responding and non-responding GCs, and disynaptic responses elicited in GCs occurred with high probability. This suggests that there could be differences in the muscarinic response in dSACs, or differences in the efficiency of eliciting disynaptic and/or muscarinic responses in these neurons in the slice. Further experiments should address this possibility.

While signal dampening by electrotonic conduction predicts a decrease in event amplitude for distal events (Armstrong and Gilly, 1992), the faster decay of these events was unexpected. One possible explanation for this discrepancy is that proximal and distal GABAergic synapses onto GCs could have different properties. For example, the composition of postsynaptic $GABA_A$ receptors ($GABA_AR$) could vary along the somatodendritic axis of GCs, giving rise to synaptic currents with distinctive kinetics. The identity of $GABA_AR$ subunits expressed in the proximal and distal dendritic compartment of GCs is unknown, however different combinations of $GABA_AR$ subunits or posttranslational modifications of receptors have been shown to greatly impact the kinetic of the postsynaptic currents (Laurie et al., 1992; Moss et al., 1992; McDonald et al., 1998;

Moss and Smart, 2001; Nusser et al., 2001; Nakamura et al., 2015; Nunes and Kuner, 2015). The observed differences in decay time of currents elicited with photo-uncaging are consistent with heterogeneous properties of $GABA_AR$ along the somatodendritic axis of GCs. Future experiments characterizing single channel properties of $GABA_ARs$ along the somatodendritic axis of GCs could clarify the degree of heterogeneity of GABAergic currents in GCs.

ACh regulates network function by altering the excitation-inhibition balance of neural circuits (Pitler and Alger, 1992; Behrends and Bruggencate, 1993; Wanaverbecq et al., 2007), and in the OB, cholinergic modulation has been shown to play a role in odor discrimination and learning (Doty et al., 1998; Linster and Cleland, 2002; Wilson et al., 2004; Hellier et al., 2012; Chapuis and Wilson, 2013; Hanson et al., 2021). Our results provide evidence supporting that the activation of distinct mAChRs results in a differential modulation of intrinsic and extrinsic sources of inhibition onto GCs. Cholinergic modulation of GABAergic inhibition has been previously shown in the hippocampus (Pitler and Alger, 1992; Hasselmo and Schnell, 1994; Wanaverbecq et al., 2007), thalamus (Antal et al., 2010; Ye et al., 2010) and cerebral cortex (Hasselmo and Bower, 1992; Gil et al., 1997; Kimura and Baughman, 1997; Patil and Hasselmo, 1999; Kimura, 2000; Brombas et al., 2014). Intriguingly, while muscarinic presynaptic inhibition of neurotransmitter release has been reported for glutamatergic (Hasselmo and Sarter, 2011), as well as, GABAergic synapses (Behrends and Bruggencate, 1993; Kimura and Baughman, 1997; Patil and Hasselmo, 1999), in the OB, muscarinic presynaptic inhibition occurred in the BF GABAergic input but not in the excitatory cortical feedback. This differential effect at the somatic level would increase the synaptic weight of the excitatory

feedback, and somatic disinhibition of GCs, increasing dendrodendritic and lateral inhibition on M/TCs due to a higher likelihood of generating somatic action potentials in GCs, thus reducing spatial activation of M/TCs and possibly favoring odor pattern separation. Interestingly, a previous study (Mazo et al., 2016) showed that regulation of excitation onto GC by presynaptic inhibition can modulate beta oscillations, suggesting that muscarinic modulation of GC inhibition could also affect oscillatory activity in the OB. Further experiments will be necessary to test these possibilities.

Appendix B

Supplementary figures Chapter 2

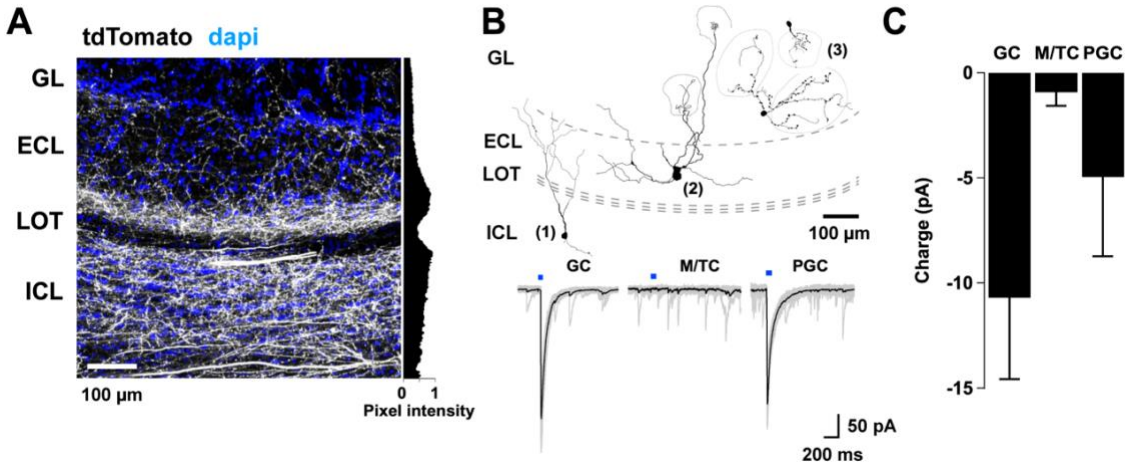

Fig. 1-1: *Inhibitory neurons are postsynaptic partners of MCPO long-range GABAergic neurons in the AOB*

(A) Confocal image of a sagittal section of the accessory OB (AOB) expressing tdTomato in the MCPO GABAergic axons (shown in white). Nuclei stained with dapi are shown in blue and delineate the different cellular layers of the AOB. The histogram on the right shows the average normalized pixel intensity across the cellular layers; GL, 0.29 ± 0.05; ECL, 0.62 ± 0.11 and GCL, 0.92 ± 0.06 (n= 4). **(B)** Upper panel, example of reconstructed neurons, post-recording; 1, GC; 2, mitral/tufted cell (M/TC); 3, PGC. The morphology of the neurons was reconstructed from confocal images of fixed cells that were filled with Alexa Fluor-594 during the recordings. Bottom, sample eIPSCs elicited by LED stimulation (5 ms) of GABAergic axons expressing ChR2. GABAergic currents were observed in GCs and PGCs, but not in the output neurons, the M/TCs, in recordings at −70 mV. GL, glomerular layer; ECL, external cellular layer; LOT, lateral olfactory tract; ICL, internal cellular layer. **(C)** Bar graph showing the total charge transferred during the GABAergic eIPSCs in distinct cell types in the AOB; responses are observed in the main inhibitory types, but not in the output neurons (GC, n= 12; M/TC, n= 6, PGC, n= 5).

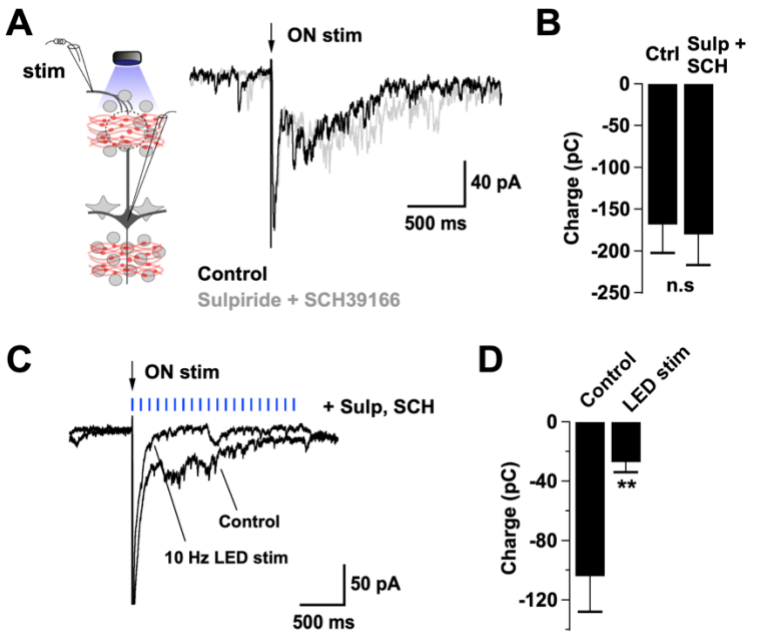

Fig. 4-1: BF GABAergic modulation of dendrodendritic inhibition in MCs does not involve the activation of dopaminergic receptors

(A) Left, diagram of the experimental configuration; MCs where voltage clamped at −60 mV while the olfactory nerve (ON) was briefly activated by an electrical stimulation. BF GABAergic axons expressing ChR2 were activated by blue light in the GL. Right, synaptic currents evoked in a MC by electrical stimulation of the ON (100 μA, 100 μs, arrow, black trace) were not significantly altered when we perfused the D1 and D2 dopaminergic receptor antagonists SCH39166 (SCH, 10 μM) and Sulpiride (Sulp, 100 μM), respectively (gray trace). The holding potential is −60 mV **(B)** The total charge transferred in MCs by ON stimulation does not significantly change when blocking dopamine receptors (n= 10, p= 0.62). **(C)** Overlaid of average current traces from a representative MC evoked by ON stimulation in the absence (control) or presence of 10 Hz blue light stimulation when dopaminergic receptors were blocked with Sulpiride and SCH. **(D)** Activating BF GABAergic axons with blue light significantly reduced the ON evoked synaptic currents in MCs in the presence of dopaminergic receptor antagonists (n= 6, p= 0.01).

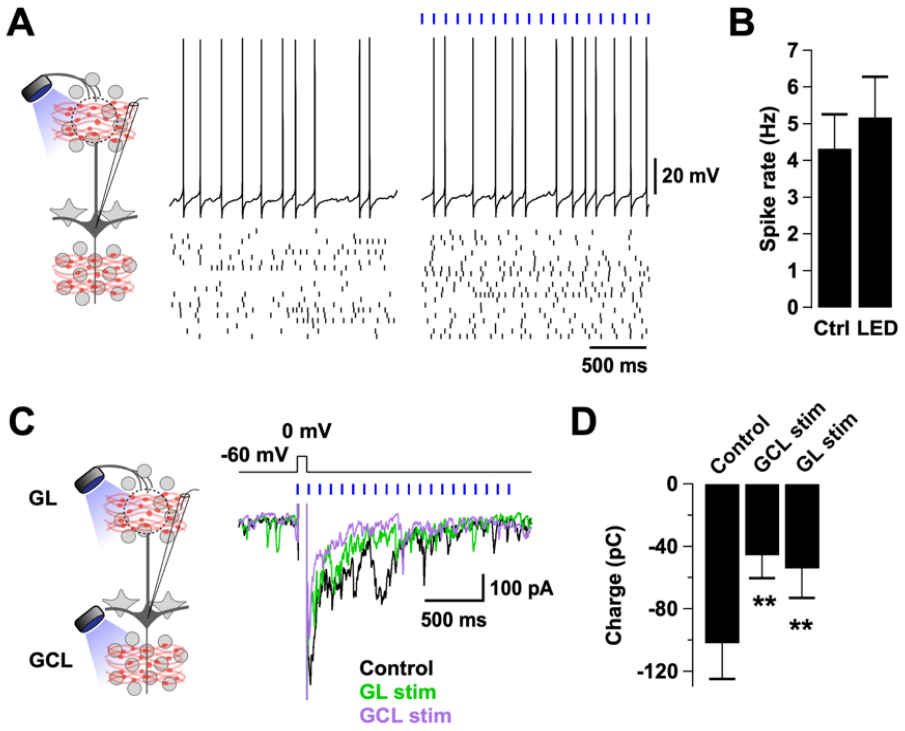

Fig. 4-2: *Activation of glomerular and infraglomerular BF GABAergic axons influence dendrodendritic inhibition in MCs*

(A) Left, diagram of the experimental configuration; MCs where depolarized by somatic current injection to evoke spiking while BF GABAergic axons were optogenetically stimulated with 10 Hz blue light in the glomerular layer (GL). Right, voltage traces of a representative MC held at peri-threshold membrane potential in control (left) and in the presence of blue light stimulation (right). Spike raster plots for 25 trials are shown below. **(B)** Summary plot for spike rate in MCs showing no significant change in the mean spike frequency during blue light stimulation in the GL compared to control (n= 7, p= 0.25). **(C)** Left, diagram of the experimental design; MCs were voltage clamped at −60 mV and briefly (50 ms) depolarized to 0 mV to activate dendrodendritic synapses. In some trials blue light was focused to the GL or GCL to activate BF GABAergic axons. Right, overlaid of average current traces from a representative MC in the control condition (black trace), and when blue light was focused in the GL (green trace) or the GCL (purple trace). **(D)** Bar plot showing the comparison of total charge transferred in MC evoked by a depolarization step during control and blue light stimulation in the GL and GCL. Focusing the stimulation in either GL or GCL significantly reduced the evoked GABAergic current in MCs (GL stimulation, n= 5, p= 0.007; GCL stimulation, n= 5, p= 0.006).

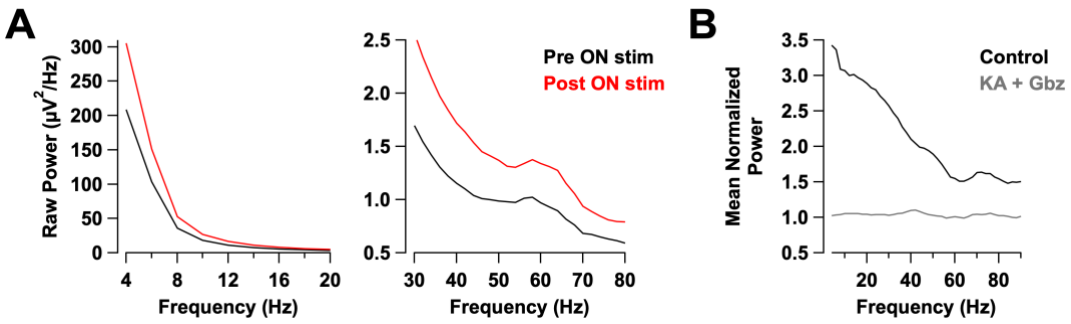

Fig. 5-1: *LFP induction in olfactory bulb slices and power modulation by BF GABAergic axons activation*

(A) Comparison of the raw 300 Hz low pass power spectra for the θ (left) and γ (right) frequency bands before (black) and after (red) a brief stimulation of the olfactory nerve (ON). **(B)** Mean normalized power spectra before (black) and after (gray) bath perfusing the synaptic blockers kynurenic acid (1 mM, KA) and gabazine (10 µM, Gbz).

Supplementary figures Chapter 3

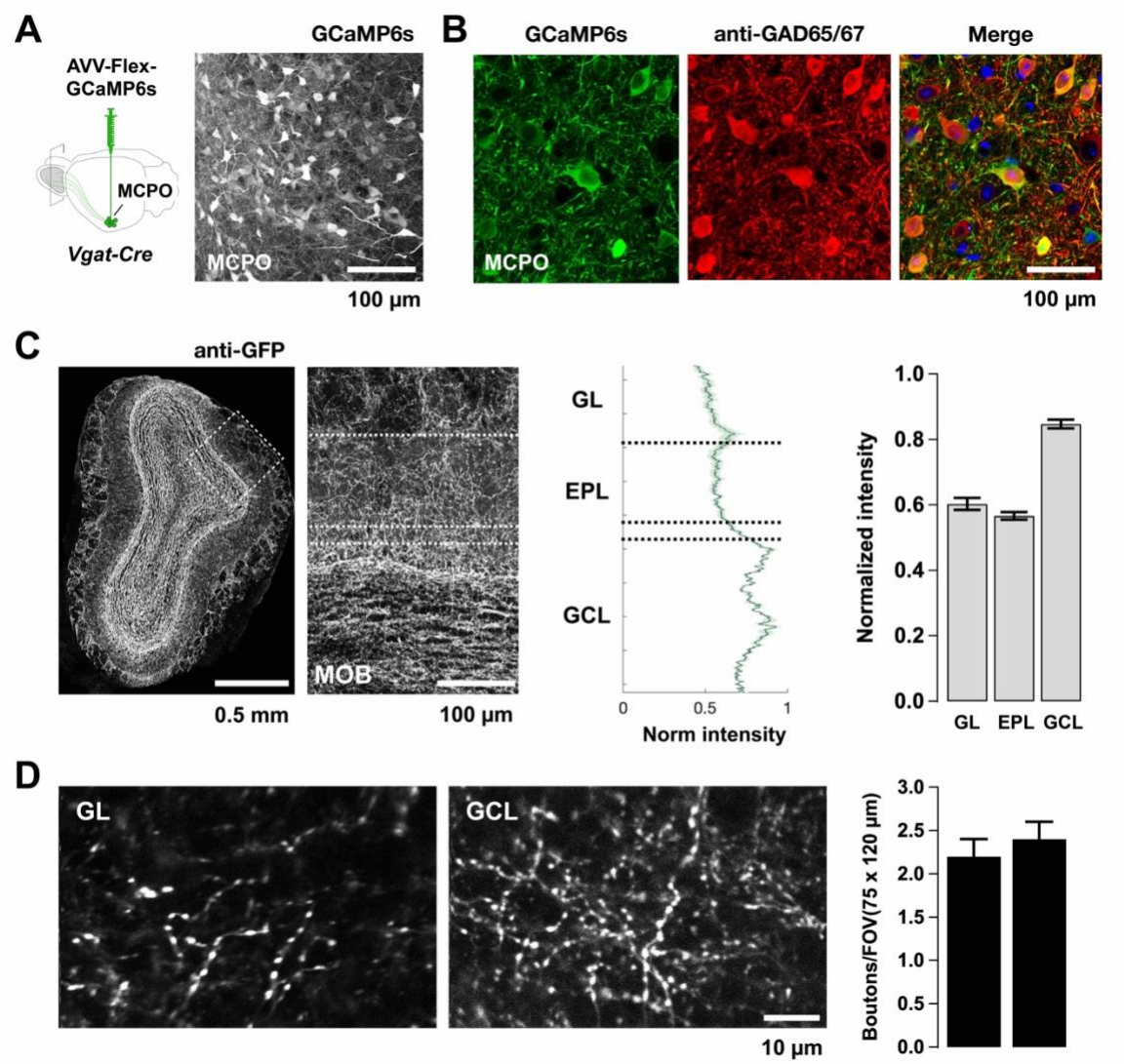

Fig. 2-1: *Laminar distribution of the MCPO GABAergic axons in the OB*

(A) Left, schematic of the experimental approach. *Vgat-Cre* mice were injected in the MCPO with the Cre-dependent virus AAV-Flex-GCaMP6s to monitor the activity of MCPO GABAergic projections in the OB. Right, confocal image showing abundant GCaMP6s expression in the MCPO. **(B)** To confirm the GABAergic nature of GCaMP6s expressing cells in the MCPO, slices were immunostained using an anti-GAD65/67 antibody. GCaMP6s intrinsic fluorescence (green) largely overlapped with the GAD65/67 signal (red) in the MPCO

(n= 3) **(C)** Left, confocal image of a coronal section of the OB containing MCPO GABAergic axons expressing GCaMP6s. Intrinsic GCaMP6s expression was amplified by immunohistochemistry against GFP. GABAergic axons were homogeneously distributed across the dorso-ventral axis of the OB. Center, confocal image of the dorsal OB showing the laminar distributions of GABAergic axons. Right, mean normalized pixel intensity across layers (n= 3). The densest distribution of axons was found in deeper layers of the OB. **(D)** Left, *in vivo* two-photon images of MCPO GABAergic boutons in the GL and GCL. Right, the density of GABAergic boutons was slightly higher in the GCL compared to GL (mean boutons/100µm^2: GCL 2.4 ± 0.2 vs. GL 2.2 ± 0.2 boutons/100µm^2, n= 19 GCL FOVs, 20 GL FOVs).

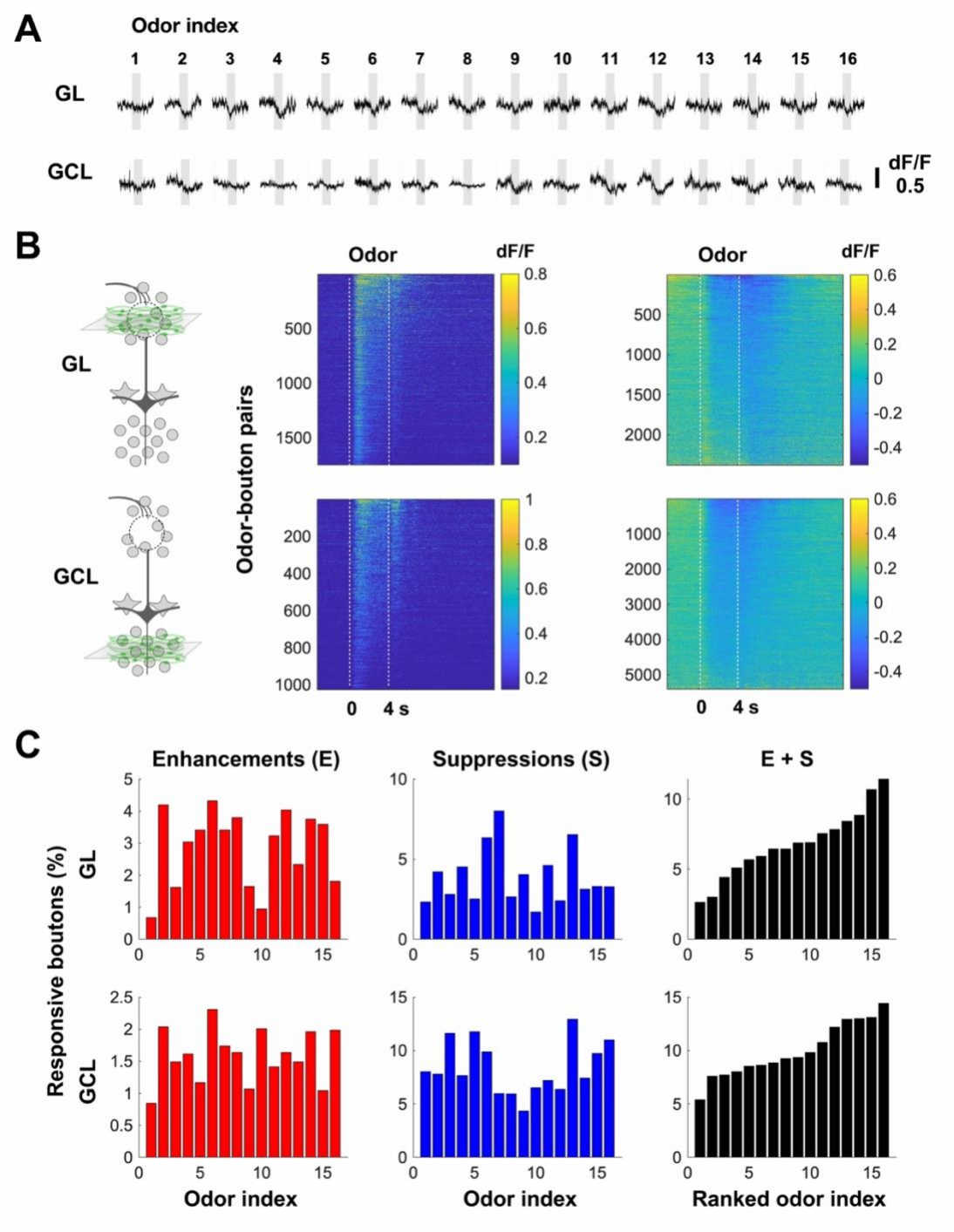

Fig. 2-2: *GABAergic bouton responses evoked by single odors across the OB layers*

(A) Sample dF/F traces for a selected bouton in the GL (top) and in the GCL (bottom) showing suppressed odor responses to a set of 16 odors. **(B)** Responsive odor-bouton pairs imaged in the GL (top, 20 FOVs, 5 mice) and GCL (bottom, 19 FOVs, 6 mice). Enhanced (left) and

suppressed (right) odor-evoked responses were ranked by mean amplitude. **(C)** Bar graphs showing the percentage of boutons responding with enhancements (left) or suppressions (center) for each odor in the panel. Right, percentage of responsive boutons (either enhanced or suppressed) shown from the least to most responding odor.

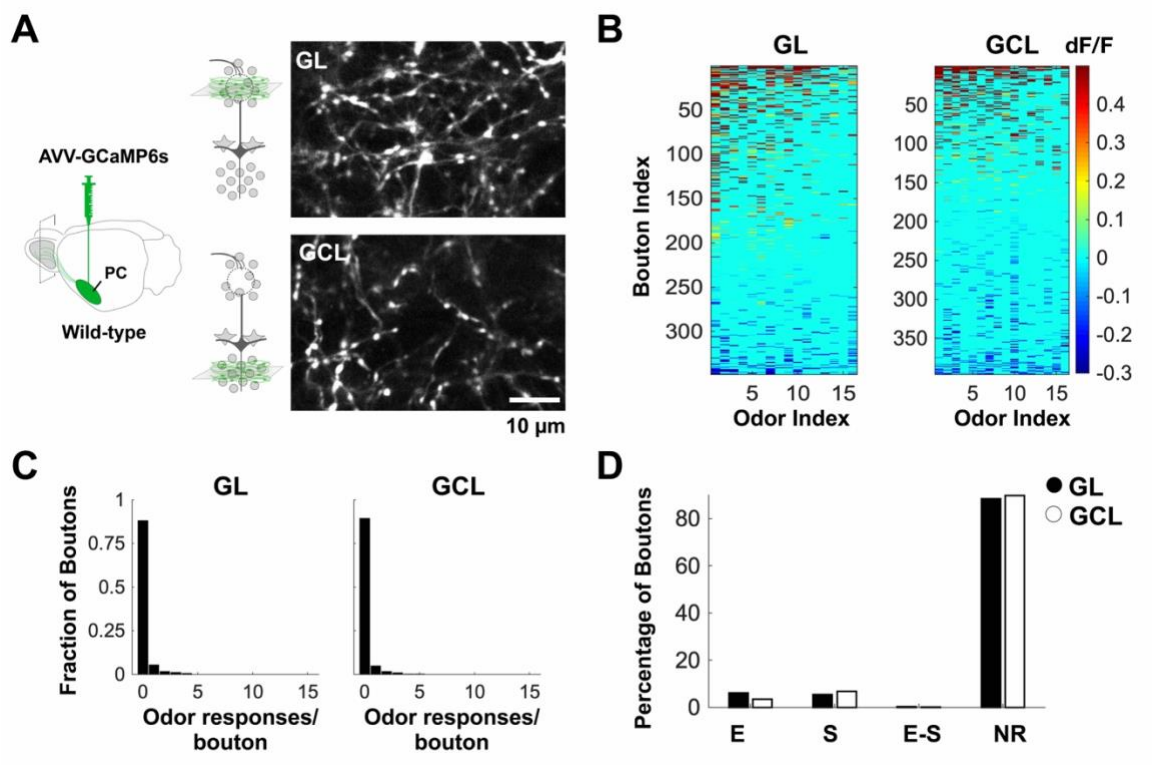

Fig. 2-3: *Odor responses in boutons of glutamatergic axons from PC neurons projecting to the OB expressing GCaMP6s*

(A) Left diagram; C57/B6 wild-type mice were injected with an adenovirus (AAV1-Syn-GCaMP6s) into the piriform cortex (PC) to drive expression GCaMP6s in glutamatergic feedback projections. Right, *in vivo* two-photon images of boutons in corticobulbar axons in the GL (top) and GCL (bottom). **(B)** Heatmap of mean odor-evoked responses for boutons in the GL (right, 16 FOVs, 3 mice) and GCL (left, 19 FOVs, 3 mice) that responded significantly to at least one odor stimulus (out of 16). Responsive boutons are shown ranked by magnitude from the most to the least responsive. Red indicates enhanced responses while blue suppressed responses. **(C)** Histogram showing the number of odor-evoked responses per bouton in PC feedback axons in the GL (left) and GCL (right). **(D)** Percentage of boutons in the GL (black bars) and GCL (white bars) that responded exclusively with either enhancement (E) or suppression (S), exhibited both E and S (E-S), and non-responsive boutons (NR).

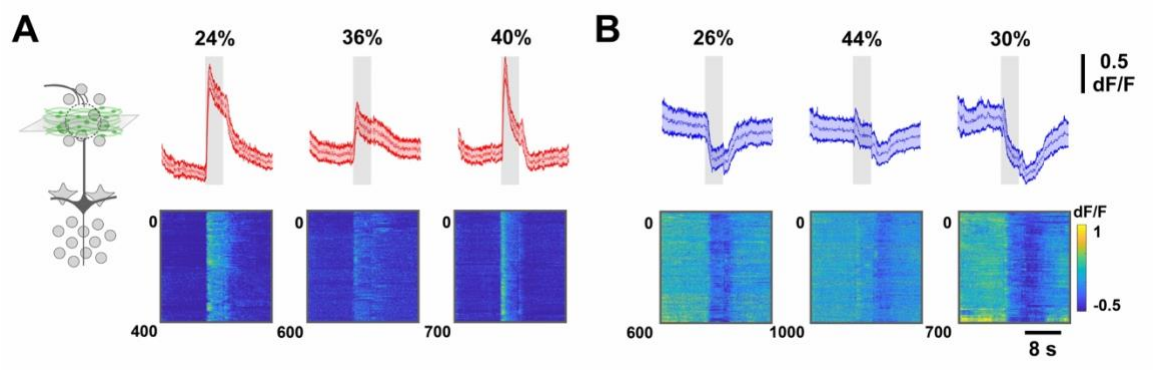

Fig. 4-1: *Odor-evoked kinetics of the GABAergic boutons in the GL*

K-means clustering of enhanced **(A)** and suppressed **(B)** odor-evoked responses in the GL obtained using the 16 odors panel. Only dF/F traces from responding odor-bouton pairs were used for this analysis. Top, mean odor responses obtained from all odor-bouton pairs pertaining to each cluster. The percentage of odor-bouton pairs assigned to a particular cluster is indicated on top of each mean trace. Vertical gray bars indicate the time of odor presentation. Bottom panels, heatmaps of the activity of all odor-bouton pairs for a given cluster.

Supplementary figures Chapter 4

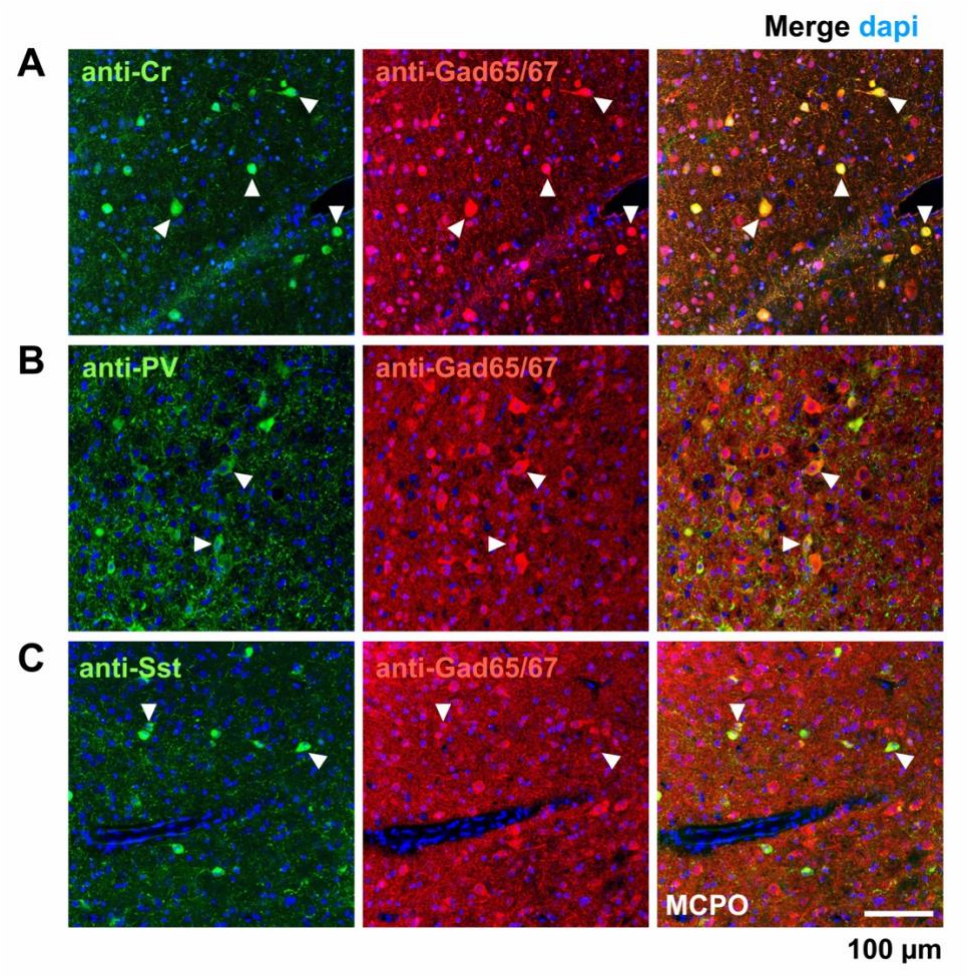

Fig. 2-1: *The MCPO contains a heterogenous group of GABAergic neurons*

Confocal images of coronal MCPO sections immunostained with antibodies against the GABAergic markers Cr (**A**), PV (**B**) and Sst (**C**) shown in green. The total population of GABAergic neurons was labeled using the Gad65/67 antibody, shown in red. Nuclear dapi staining is shown in blue. These representative images illustrate the expression of Cr, PV and Sst among the MCPO GABAergic population. Arrows indicate example cells were colocalization of the protein Gad65/67 and the corresponding GABAergic marker is most clear.

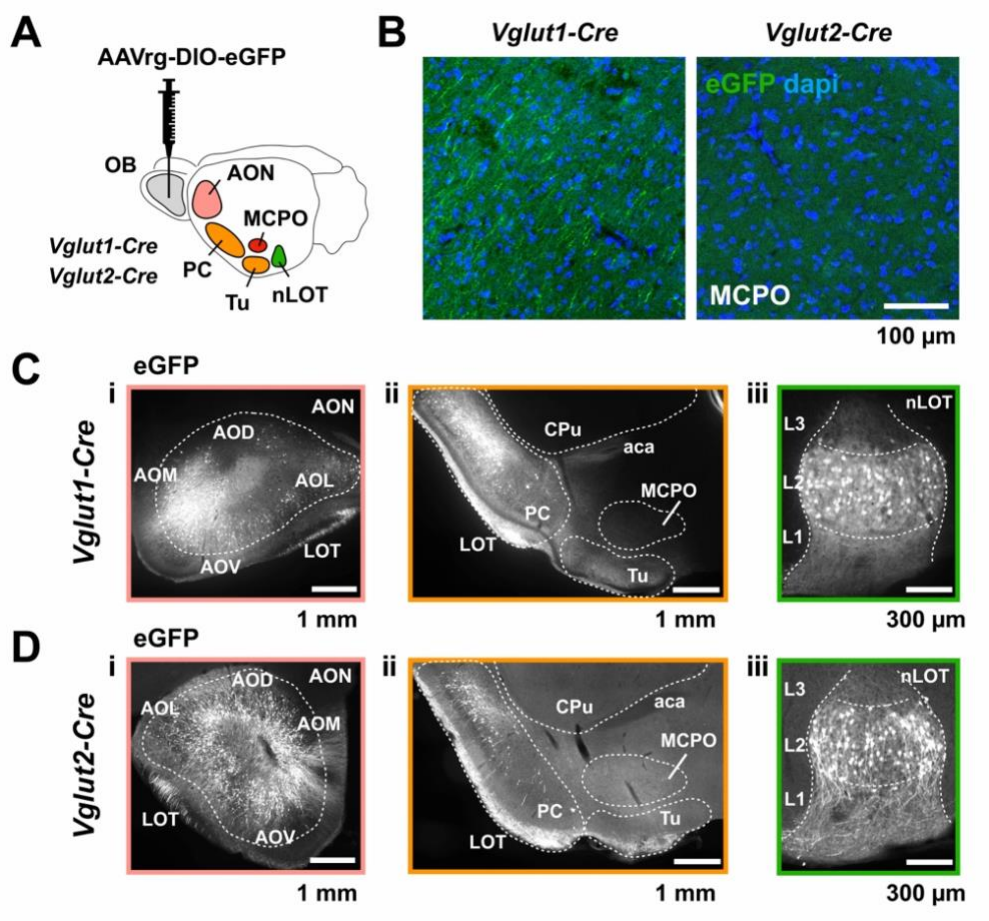

Fig. 2-2: *The olfactory bulb does not receive glutamatergic inputs from the MCPO*

(A) Diagram showing the strategy used to label potential OB projecting glutamatergic neurons. The Cre-dependent retrograde AAVrg-DIO-eGFP virus was injected into the OB of *Vglut-1 Cre* or *Vglut-2* mice. Different brain regions were examined using confocal microscopy. AON, anterior olfactory nucleus; PC, piriform cortex; MCPO, magnocellular preoptic area; Tu, olfactory tubercle; nLOT, nucleus of the lateral olfactory tract. **(B)** Confocal image of the MCPO in *Vglut-1 Cre* (left) and *Vglut-2 Cre* (right) mice injected with the retrograde virus in the OB. These representative images show no retrogradely labeled cells in the MPCO. **(C) i**, Coronal section of AON obtained from a *Vglut-1 Cre* mouse injected in the OB with the AAVrg-DIO-eGFP virus. Retrolabeled Vglut1 neurons are observed across different areas of the AON. AOM: AON medial, AOD: AON dorsal, AOL: AON lateral, AOV: AON ventral. **ii**, Coronal section of BF containing retrolabeled Vglut1 neurons in the PC. As expected, the Tu did not contain retrolabeled neurons. **iii,** Coronal section of nLOT containing abundant retrogradely transduced Vglut1 neurons. **(D)** Retrolabeled Vglut2 neurons across multiple brain areas as shown in panel **C**.

Supplementary figure Appendix A

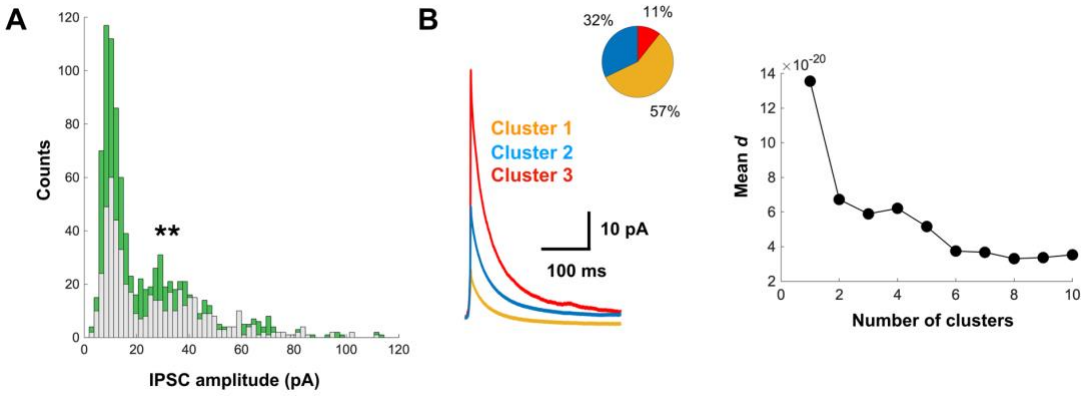

Fig. 2-1: *Spontaneous IPSCs in GCs can be sorted into three populations*

(A) Amplitude distributions of sIPSCs, before (light gray) and after Mus application (green, $p < 0.01$). Mus produces a relatively larger increase in events of smaller amplitude. **(B)** Left, sIPSC waveforms were clustered into three populations using the k-means method. Overlay of the average waveform obtained from the arithmetic mean of all sIPSCs assigned to a particular cluster (cluster 1: n= 808, amplitude 13.9 ± 6.3 pA, rise time 3.2 ± 2.7 ms, decay time 62.5 ± 35.4 ms; cluster 2: n= 453, amplitude 28.6 ± 8.3 pA, rise time 1.7 ± 1.4 ms, decay time 79.5 ± 36.3 ms; cluster 3: n= 150, amplitude 55.2 ± 15.8 pA, rise time 1.3 ± 0.3 ms, decay time 74 ± 29.3). The percentage of events assigned to each of the three clusters is shown in the pie chart. Right, dot plot of the mean *d* value obtained while varying the number of clusters used to determine the number of clusters.

Supplementary tables

Table S1. *Odor set used to examine the response profile of boutons in the OB*

Odor index	Odor name
1	p-anisaldehyde
2	Heptanal
3	Ethyl tiglate
4	Allyl tiglate
5	Ethyl propionate
6	Ethyl butyrate
7	Ethyl valerate
8	Isoamyl acetate
9	Propyl tiglate
10	Phenyl ethyl acetate
11	Propyl butyrate
12	Hexanal
13	Acetophenone
14	Valeraldehyde
15	Gamma terpinene
16	2,4 decadienal

Table S2. *Odors used to assess the effect of concentration on response profile*

Odor index	Odor name
1	Ethyl tiglate
2	Isoamyl acetate
3	Valeraldehyde
4	Ethyl valerate
5	Heptanal

Bibliography

Abraham NM, Egger V, Shimshek DR, Renden R, Fukunaga I, Sprengel R, Seeburg PH, Klugmann M, Margrie TW, Schaefer AT, Kuner T (2010) Synaptic Inhibition in the Olfactory Bulb Accelerates Odor Discrimination in Mice. Neuron 65:399–411.

Adrian ED (1942) Olfactory reactions in the brain of the hedgehog. J Physiol 100:459–473.

Anaclet C, Pedersen NP, Ferrari LL, Venner A, Bass CE, Arrigoni E, Fuller PM (2015) Basal forebrain control of wakefulness and cortical rhythms. Nat Commun 6:1–14.

Antal M, Acuna-Goycolea C, Todd Pressler R, Blitz DM, Regehr WG (2010) Cholinergic activation of M2 receptors leads to context- dependent modulation of feedforward inhibition in the visual thalamus. PLoS Biol 8.

Araneda RC, Firestein S (2006) Adrenergic enhancement of inhibitory transmission in the accessory olfactory bulb. J Neurosci 26:3292–3298.

Araneda RC, Kini AD, Firestein S (2000) The molecular receptive range of an odorant receptor. Nat Neurosci 3:1248–1255.

Araneda RC, Peterlin Z, Zhang X, Chesler A, Firestein S (2004) A pharmacological profile of the aldehyde receptor repertoire in rat olfactory epithelium. J Physiol 555:743–756.

Araneda RC, Smith R (2010) Cholinergic modulation of neuronal excitability in the accessory olfactory bulb. J Neurophysiol.

Arevian AC, Kapoor V, Urban NN (2008) Activity-dependent gating of lateral inhibition in the mouse olfactory bulb. Nat Neurosci 11:80–87.

Armstrong BCM, Gilly WF (1992) Access Resistance and Space Clamp Problems Associated with Whole-Cell Patch Clamping. Methods 207.

Arnson HA, Strowbridge BW (2017) Spatial Structure of Synchronized Inhibition in the Olfactory Bulb. J Neurosci 37:10468–10480.

Aroniadou-Anderjaska V, Zhou FM, Priest C a, Ennis M, Shipley MT (2000) Tonic and synaptically evoked presynaptic inhibition of sensory input to the rat olfactory bulb via GABA(B) heteroreceptors. J Neurophysiol 84:1194–1203.

Aston-Jones G, Cohen JD (2005) An integrative theory of locus coeruleus-norepinephrine function: Adaptive gain and optimal performance. Annu Rev Neurosci 28:403–450.

Atluri PP, Regehr WG (1998) Delayed release of neurotransmitter from cerebellar granule cells. J Neurosci 18:8214–8227.

Aungst JL, Heyward PM, Puche AC, Karnup S V, Hayar A, Szabo G, Shipley MT (2003) Centre-surround inhibition among olfactory bulb glomeruli. Nature 426:623–629.

Ballinger EC, Ananth M, Talmage DA, Role LW (2016) Basal Forebrain Cholinergic Circuits and Signaling in Cognition and Cognitive Decline. Neuron 91:1199–1218.

Balu R, Larimer P, Strowbridge BW (2004) Phasic stimuli evoke precisely timed spikes in intermittently discharging mitral cells. J Neurophysiol 92:743–753.

Balu R, Pressler RT, Strowbridge BW (2007) Multiple Modes of Synaptic Excitation of Olfactory Bulb Granule Cells. J Neurosci 27:5621–5632.

Banerjee A, Marbach F, Anselmi F, Koh MS, Davis MB, Garcia da Silva P, Delevich K, Oyibo HK, Gupta P, Li B, Albeanu DF (2015) An Interglomerular Circuit Gates Glomerular Output and Implements Gain Control in the Mouse Olfactory Bulb. Neuron 87:193–207.

Banks MI, Li TB, Pearce R a (1998) The synaptic basis of GABAA,slow. J Neurosci 18:1305–1317.

Bartos M, Vida I, Frotscher M, Meyer A, Monyer H, Geiger JRP, Jonas P (2002) Fast synaptic inhibition promotes synchronized gamma oscillations in hippocampal interneuron networks. Proc Natl Acad Sci 99:13222–13227.

Basu J, Zaremba JD, Cheung SK, Hitti FL, Zemelman B V, Losonczy A, Siegelbaum SA (2016) Gating of hippocampal activity, plasticity, and memory by entorhinal cortex long-range inhibition. 351.

Behrends JC, Bruggencate G (1993) Modulation of Synaptic Inhibition in the Guinea Pig Hippocampus In Vitro : Excitation of GABAergic Interneurons and Inhibition of GABA-Release. 69:5–8.

Beshel J, Kopell N, Kay LM (2007) Olfactory Bulb Gamma Oscillations Are Enhanced with Task Demands. J Neurosci 27:8358–8365.

Böhm E, Brunert D, Rothermel M (2020) Input dependent modulation of olfactory bulb activity by HDB GABAergic projections. Sci Rep 10:1–15.

Bokil H, Andrews P, Kulkarni JE, Mehta S, Mitra PP (2010) Chronux: A platform for analyzing neural signals. J Neurosci Methods 192:146–151.

Borhegyi Z, Varga V, Szilágyi N, Fabo D, Freund TF (2004) Phase segregation of medial septal GABAergic neurons during hippocampal theta activity. J Neurosci 24:8470–8479.

Boyd AM, Kato HK, Komiyama T, Isaacson JS (2015) Broadcasting of Cortical Activity to the Olfactory Bulb. Cell Rep 10:1032–1039.

Boyd AM, Sturgill JF, Poo C, Isaacson JS (2012) Cortical Feedback Control of Olfactory Bulb Circuits. Neuron 76:1161–1174.

Bozza T, McGann JP, Mombaerts P, Wachowiak M (2004) In vivo imaging of neuronal

activity by targeted expression of a genetically encoded probe in the mouse. Neuron 42:9–21.

Brennan PA (2001) The vomeronasal system. Cell Mol Life Sci 58:546–555.

Brombas A, Fletcher LN, Williams SR (2014) Activity-dependent modulation of layer 1 inhibitory neocortical circuits by acetylcholine. J Neurosci 34:1932–1941.

Brown RE, McKenna JT (2015) Turning a negative into a positive: Ascending GABAergic control of cortical activation and arousal. Front Neurol 6.

Buck L, Axel R (1991) A novel multigene family may encode odorant receptors: a molecular basis for odour recognition. Cell 65:175–187.

Burton SD, Urban NN (2015) Rapid Feedforward Inhibition and Asynchronous Excitation Regulate Granule Cell Activity in the Mammalian Main Olfactory Bulb. J Neurosci 35:14103–14122.

Butts DA, Weng C, Jin J, Yeh CI, Lesica NA, Alonso JM, Stanley GB (2007) Temporal precision in the neural code and the timescales of natural vision. Nature 449:92–95.

Buzsáki G, Chrobak JJ (1995) Temporal structure in spatially organized neuronal ensembles: a role for interneuronal networks. Curr Opin Neurobiol 5:504–510.

Caputi A, Melzer S, Michael M, Monyer H (2013) The long and short of GABAergic neurons. Curr Opin Neurobiol 23:179–186.

Cardin JA (2018) Inhibitory Interneurons Regulate Temporal Precision and Correlations in Cortical Circuits. Trends Neurosci 41:689–700.

Cardona A, Saalfeld S, Schindelin J, Arganda-Carreras I, Preibisch S, Longair M, Tomancak P, Hartenstein V, Douglas RJ (2012) TrakEM2 software for neural circuit reconstruction. PLoS One 7.

Case DT, Burton SD, Gedeon JY, Williams SPG, Urban NN, Seal RP (2017) Layer- and cell type-selective co-transmission by a basal forebrain cholinergic projection to the olfactory bulb. Nat Commun 8.

Castillo PE, Carleton A, Vincent J-DD, Lledo PM (1999) Multiple and opposing roles of cholinergic transmission in the main olfactory bulb. J Neurosci 19:9180–9191.

Chapuis J, Wilson DA (2013) Cholinergic modulation of olfactory pattern separation. Neurosci Lett 545:50–53.

Chen TW, Wardill TJ, Sun Y, Pulver SR, Renninger SL, Baohan A, Schreiter ER, Kerr RA, Orger MB, Jayaraman V, Looger LL, Svoboda K, Kim DS (2013) Ultrasensitive fluorescent proteins for imaging neuronal activity. Nature 499:295–300.

Christie JM, Schoppa NE, Westbrook GL (2001) Tufted cell dendrodendritic inhibition in the olfactory bulb is dependent on NMDA receptor activity. J Neurophysiol 85:169–173.

Cullinan WE, Záborszky L (1991) Organization of ascending hypothalamic projections to the rostral forebrain with special reference to the innervation of cholinergic projection neurons. J Comp Neurol 306:631–667.

Cury KM, Uchida N (2010) Robust Odor Coding via Inhalation-Coupled Transient Activity in the Mammalian Olfactory Bulb. Neuron 68:570–585.

D'Souza RD, Parsa P V., Vijayaraghavan S (2013) Nicotinic receptors modulate olfactory bulb external tufted cells via an excitation-dependent inhibitory mechanism. J Neurophysiol 110:1544–1553.

Day HEW, Campeau S, Watson SJ, Akil H (1997) Distribution of α(1a)-, α(1b)- and α(1d)-adrenergic receptor mRNA in the rat brain and spinal cord. J Chem Neuroanat

13:115–139.

De Olmos J, Hardy H, Heimer L (1978) The afferent connections of the main and the accessory olfactory bulb formations in the rat: An experimental HRP study. J Comp Neurol 181:213–244.

Dodge FA, Miledi R, Rahamimoff R (1969) Strontium and quantal release of transmitter at the neuromuscular junction. J Physiol 200:267–283.

Doty RL, Bagla R, Kim N (1998) Physostigmine enhances performance on an odor mixture discrimination test. Physiol Behav 65:801–804.

Doucette W, Milder J, Restrepo D (2007) Adrenergic modulation of olfactory bulb circuitry affects odor discrimination. Learn Mem 14:539–547.

Doyle WI, Meeks JP (2017) Heterogeneous effects of norepinephrine on spontaneous and stimulus-driven activity in the male accessory olfactory bulb. J Neurophysiol 117:1342–1351.

Dulac C, Axel R (1995) A novel family of genes encoding putative pheromone receptors in mammals. Cell 83:195–206.

Dulac C, Torello AT (2003) Molecular detection of pheromone signals in mammals: From genes to behaviour. Nat Rev Neurosci 4:551–562.

Dulac C, Wagner S (2006) Genetic Analysis of Brain Circuits Underlying Pheromone Signaling. Annu Rev Genet 40:449–467.

Egger V, Svoboda K, Mainen ZF (2003) Mechanisms of lateral inhibition in the olfactory bulb: efficiency and modulation of spike-evoked calcium influx into granule cells. J Neurosci 23:7551–7558.

Egger V, Svoboda K, Mainen ZF (2005) Dendrodendritic synaptic signals in olfactory bulb

granule cells: Local spine boost and global low-threshold spike. J Neurosci 25:3521–3530.

Eisenberg JF, Kleiman DG (1972) Olfactory Communication in Mammals. Annu Rev Ecol Syst 3:1–32.

Ennis M, Zhou FM, Ciombor KJ, Aroniadou-Anderjaska V, Hayar A, Borrelli E, Zimmer LA, Margolis F, Shipley MT (2001) Dopamine D2 receptor-mediated presynaptic inhibition of olfactory nerve terminals. J Neurophysiol 86:2986–2997.

Eyre MD, Antal M, Nusser Z (2008) Distinct deep short-axon cell subtypes of the main olfactory bulb provide novel intrabulbar and extrabulbar GABAergic connections. J Neurosci 28:8217–8229.

Eyre MD, Renzi M, Farrant M, Nusser Z (2012) Setting the time course of inhibitory synaptic currents by mixing multiple GABA(A) receptor α subunit isoforms. J Neurosci 32:5853–5867.

Faul F, Erdfelder E, Buchner A, Lang AG (2009) Statistical power analyses using G*Power 3.1: Tests for correlation and regression analyses. Behav Res Methods 41:1149–1160.

Fedchyshyn MJ, Wang L-Y (2007) Activity-dependent changes in temporal components of neurotransmission at the juvenile mouse calyx of Held synapse. J Physiol 581:581–602.

Feng L, Zhao T, Kim J (2015) Neutube 1.0: A new design for efficient neuron reconstruction software based on the swc format. eNeuro 2:ENEURO.0049-14.2014.

Florin-Lechner SM, Druhan JP, Aston-Jones G, Valentino RJ (1996) Enhanced norepinephrine release in prefrontal cortex with burst stimulation of the locus coeruleus. Brain Res 742:89–97.

Foote SL, Aston-Jones G, Bloom FE (1980) Impulse activity of locus coeruleus neurons in awake rats and monkeys is a function of sensory stimulation and arousal. Proc Natl Acad Sci U S A 77:3033–3037.

Freund TF, Antal M (1988) GABA-containing neurons in the septum control inhibitory interneurons in the hippocampus. Nature 336:170–173.

Freund TF, Gulyás AI (1991) GABAergic Interneurons Containing Calbindin D28k or Somatostatin Are Major Targets of GABAergic Basal Forebrain Afferents in the Rat Neocortex. J Comp Neurol 314:187–199.

Freund TF, Meskenaite V (1992) gamma-Aminobutyric acid-containing basal forebrain neurons innervate inhibitory interneurons in the neocortex. Proc Natl Acad Sci U S A 89:738–742.

Fuchs EC, Neitz A, Pinna R, Melzer S, Caputi A, Monyer H (2016) Local and Distant Input Controlling Excitation in Layer II of the Medial Entorhinal Cortex. Neuron 89:194–208.

Fukunaga I, Berning M, Kollo M, Schmaltz A, Schaefer AT (2012) Two Distinct Channels of Olfactory Bulb Output. Neuron 75:320–329.

Fukunaga I, Herb JT, Kollo M, Boyden ES, Schaefer AT (2014) Independent control of gamma and theta activity by distinct interneuron networks in the olfactory bulb. Nat Neurosci 17:1208–1216.

Gaykema RPA, Zaborszky L (1997) Parvalbumin-containing neurons in the basal forebrain receive direct input from the substantia nigra-ventral tegmental area. Brain Res 747:173–179.

Ghatpande AS, Sivaraaman K, Vijayaraghavan S (2006) Store calcium mediates

cholinergic effects on mIPSCs in the rat main olfactory bulb. J Neurophysiol 95:1345–1355.

Gil Z, Connors BW, Amitai Y (1997) Differential regulation of neocortical synapses by neuromodulators and activity. Neuron 19:679–686.

Gire DH, Schoppa NE (2009) Control of on/off glomerular signaling by a local GABAergic microcircuit in the olfactory bulb. J Neurosci 29:13454–13464.

Goda Y, Stevens CF (1994) Two components of transmitter release at a central synapse. Proc Natl Acad Sci U S A 91:12942–12946.

Gonzalez-Sulser A, Parthier D, Candela A, McClure C, Pastoll H, Garden D, Sürmeli G, Nolan MF (2014) Gabaergic projections from the medial septum selectively inhibit interneurons in the medial entorhinal cortex. J Neurosci 34:16739–16743.

Gracia-Llanes FJ, Crespo C, Blasco-Ibáñez JM, Nacher J, Varea E, Rovira-Esteban L, Martínez-Guijarro FJ (2010) GABAergic basal forebrain afferents innervate selectively GABAergic targets in the main olfactory bulb. Neuroscience 170:913–922.

Gritti I, Mainville L, Mancia M, Jones BE (1997) GABAergic and Other Noncholinergic Basal Forebrain Neurons , Together With Cholinergic Neurons, Project to the Mesocortex and Isocortex in the Rat. J Comp Neurol 177:163–177.

Gritti I, Manns ID, Mainville L, Jones BE (2003) Parvalbumin, calbindin, or calretinin in cortically projecting and GABAergic, cholinergic, or glutamatergic basal forebrain neurons of the rat. J Comp Neurol 458:11–31.

Gschwend O, Abraham NM, Lagier S, Begnaud F, Rodriguez I, Carleton A (2015) Neuronal pattern separation in the olfactory bulb improves odor discrimination

learning. Nat Neurosci 18:1474–1482.

Gulyás AI, Görcs TJ, Freund TF (1990) Innervation of different peptide-containing neurons in the hippocampus by gabaergic septal afferents. Neuroscience 37:31–44.

Gulyás AI, Seress L, Tóth K, Acsády L, Antal M, Freund TF (1991) Septal GABAergic neurons innervate inhibitory interneurons in the hippocampus of the macaque monkey. Neuroscience 41:381–390.

Gutkin B, Ermentrout GB, Rudolph M (2003) Spike generating dynamics and the conditions for spike-time precision in cortical neurons. J Comput Neurosci 15:91–103.

Hagiwara A, Pal SK, Sato TF, Wienisch M, Murthy VN (2012) Optophysiological analysis of associational circuits in the olfactory cortex. Front Neural Circuits 6:1–19.

Hamilton KA, Heinbockel T, Ennis M, Szabó G, Erdélyi F, Hayar A (2005) Properties of external plexiform layer interneurons in mouse olfactory bulb slices. Neuroscience 133:819–829.

Hangya B, Borhegyi Z, Szilágyi N, Freund TF, Varga V (2009) GABAergic neurons of the medial septum lead the hippocampal network during theta activity. J Neurosci 29:8094–8102.

Hangya B, Ranade SP, Lorenc M, Kepecs A (2015) Central cholinergic neurons are rapidly recruited by reinforcement feedback. Cell 162:1155–1168.

Hanson E, Brandel-Ankrapp KL, Arenkiel BR (2021) Dynamic Cholinergic Tone in the Basal Forebrain Reflects Reward-Seeking and Reinforcement During Olfactory Behavior. Front Cell Neurosci 15:1–14.

Hanson E, Swanson J, Arenkiel BR (2020) GABAergic Input From the Basal Forebrain

Promotes the Survival of Adult-Born Neurons in the Mouse Olfactory Bulb. Front Neural Circuits 14:1–12.

Hasselmo ME (1995) Neuromodulation and cortical function: modeling the physiological basis of behavior. Behav Brain Res 67:1–27.

Hasselmo ME, Bower JM (1992) Cholinergic suppression specific to intrinsic not afferent fiber synapses in rat piriform (olfactory) cortex. J Neurophysiol 67:1222–1229.

Hasselmo ME, Sarter M (2011) Modes and models of forebrain cholinergic neuromodulation of cognition. Neuropsychopharmacology 36:52–73.

Hasselmo ME, Schnell E (1994) Laminar selectivity of the cholinergic suppression of synaptic transmission in rat hippocampal region CA1: Computational modeling and brain slice physiology. J Neurosci 14:3898–3914.

Hayar A (2004) Olfactory Bulb Glomeruli: External Tufted Cells Intrinsically Burst at Theta Frequency and Are Entrained by Patterned Olfactory Input. J Neurosci 24:1190–1199.

Hayar A, Heyward PM, Heinbockel T, Shipley MT, Ennis M (2001) Direct excitation of mitral cells via activation of α1-noradrenergic receptors in rat olfactory bulb slices. J Neurophysiol 86:2173–2182.

Hefft S, Jonas P (2005) Asynchronous GABA release generates long-lasting inhibition at a hippocampal interneuron-principal neuron synapse. Nat Neurosci 8:1319–1328.

Hein L (2006) Adrenoceptors and signal transduction in neurons. Cell Tissue Res 326:541–551.

Hellier JL, Arevalo NL, Smith L, Xiong KN, Restrepo D (2012) α7-nicotinic acetylcholine receptor: Role in early odor learning preference in mice. PLoS One 7:1–7.

Henny P, Jones BE (2008) Projections from basal forebrain to prefrontal cortex comprise cholinergic, GABAergic and glutamatergic inputs to pyramidal cells or interneurons. Eur J Neurosci 27:654–670.

Herrada G, Dulac C (1997) A novel family of putative pheromone receptors in mammals with a topographically organized and sexually dimorphic distribution. Cell 90:763–773.

Hildebrand JG, Shepherd GM (1997) Mechanisms of olfactory discrimination: Converging evidence for common principles across phyla. Annu Rev Neurosci 20:595–631.

Huang L, Garcia I, Jen HI, Arenkiel BR (2013) Reciprocal connectivity between mitral cells and external plexiform layer interneurons in the mouse olfactory bulb. Front Neural Circuits 7:1–16.

Huntsman MM, Porcello DM, Homanics GE, DeLorey TM, Huguenard JR (1999) Reciprocal inhibitory connections and network synchrony in the mammalian thalamus. Science (80-) 283:541–543.

Hur EE, Edwards RH, Rommer E, Zaborszky L (2009) Vesicular glutamate transporter 1 and vesicular glutamate transporter 2 synapses on cholinergic neurons in the sublenticular gray of the rat basal forebrain: a double-label electron microscopic study. Neuroscience 164:1721–1731.

Hur EE, Zaborszky L (2005) Vglut2 afferents to the medial prefrontal and primary somatosensory cortices: A combined retrograde tracing in situ hybridization. J Comp Neurol 483:351–373.

Hurst RS, Hajós M, Raggenbass M, Wall TM, Higdon NR, Lawson JA, Rutherford-Root KL, Berkenpas MB, Hoffmann WE, Piotrowski DW, Groppi VE, Allaman G, Ogier

R, Bertrand S, Bertrand D, Arneric SP (2005) A novel positive allosteric modulator of the α7 neuronal nicotinic acetylcholine receptor: In vitro and in vivo characterization. J Neurosci 25:4396–4405.

Igarashi KM, Ieki N, An M, Yamaguchi Y, Nagayama S, Kobayakawa K, Kobayakawa R, Tanifuji M, Sakano H, Chen WR, Mori K (2012) Parallel Mitral and Tufted Cell Pathways Route Distinct Odor Information to Different Targets in the Olfactory Cortex. J Neurosci 32:7970–7985.

in 't Zandt EE, Cansler HL, Denson HB, Wesson DW (2019) Centrifugal Innervation of the Olfactory Bulb: A Reappraisal. Eneuro 6:ENEURO.0390-18.2019.

Inagaki S, Iwata R, Iwamoto M, Imai T (2020) Widespread Inhibition, Antagonism, and Synergy in Mouse Olfactory Sensory Neurons In Vivo. Cell Rep 31:107814.

Isaacson JS, Scanziani M (2011) How inhibition shapes cortical activity. Neuron 72:231–243.

Isaacson JS, Strowbridge BW (1998) Olfactory reciprocal synapse: dendritic signalling in the CNS. Neuron 20:749–761.

James NM, Gritton HJ, Kopell N, Sen K, Han X (2019) Muscarinic receptors regulate auditory and prefrontal cortical communication during auditory processing. Neuropharmacology 144:155–171.

Jia C, Chen WR, Shepherd GM (1999) Synaptic organization and neurotransmitters in the rat accessory olfactory bulb. J Neurophysiol 81:345–355.

Jia C, Halpern M (1996) Subclasses of vomeronasal receptor neurons: Differential expression of G proteins (Giα2 and Goα) and segregated projections to the accessory olfactory bulb. Brain Res 719:117–128.

Jiang L, Kundu S, Lederman JDD, López-Hernández GYY, Ballinger ECC, Wang S, Talmage DAA, Role LWW (2016) Cholinergic Signaling Controls Conditioned Fear Behaviors and Enhances Plasticity of Cortical-Amygdala Circuits. Neuron 90:1057–1070.

Jinno S, Klausberger T, Marton LF, Dalezios Y, Roberts JDB, Fuentealba P, Bushong EA, Henze D, Buzsáki G, Somogyi P (2007) Neuronal diversity in GABAergic long-range projections from the hippocampus. J Neurosci 27:8790–8804.

Johnson BA, Leon M (2000) Modular representations of odorants in the glomerular layer of the rat olfactory bulb and the effects of stimulus concentration. J Comp Neurol 422:496–509.

Junek S, Kludt E, Wolf F, Schild D (2010) Olfactory Coding with Patterns of Response Latencies. Neuron 67:872–884.

Kaeser PS, Regehr WG (2014) Molecular Mechanisms for Synchronous, Asynchronous, and Spontaneous Neurotransmitter Release. Annu Rev Physiol 76:333–363.

Kay LM (2014) Circuit oscillations in odor perception and memory. Prog Brain Res 208:223–251.

Kay LM (2015) Olfactory system oscillations across phyla. Curr Opin Neurobiol 31:141–147.

Kay LM, Beshel J, Brea J, Martin C, Rojas-Líbano D, Kopell N (2009) Olfactory oscillations: the what, how and what for. Trends Neurosci 32:207–214.

Keller GB, Mrsic-Flogel TD (2018) Predictive Processing: A Canonical Cortical Computation. Neuron 100:424–435.

Kepecs A, Fishell G (2014) Interneuron cell types are fit to function. Nature 505:318–326.

Kepecs A, Uchida N, Mainen ZF (2006) The sniff as a unit of olfactory processing. Chem Senses 31:167–179.

Keverne EB (1999) The Vomeronasal Organ. Science (80-) 286:720.

Kim T, Thankachan S, McKenna JT, Mcnally JM, Yang C, Choi JH, Chen L, Kocsis B, Strecker RE, Basheer R, Brown RE, Hyun J (2015a) Cortically projecting basal forebrain parvalbumin neurons regulate cortical gamma band oscillations. Proc Natl Acad Sci 112:E2848–E2848.

Kim Y, Venkataraju KU, Pradhan K, Mende C, Taranda J, Turaga SC, Arganda-Carreras I, Ng L, Hawrylycz MJ, Rockland KS, Seung HS, Osten P (2015b) Mapping social behavior-induced brain activation at cellular resolution in the mouse. Cell Rep 10:292–305.

Kim Y, Yang GR, Pradhan K, Venkataraju KU, Bota M, García del Molino LC, Fitzgerald G, Ram K, He M, Levine JM, Mitra P, Huang ZJ, Wang XJ, Osten P (2017) Brain-wide Maps Reveal Stereotyped Cell-Type-Based Cortical Architecture and Subcortical Sexual Dimorphism. Cell 171:456-469.e22.

Kimura F (2000) Cholinergic modulation of cortical function: A hypothetical role in shifting the dynamics in cortical network. Neurosci Res 38:19–26.

Kimura F, Baughman RW (1997) Distinct muscarinic receptor subtypes suppress excitatory and inhibitory synaptic responses in cortical neurons. J Neurophysiol 77:709–716.

Kiyokage E, Pan Y-Z, Shao Z, Kobayashi K, Szabo G, Yanagawa Y, Obata K, Okano H, Toida K, Puche AC, Shipley MT (2010) Molecular identity of periglomerular and short axon cells. J Neurosci 30:1185–1196.

Klein S, Staring M, Murphy K, Viergever MA, Pluim JPW (2010) Elastix: A toolbox for intensity-based medical image registration. IEEE Trans Med Imaging 29:196–205.

Korotkova T, Fuchs EC, Ponomarenko A, von Engelhardt J, Monyer H (2010) NMDA Receptor Ablation on Parvalbumin-Positive Interneurons Impairs Hippocampal Synchrony, Spatial Representations, and Working Memory. Neuron 68:557–569.

Kuglin CD, Hines DC (1975) The phase correlation image alignment method. IEEE Int Conf Cybern Soc 6:163–165.

Lagier S, Carleton A, Lledo PM (2004) Interplay between Local GABAergic Interneurons and Relay Neurons Generates Oscillations in the Rat Olfactory Bulb. J Neurosci 24:4382–4392.

Lagier S, Panzanelli P, Russo RE, Nissant A, Bathellier B, Sassoè-Pognetto M, Fritschy J, Lledo PM (2007) GABAergic inhibition at dendrodendritic synapses tunes gamma oscillations in the olfactory bulb. Proc Natl Acad Sci U S A 104:7259–7264.

Laurent G, Davidowitz H (1994) Encoding of Olfactory Information with Oscillating Neural Assemblies. Science (80-) 265:1872–1875.

Laurent G, Wehr M, Davidowitz H (1996) Temporal representations of odors in an olfactory network. J Neurosci 16:3837–3847.

Laurie DJ, Seeburg PH, Wisden W (1992) The distribution of 13 GABA(A) receptor subunit mRNAs in the rat brain. II. Olfactory bulb and cerebellum. J Neurosci 12:1063–1076.

Lee SH, Dan Y (2012) Neuromodulation of Brain States. Neuron 76:209–222.

Leong ATL, Chan RW, Gao PP, Chan YS, Tsia KK, Yung WH, Wu EX (2016) Long-range projections coordinate distributed brain-wide neural activity with a specific

spatiotemporal profile. Proc Natl Acad Sci U S A 113:E8306–E8315.

Li WL, Chu MW, Wu A, Suzuki Y, Imayoshi I, Komiyama T (2018) Adult-born neurons facilitate olfactory bulb pattern separation during task engagement. Elife 7:1–26.

Liman ER (1996) Pheromone transduction in the vomeronasal organ. Curr Opin Neurobiol 6:487–493.

Lin S-C, Brown RE, Hussain Shuler MG, Petersen CCH, Kepecs A (2015) Optogenetic Dissection of the Basal Forebrain Neuromodulatory Control of Cortical Activation, Plasticity, and Cognition. J Neurosci 35:13896–13903.

Linster C, Cleland TA (2002) Cholinergic modulation of sensory representations in the olfactory bulb. Neural Networks 15:709–717.

Liu S, Shao Z, Puche AC, Wachowiak M, Rothermel M, Shipley MT (2015) Muscarinic receptors modulate dendrodendritic inhibitory synapses to sculpt glomerular output. J Neurosci 35:5680–5692.

Lledo PM, Gheusi G, Vincent JD (2005) Information processing in the mammalian olfactory system. Physiol Rev 85:281–317.

Luiten PGM, Gaykema RPA, Traber J, Spencer DG (1987) Cortical projection patterns of magnocellular basal nucleus subdivisions as revealed by anterogradely transported Phaseolus vulgaris leucoagglutinin. Brain Res 413:229–250.

Luskin MB, Price JL (1983) The topographic organization of associational fibers of the olfactory system in the rat, including centrifugal fibers to the olfactory bulb. J Comp Neurol 216:264–291.

Ma L, Qiu Q, Gradwohl S, Scott A, Yu EQ, Alexander R, Wiegraebe W, Yu CR (2012) Distributed representation of chemical features and tunotopic organization of

glomeruli in the mouse olfactory bulb. Proc Natl Acad Sci U S A 109:5481–5486.

Ma M, Luo M (2012) Optogenetic activation of basal forebrain cholinergic neurons modulates neuronal excitability and sensory responses in the main olfactory bulb. J Neurosci 32:10105–10116.

MacLeod KM, Laurent G (1996) Distinct mechanisms for synchronization and temporal patterning of odor-encoding\rneural assemblies. Science (80-) 274:976–979.

Macrides F, Chorover S (1972) Olfactory Bulb Units: Activity Correlated with Inhalation Cycles and Odor Quality. Science (80-) 175.

Mainen ZF, Sejnowski TJ (1995) Reliability of spike timing in neocortical neurons. Science 268:1503–1506.

Manella LC, Petersen N, Linster C (2017) Stimulation of the locus ceruleus modulates signal-to-noise ratio in the olfactory bulb. J Neurosci 37:11605–11615.

Markopoulos F, Rokni D, Gire DH, Murthy VN (2012) Functional properties of cortical feedback projections to the olfactory bulb. Neuron 76:1175–1188.

Martin C, Beshel J, Kay LM (2007) An Olfacto-Hippocampal Network Is Dynamically Involved in Odor-Discrimination Learning. J Neurophysiol 98:2196–2205.

Martínez-Guijarro FJ, Freund TF (1992) GABA-immunoreactive basal forebrain afferents innervate GABA-immunoreactive non-pyramidal cells in the cerebral cortex of the lizard podarcis hispanica. Neuroscience 51:425–437.

Matsutani S (2010) Trajectory and terminal distribution of single centrifugal axons from olfactory cortical areas in the rat olfactory bulb. Neuroscience 169:436–448.

Matsutani S, Yamamoto N (2008) Centrifugal innervation of the mammalian olfactory bulb. Anat Sci Int 83:218–227.

Mazo C, Lepousez G, Nissant A, Valley MT, Lledo PM (2016) GABAB Receptors Tune Cortical Feedback to the Olfactory Bulb. J Neurosci 36:8289–8304.

Mazo C, Saha S, Nissant A, Peroni E, Lledo PM, Lepousez G (2020) Long-range GABAergic projections contribute to cortical feedback control of sensory processing. bioRxiv.

McDonald BJ, Amato A, Connolly CN, Benke D, Moss SJ, Smart TG (1998) Adjacent phosphorylation sites on GABAA receptor β subunits determine regulation by cAMP-dependent protein kinase. Nat Neurosci 1:23–28.

McKenna JT, Yang C, Bellio T, Anderson-Chernishof MB, Gamble MC, Hulverson A, McCoy JG, Winston S, Hodges E, Katsuki F, McNally JM, Basheer R, Brown RE (2021) Characterization of basal forebrain glutamate neurons suggests a role in control of arousal and avoidance behavior. Brain Struct Funct 226:1755–1778.

McKenna JT, Yang C, Franciosi S (2013) Distribution and intrinsic membrane properties of basal forebrain GABAergic and par albumin neurons in the mouse. J Comp Neurol 521:1225–1250.

McLean JH, Shipley MT, Nickell WT, Aston-Jones G, Reyher CKH (1989) Chemoanatomical organization of the noradrenergic input from locus coeruleus to the olfactory bulb of the adult rat. J Comp Neurol 285:339–349.

Melzer S, Michael M, Caputi A, Eliava M, Fuchs EC, Whittington M a., Monyer H (2012) Long-Range–Projecting GABAergic Neurons Modulate Inhibition in Hippocampus and Entorhinal Cortex. Science (80-) 335:1506–1510.

Melzer S, Monyer H (2020) Diversity and function of corticopetal and corticofugal GABAergic projection neurons. Nat Rev Neurosci 21:499–515.

Mohrhardt J, Nagel M, Fleck D, Ben-Shaul Y, Spehr M (2018) Signal detection and coding in the accessory olfactory system. Chem Senses 43:667–695.

Mombaerts P (2004) Odorant receptor gene choice in olfactory sensory neurons: The one receptor-one neuron hypothesis revisited. Curr Opin Neurobiol 14:31–36.

Mombaerts P, Wang F, Dulac C, Chao SK, Nemes A, Mendelsohn M, Edmondson J, Axel R (1996) Visualizing an olfactory sensory map. Cell 87:675–686.

Moreno MM, Bath K, Kuczewski N, Sacquet J, Didier A, Mandairon N (2012) Action of the noradrenergic system on adult-born cells is required for olfactory learning in mice. J Neurosci 32:3748–3758.

Mori K, Nagao H, Yoshihara Y (1999) The Olfactory Bulb : Coding and Processing of Odor Molecule Information. Science (80-) 286:711–715.

Moss SJ, Smart TG (2001) Constructing inhibitory synapses. Nat Rev Neurosci 2:240–250.

Moss SJ, Smart TG, Huganir RL (1992) Functional Modulation of GABAA receptors by cAMP-Dependent protein phosphorylation. Science (80-) 257:661–665.

Murphy GJ, Darcy DP, Isaacson JS (2005) Intraglomerular inhibition: signaling mechanisms of an olfactory microcircuit. Nat Neurosci 8:354–364.

Nagayama S, Homma R, Imamura F (2014) Neuronal organization of olfactory bulb circuits. Front Neural Circuits 8:1–19.

Nai Q, Dong HW, Linster C, Ennis M (2010) Activation of A1 and A2 noradrenergic receptors exert opposing effects on excitability of main olfactory bulb granule cells. Neuroscience 169:882–892.

Nakamura Y, Darnieder LM, Deeb TZ, Moss SJ (2015) Regulation of GABAARs by

phosphorylation. Adv Pharmacol 72:97–146.

Nunes D, Kuner T (2015) Disinhibition of olfactory bulb granule cells accelerates odour discrimination in mice. Nat Commun 6:8950.

Nunez-Parra A, Cea-Del Rio CA, Huntsman MM, Restrepo D (2020) The Basal Forebrain Modulates Neuronal Response in an Active Olfactory Discrimination Task. Front Cell Neurosci 14:1–14.

Nunez-Parra A, Maurer RK, Krahe K, Smith RS, Araneda RC (2013) Disruption of centrifugal inhibition to olfactory bulb granule cells impairs olfactory discrimination. Proc Natl Acad Sci U S A 110:14777–14782.

Nusser Z, Kay LM, Laurent G, Homanics GE, Mody I (2001) Disruption of GABAA receptors on GABAergic interneurons leads to increased oscillatory power in the olfactory bulb network. J Neurophysiol 86:2823–2833.

Nusser Z, Sieghart W, Mody I (1999) Differential regulation of synaptic GABA(A) receptors by cAMP-dependent protein kinase in mouse cerebellar and olfactory bulb neurones. J Physiol 521:421–435.

Oka Y, Omura M, Kataoka H, Touhara K (2004) Olfactory receptor antagonism between odorants. EMBO J 23:120–126.

Onoda N, Mori K (1980) Depth distribution of temporal firing patterns in olfactory bulb related to air-intake cycles. J Neurophysiol 44:29–39.

Osinski BL, Kay LM (2016) Granule cell excitability regulates gamma and beta oscillations in a model of the olfactory bulb dendrodendritic microcircuit. J Neurophysiol 116:522–539.

Oswald AM, Urban NN (2012) There and Back Again: The Corticobulbar Loop. Neuron

76:1045–1047.

Otazu GH, Chae H, Davis MB, Albeanu DF (2015) Cortical Feedback Decorrelates Olfactory Bulb Output in Awake Mice. Neuron 86:1461–1477.

Pandipati S, Gire DH, Schoppa NE (2010) Adrenergic receptor-mediated disinhibition of mitral cells triggers long-term enhancement of synchronized oscillations in the olfactory bulb. J Neurophysiol 104:665–674.

Pandipati S, Schoppa NE (2012) Age-dependent adrenergic actions in the main olfactory bulb that could underlie an olfactory-sensitive period. J Neurophysiol 108:1999–2007.

Paolini AG, McKenzie JS (1996) Lesions in the magnocellular preoptic nucleus decrease olfactory investigations in rats. Behav Brain Res 81:223–231.

Paolini AG, McKenzie JS (1997) Intracellular recording of magnocellular preoptic neuron responses to olfactory brain. Neuroscience 78:229–242.

Parikh V, Sarter M (2008) Cholinergic mediation of attention: Contributions of phasic and tonic increases in prefrontal cholinergic activity. Ann N Y Acad Sci 1129:225–235.

Patil MM, Hasselmo ME (1999) Modulation of inhibitory synaptic potentials in the piriform cortex. J Neurophysiol 81:2103–2118.

Paxinos G, Franklin K (2004) The Mouse Brain.

Petreanu L, Mao T, Sternson SM, Svoboda K (2009) The subcellular organization of neocortical excitatory connections. Nature 457:1142–1145.

Petrovich GD, Canteras NS, Swanson LW (2001) Combinatorial amygdalar inputs to hippocampal domains and hypothalamic behavior systems. Brain Res Rev 38:247–289.

Pfeffer CK, Xue M, He M, Huang ZJ, Scanziani M (2013) Inhibition of inhibition in visual cortex: the logic of connections between molecularly distinct interneurons. Nat Neurosci 16:1068–1076.

Pfister P, Smith BC, Evans BJ, Brann JH, Trimmer C, Sheikh M, Arroyave R, Reddy G, Jeong HY, Raps DA, Peterlin Z, Vergassola M, Rogers ME (2020) Odorant Receptor Inhibition Is Fundamental to Odor Encoding. Curr Biol 30:2574-2587.e6.

Pieribone VA, Nicholas AP, Dagerlind A, Hokfelt T (1994) Distribution of α1 adrenoceptors in rat brain revealed by in situ hybridization experiments utilizing subtype-specific probes. J Neurosci 14:4252–4268.

Pitler TA, Alger BE (1992) Cholinergic excitation of GABAergic interneurons in the rat hippocampal slice. J Physiol 450:127–142.

Poo C, Isaacson JS (2009) Odor Representations in Olfactory Cortex: "Sparse" Coding, Global Inhibition, and Oscillations. Neuron 62:850–861.

Pressler RT, Inoue T, Strowbridge BW (2007a) Muscarinic receptor activation modulates granule cell excitability and potentiates inhibition onto mitral cells in the rat olfactory bulb. J Neurosci 27:10969–10981.

Pressler RT, Inoue T, Strowbridge BW (2007b) Muscarinic Receptor Activation Modulates Granule Cell Excitability and Potentiates Inhibition onto Mitral Cells in the Rat Olfactory Bulb. J Neurosci 27:10969–10981.

Pressler RT, Strowbridge BW (2006) Blanes cells mediate persistent feedforward inhibition onto granule cells in the olfactory bulb. Neuron 49:889–904.

Price JL, Powell TPS (1970a) The synaptology of the granule cells of the olfactory bulb. J Cell Sci 7:91–123.

Price JL, Powell TPS (1970b) The Mitral and Short Axon Cells of the Olfactory Bulb. J Cell Sci 7:631–651.

Ragan T, Kadiri LR, Venkataraju KU, Bahlmann K, Sutin J, Taranda J, Arganda-Carreras I, Kim Y, Seung HS, Osten P (2012) Serial two-photon tomography for automated ex vivo mouse brain imaging. Nat Methods 9:255–258.

Rall W, Shepherd GMG (1968) Theoretical reconstruction of field potentials and dendrodendritic synaptic interactions in olfactory bulb. J Neurophysiol 31:884–915.

Ramirez-Gordillo D, Ma M, Restrepo D (2018) Precision of classification of odorant value by the power of olfactory bulb oscillations is altered by optogenetic silencing of local adrenergic innervation. Front Cell Neurosci 12.

Rodriguez-Molina VM, Aertsen A, Heck DH (2007) Spike timing and reliability in cortical pyramidal neurons: Effects of EPSC kinetics, input synchronization and background noise on spike timing. PLoS One 2.

Rodriguez I, Feinstein P, Mombaerts P (1999) Variable patterns of axonal projections of sensory neurons in the mouse vomeronasal system. Cell 97:199–208.

Rothermel M, Carey RM, Puche AC, Shipley MT, Wachowiak M (2014) Cholinergic inputs from Basal forebrain add an excitatory bias to odor coding in the olfactory bulb. J Neurosci 34:4654–4664.

Rothermel M, Wachowiak M (2014) Functional imaging of cortical feedback projections to the olfactory bulb. Front Neural Circuits 8:1–14.

Rubin BD, Katz LC (1999) Optical imaging of odorant representations in the mammalian olfactory bulb. Neuron 23:499–511.

Russo MJ, Franks KM, Oghaz R, Axel R, Siegelbaum SA (2020) Synaptic organization of

anterior olfactory nucleus inputs to piriform cortex. J Neurosci 40:9414–9425.

Sanz Diez A, Najac M, De Saint Jan D (2019) Basal forebrain GABAergic innervation of olfactory bulb periglomerular interneurons. J Physiol 597:2547–2563.

Sarter M, Bruno JP (2002) The neglected constituent of the basal forebrain corticopetal projection system: GABAergic projections. Eur J Neurosci 15:1867–1873.

Saunders A, Granger AJ, Sabatini BL (2015) Corelease of acetylcholine and GABA from cholinergic forebrain neurons. Elife 2015:1–13.

Schaefer AT, Margrie TW (2007) Spatiotemporal representations in the olfactory system. Trends Neurosci 30:92–100.

Schoppa NE (1998) Dendrodendritic inhibition in the olfactory bulb is driven by NMDA receptors. J Neurosci 18:6790–6802.

Schoppa NE (2006) Synchronization of olfactory bulb mitral cells by precisely timed inhibitory inputs. Neuron 49:271–283.

Schoppa NE, Urban NN (2003) Dendritic processing within olfactory bulb circuits. Trends Neurosci 26:501–506.

Shao Z, Puche AC, Liu S, Shipley MT (2012) Intraglomerular inhibition shapes the strength and temporal structure of glomerular output. J Neurophysiol 108:782–793.

Shepherd GMG (2004) The synaptic organization of the brain. Oxford univeristy press.

Shibuya T, Shibuya S (1963) Olfactory epithelium: unitary responses in the tortoise. Science 140:495–496.

Shin OH, Rhee JS, Tang J, Sugita S, Rosenmund C, Südhof TC (2003) Sr2+ binding to the Ca2+ binding site of the synaptotagmin 1 C2B domain triggers fast exocytosis without stimulating SNARE interactions. Neuron 37:99–108.

Shipley MT, Adamek GD (1984) The connections of the Mouse Olfactory Bulb: a Study Using Orthograde and Retrograde Transport of Wheat-Germ-Agglutinin Conjugated To Horseradish-Peroxidase. Brain Res Bull 12:669–688.

Shipley MT, Ennis M (1996) Functional organization of olfactory system. J Neurobiol 30:123–176.

Shipley MT, Halloran FJ, de la Torre J (1985) Surprisingly rich projection from locus coeruleus to the olfactory bulb in the rat. Brain Res 329:294–299.

Shusterman R, Smear MC, Koulakov AA, Rinberg D (2011) Precise olfactory responses tile the sniff cycle. Nat Neurosci 14:1039–1044.

Small KM, McGraw DW, Liggett SB (2003) Pharmacology and Physiology of Human Adrenergic Receptor Polymorphisms. Annu Rev Pharmacol Toxicol 43:381–411.

Smear M, Shusterman R, Connor RO, Bozza T, Rinberg D, O'Connor R, Bozza T, Rinberg D (2011) Perception of sniff phase in mouse olfaction. Nature 479:397–400.

Smith ML, Hale BD, Booze RM (1994) Calbindin-D28k Immunoreactivity within the Cholinergic and GABAergic Projection Neurons of the Basal Forebrain. Exp Neurol 130:230–236.

Smith R, Weitz CJ, Araneda RC (2009) Excitatory actions of noradrenaline and megabit topic glutamate receptor activations in granule cells of the accessory olfactory bulb. J Neurophysiol.

Smith RS, Hu R, DeSouza A, Eberly CL, Krahe K, Chan W, Araneda RC (2015) Differential Muscarinic Modulation in the Olfactory Bulb. J Neurosci 35:10773–10785.

Somogyi P, Katona L, Klausberger T, Lasztóczi B, Viney TJ (2014) Temporal

redistribution of inhibition over neuronal subcellular domains underlies state-dependent rhythmic change of excitability in the hippocampus. Philos Trans R Soc B Biol Sci 369.

Soucy ER, Albeanu DF, Fantana AL, Murthy VN, Meister M (2009) Precision and diversity in an odor map on the olfactory bulb. Nat Neurosci 12:210–220.

Stopfer M, Bhagavan S, Smith BH, Laurent G (1997) Impaired odor discrimination on desynchronization of odor–encoding neural assemblies. Nature 390:70–74.

Storace DA, Cohen LB (2017) Measuring the olfactory bulb input-output transformation reveals a contribution to the perception of odorant concentration invariance. Nat Commun 8:1–10.

Sturgill JF, Hegedus P, Li SJ, Chevy Q, Siebels A, Jing M, Li Y, Hangya B, Kepecs A (2020) Basal forebrain-derived acetylcholine encodes valence-free reinforcement prediction error. bioRxiv.

Südhof TC (2013) Neurotransmitter release: The last millisecond in the life of a synaptic vesicle. Neuron 80:675–690.

Sullivan RM, Wilson DA, Leon M (1989) Norepinephrine and learning-induced plasticity in infant rat olfactory system. J Neurosci 9:3998–4006.

Takács VT, Cserép C, Schlingloff D, Pósfai B, Szőnyi A, Sos KE, Környei Z, Dénes Á, Gulyás AI, Freund TF, Nyiri G (2018) Co-transmission of acetylcholine and GABA regulates hippocampal states. Nat Commun 9:9:2848.

Tamamaki N, Tomioka R (2010) Long-range GABAergic connections distributed throughout the neocortex and their possible function. Front Neurosci 4:1–8.

Tervo DGR, Hwang BY, Viswanathan S, Gaj T, Lavzin M, Ritola KD, Lindo S, Michael

S, Kuleshova E, Ojala D, Huang CC, Gerfen CR, Schiller J, Dudman JT, Hantman AW, Looger LL, Schaffer D V., Karpova AY (2016) A Designer AAV Variant Permits Efficient Retrograde Access to Projection Neurons. Neuron 92:372–382.

Thiele A (2013) Muscarinic signaling in the brain. Annu Rev Neurosci 36:271–294.

Trudeau LE, El Mestikawy S (2018) Glutamate cotransmission in cholinergic, GABAergic and monoamine systems: Contrasts and commonalities. Front Neural Circuits 12:113.

Uchida N, Takahashi YK, Tanifuji M, Mori K (2000) Odor maps in the mammalian olfactory bulb: domain organization and odorant structural features. Nat Neurosci 3:1035–1043.

Unal G, Joshi A, Viney TJ, Kis V, Somogyi P (2015) Synaptic targets of medial septal projections in the hippocampus and extrahippocampal cortices of the mouse. J Neurosci 35:15812–15826.

Urban NN, Sakmann B (2002) Reciprocal intraglomerular excitation and intra- and interglomerular lateral inhibition between mouse olfactory bulb mitral cells. J Physiol 542:355–367.

Villar PS, Hu R, Araneda RC (2021a) Long-Range GABAergic Inhibition Modulates Spatiotemporal Dynamics of the Output Neurons in the Olfactory Bulb. J Neurosci 41:3610–3621.

Villar PS, Hu R, Teitz B, Araneda RC (2021b) Cholinergic Modulation of Distinct Inhibitory Domains in Granule. bioRxiv 1322106.

Viney TJ, Salib M, Joshi A, Unal G, Berry N, Somogyi P (2018) Shared rhythmic subcortical GABAergic input to the entorhinal cortex and presubiculum. Elife 7:e34395.

Vinje WE, Gallant JL (2000) Sparse coding and decorrelation in primary visual cortex during natural vision. Science (80-) 287:1273–1276.

Voytko M Lou (1996) Cognitive functions of the basal forebrain cholinergic system in monkeys: Memory or attention? Behav Brain Res 75:13–25.

Voytko M Lou, Olton DS, Richardson RT, Gorman LK, Tobin JR, Price DL (1994) Basal forebrain lesions in monkeys disrupt attention but not learning and memory. J Neurosci 14:167–186.

Wachowiak M (2011) All in a Sniff: Olfaction as a Model for Active Sensing. Neuron 71:962–973.

Wachowiak M, Cohen LB (1999) Presynaptic inhibition of primary olfactory afferents mediated by different mechanisms in lobster and turtle. J Neurosci 19:8808–8817.

Wachowiak M, McGann JP, Heyward PM, Shao Z, Puche AC, Shipley MT (2005) Inhibition of olfactory receptor neuron input to olfactory bulb glomeruli mediated by suppression of presynaptic calcium influx. J Neurophysiol 94:2700–2712.

Wachowiak M, Shipley MT (2006) Coding and synaptic processing of sensory information in the glomerular layer of the olfactory bulb. Semin Cell Dev Biol 17:411–423.

Wagner S, Gresser AL, Torello AT, Dulac C (2006) A Multireceptor Genetic Approach Uncovers an Ordered Integration of VNO Sensory Inputs in the Accessory Olfactory Bulb. Neuron 50:697–709.

Wanaverbecq N, Semyanov A, Pavlov I, Walker MC, Kullmann DM (2007) Cholinergic axons modulate GABAergic signaling among hippocampal interneurons via postsynaptic alpha 7 nicotinic receptors. J Neurosci 27:5683–5693.

Wehr M, Zador AM (2003) Balanced inhibition underlies tuning and sharpens spike timing

in auditory cortex. Nature 426:442–446.

Wen H, Hubbard JM, Rakela B, Linhoff MW, Mandel G, Brehm P (2013) Synchronous and asynchronous modes of synaptic transmission utilize different calcium sources. Elife 2013:e01206.

Willmore BDB, Mazer JA, Gallant JL (2011) Sparse coding in striate and extrastriate visual cortex. J Neurophysiol 105:2907–2919.

Wilson CD, Serrano GO, Koulakov AA, Rinberg D (2017) A primacy code for odor identity. Nat Commun 8.

Wilson DA, Fletcher ML, Sullivan RM (2004) Acetylcholine and Olfactory Perceptual Learning. Learn Mem 11:28–34.

Wilson RI, Mainen ZF (2006) Early events in olfactory processing. Annu Rev Neurosci 29:163–201.

Winkowski DE, Bandyopadhyay S, Shamma SA, Kanold PO (2013) Frontal cortex activation causes rapid plasticity of auditory cortical processing. J Neurosci 33:18134–18148.

Woo CC, Leon M (1995) Distribution and development of β-adrenergic receptors in the rat olfactory bulb. J Comp Neurol 352:1–10.

Wood KC, Blackwell JM, Geffen MN (2017) Cortical inhibitory interneurons control sensory processing. Curr Opin Neurobiol 46:200–207.

Xu-Friedman M a, Regehr WG (2000) Probing fundamental aspects of synaptic transmission with strontium. J Neurosci 20:4414–4422.

Xu L, Li W, Voleti V, Zou DJ, Hillman EMC, Firestein S (2020) Widespread receptor-driven modulation in peripheral olfactory coding. Science (80-) 368.

Xu M, Chung S, Zhang S, Zhong P, Ma C, Chang W-C, Weissbourd BC, Sakai N, Luo L, Nishino S, Dan Y (2015) Basal forebrain circuit for sleep-wake control. Nat Neurosci 18:1641–1647.

Yang C, McKenna JT, Zant JC, Winston S, Basheer R, Brown RE (2014a) Cholinergic neurons excite cortically projecting basal forebrain GABAergic neurons. J Neurosci 34:2832–2844.

Yang C, McKenna JT, Zant JC, Winston S, Basheer R, Brown RE (2014b) Cholinergic neurons excite cortically projecting basal forebrain GABAergic neurons. J Neurosci 34:2832–2844.

Yang C, Thankachan S, McCarley RW, Brown RE (2017) The menagerie of the basal forebrain: how many (neural) species are there, what do they look like, how do they behave and who talks to whom?'. Curr Opin Neurobiol 45:221.

Ye M, Hayar A, Strotman B, Garcia-Rill E (2010) Cholinergic modulation of fast inhibitory and excitatory transmission to pedunculopontine thalamic projecting neurons. J Neurophysiol 103:2417–2432.

Yokoi M, Mori K, Nakanishi S (1995) Refinement of odor molecule tuning by dendrodendritic synaptic inhibition in the olfactory bulb. Proc Natl Acad Sci 92:3371–3375.

Zaborszky L, Buhl DL, Pobalashingham S, Bjaalie JG, Nadasdy Z (2005) Three-dimensional chemoarchitecture of the basal forebrain: Spatially specific association of cholinergic and calcium binding protein-containing neurons. Neuroscience 136:697–713.

Zaborszky L, Carlsen J, Brashear HR, Heimer L (1986) Cholinergic and GABAergic

afferents to the olfactory bulb in the rat with special emphasis on the projection neurons in the nucleus of the horizontal limb of the diagonal band. J Comp Neurol 243:488–509.

Záborszky L, Carlsen J, Brashear HR, Heimer L (1986) Cholinergic and GABAergic afferents to the olfactory bulb in the rat with special emphasis on the projection neurons in the nucleus of the horizontal limb of the diagonal band. J Comp Neurol 243:488–509.

Zaborszky L, Gaykema RP, Swanson DJ, Cullinan WE (1997) Cortical input to the basal forebrain. Neuroscience 79:1051–1078.

Zaborszky L, Pang K, Somogyi J, Nadasdy Z, Kallo I (1999) The basal forebrain corticopetal system revisited. Ann N Y Acad Sci 877:339–367.

Zaborszky L, van den Pol A, Gyengesi E (2012) The Basal Forebrain Cholinergic Projection System in Mice. In: The Mouse Nervous System, pp 684–718. Elsevier.

Zak JD, Reddy G, Vergassola M, Murthy VN (2020) Antagonistic odor interactions in olfactory sensory neurons are widespread in freely breathing mice. Nat Commun 11:1–12.

Zant JC, Kim T, Prokai L, Szarka S, McNally J, McKenna JT, Shukla C, Yang C, Kalinchuk A V., McCarley RW, Brown RE, Basheer R (2016) Cholinergic Neurons in the Basal Forebrain Promote Wakefulness by Actions on Neighboring Non-Cholinergic Neurons: An Opto-Dialysis Study. J Neurosci 36:2057–2067.

Zhu P, Frank T, Friedrich RW (2013a) Equalization of odor representations by a network of electrically coupled inhibitory interneurons. Nat Neurosci 16:1678–1686.

Zhu PX, Frank T, Friedrich RW (2013b) Equalization of odor representations by a network

of electrically coupled inhibitory interneurons. Nat Neurosci 16:1678–1686.

Zimnik NC, Treadway T, Smith RS, Araneda RC (2013) α 1A -Adrenergic regulation of inhibition in the olfactory bulb. J Physiol 5917:1631–1643.